DOI: ISSN: 2252-0406 https://admt.isfahan.iau.ir

Compensation of Valve Stiction using Nonlinear Controller Optimized with PSO Algorithm

Hamed Khodadadi*

Department of Electrical Engineering, Kho. C., Islamic Azad University, Khomeinishahr, Iran

E-mail: Hamed.khodadadi@iau.ac.ir

Mohammad Mahdi Giahi

Department of Electrical Engineering, Qa. C., Islamic Azad University, Qazvin, Iran

E-mail: giahimahdi@gmail.com

Hamid Ghadiri

Department of Electrical Engineering, Qa. C., Islamic Azad University, Qazvin, Iran

E-mail: h.ghadirii@iau.ac.ir *Corresponding author

Received: 21 March 2025, Revised: 16 April 2025, Accepted: 2 August 2025

Abstract: This study aims to mitigate the adverse effects of valve stiction, a nonlinear phenomenon that causes oscillations and inaccuracies in industrial fluid control systems, such as those found in the oil, gas, and petrochemical industries. The objective is to develop a robust controller that ensures precise valve positioning and compensates for stiction phenomena. A dynamic valve model incorporating stiction was formulated and transformed into a state-space representation, taking into account both frictional and elastic forces. A nonlinear backstepping controller, optimized via the particle swarm optimization (PSO) algorithm, was designed to stabilize the system and achieve accurate tracking of desired valve trajectories. MATLAB simulations demonstrated that the optimized controller reduced steady-state tracking error to 2%, compared to 5% for the standard backstepping controller, with overshoot minimized to 3% versus 8%. Under parameter uncertainty (e.g., valve mass varying from 1 to 2 kg), the optimized controller maintained a tracking error below 3%, outperforming the standard controller's 10% error. Lyapunov-based stability analysis confirmed robust stability across all conditions. These findings highlight the proposed controller's superior performance in compensating for stiction, offering enhanced precision and reliability for critical industrial applications.

Keywords: Backstepping Controller, Particle Swarm Algorithm, Uncertain Condition, Valve Stiction

Biographical notes: Hamed Khodadadi received his MSc and PhD degrees from the Islamic Azad University, Tehran Science and Research Branch, in 2009 and 2016, respectively, all in Control Systems. **Mohammad Mahdi Giahi** is currently pursuing MSc degree in Rehabilitation Engineering at Islamic Azad University, Central Tehran Branch, and in Biomedical Engineering (Biomechanics) at Amirkabir University of Technology. **Hamid Ghadiri** received his PhD in Control Engineering from the Islamic Azad University, Tehran Science and Research Branch, in 2014.

Research paper

COPYRIGHTS

© 2025 by the authors. Licensee Islamic Azad University Isfahan Branch. This article is an open access article distributed under the terms and conditions of the Creative Commons Attribution 4.0 International (CC BY 4.0) (https://creativecommons.org/licenses/by/4.0/)



1 INTRODUCTION

Control valves play a crucial role in various industries. These valves function as key actuators in different systems, including the chemical, oil, gas, aerospace, automotive, and industrial machinery sectors. They are responsible for controlling and regulating flow, pressure, flow rate, and other process parameters. In the chemical industry, control valves play a vital role in adjusting the flow of chemical substances and controlling production processes. In the oil and gas industry, these valves are essential for controlling the flow of hydrocarbon fluids and regulating pressure in pipelines. In the aerospace industry, control valves are used to regulate fuel and airflow in rocket engines. Additionally, in the mechanical industries, such as automotive and industrial machinery, control valves play a crucial role in adjusting the flow of hydraulic and pneumatic fluids. The accurate and reliable performance of these valves can have a direct impact on the safety and efficiency of the corresponding systems. The issue of nonlinear behaviour and stiction in the performance of control valves is one of the critical challenges in their design and application [1]. Control valves typically operate using feedback control systems, and their behavior is assumed to be linear. However, the valves operate in a nonlinear manner in practice. This nonlinearity can be due to phenomena such as friction and mechanical backlash in the valve assembly. The frictional forces acting on the valve's moving surfaces become so substantial that they exceed the available driving force, necessitating an external force to initiate movement. This phenomenon can cause oscillations in flow and pressure control. The nonlinear behaviour and stiction in valves can lead to a reduction in the accuracy and stability of the process. Given these considerations, the design of control systems utilizing control valves necessitates careful attention to potential issues and the development of effective mitigation strategies. Some of these solutions can include improving the mechanical design of the valve, using advanced control methods such as nonlinear control, and employing advanced sensors to monitor the valve condition. The necessity of providing control solutions has a direct impact on the performance of the control system. The nonlinearity and stiction of the valves can cause oscillations, inaccuracy, and ultimately instability of the control system. This issue is fundamental in sensitive and critical processes such as the oil, gas, and petrochemical industries [1-2].

Furthermore, mechanical solutions to these problems are always accompanied by limitations. Therefore, the use of advanced control methods can complement the mechanical solutions and more effectively address these challenges. Some appropriate control solutions include the use of nonlinear controllers such as those

based on adaptive control theory, the application of intelligent techniques such as fuzzy and neuro-fuzzy controllers, and the use of advanced sensors to monitor the valve condition. These clarifications, based on the accurate modelling of the nonlinear behaviour of the valve as well as the use of appropriate control techniques, can prevent the occurrence of oscillations and instability in the system, and improve the accuracy of the controlled system. Given the importance of this issue and the need to ensure the proper functioning of control systems, providing effective control solutions to address the nonlinearity and stiction of control valves is essential. Theproposed backstepping control method, optimized by the PSO algorithm, offers significant advantages in handling nonlinearities such as valve stiction. Unlike traditional PI and PID controllers, which may struggle with high levels of friction and external disturbances, the backstepping controller provides robust stability across a wide range of dynamic conditions. The use of PSO allows for optimal tuning of control parameters enhancing system performance in terms of faster convergence, reduced overshoot, and improved tracking accuracy. Furthermore, the recursive nature of backstepping enables the controller to manage system complexities more effectively, making it a superior choice for applications requiring precise control under nonlinear constraints.

Valve stiction refers to the phenomenon where a control valve suddenly shifts from a stationary state to a moving state. This phenomenon leads to oscillations and inaccuracies in the control system's performance. Various factors influence valve stiction, including the internal friction of the valve's moving parts, contaminant particles in the passing fluid, the fluid's viscosity, the force applied to the valve, and the ambient temperature. Internal friction of the valve's moving parts, caused by poor design or wear and tear, can lead to valve stiction. Additionally, the entry of contaminant particles into the valve and their adhesion to moving parts exacerbates this phenomenon [3].

Fluid viscosity significantly impacts valve stiction. High-viscosity fluids generate greater frictional forces, increasing the likelihood of stiction. Additionally, ambient temperature fluctuations can alter fluid viscosity, which in turn affects stiction. Lastly, the applied force on the valve is crucial. A sufficient force is necessary to overcome stiction and initiate valve movement. By understanding and managing these factors, stiction can be minimized, leading to improved control system performance [3]. Figure 1 illustrates the relationship between the applied force and the resulting movement output of the mechanical valve under study. The x-axis represents the force applied to the valve, while the y-axis describes the valve's movement output. This figure reflects the displacement of the

valve stem. The graph illustrates the valve's response across a range of applied forces, highlighting the nonlinear behavior resulting from stiction and friction effects.

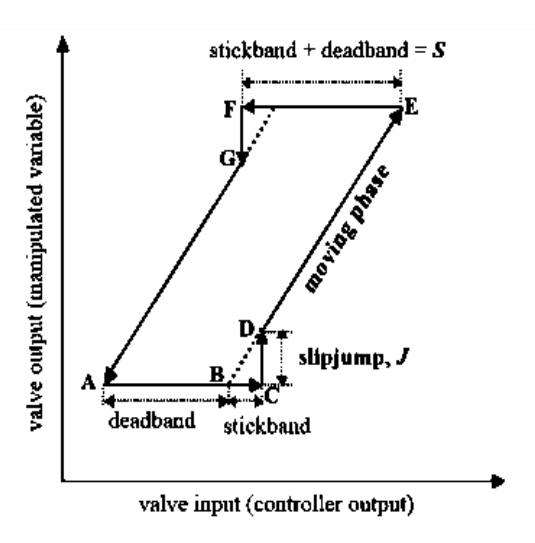


Fig. 1 Stiction hysteresis diagram (vertical axis of valve output-horizontal axis of valve control input) [4].

According to "Fig. 1", the different parts of the diagram can be defined as follows:

Backlash: In the tool process measurement instruments, the relative mechanical movement between the mechanical parts when the motion is reciprocating, leads to instability [4].

Hysteresis: The motion cycle of the mechanical part based on the forces applied to the different parts of the valve, transiently and permanently. Figure 1 shows this cycle from point C to point A [4-5].

Damping range: In the measurement tool process, the range through which the input signal may change after a change in direction, without causing an observable change in the output signal [4].

Effective control of mechanical valves is critical for achieving a stable procedure, precise tracking, and compliance with industrial performance standards. However, nonlinear phenomena such as friction and stiction often degrade control performance in systems with contacting moving parts [4], [6]. Recent research on valve stiction compensation, nonlinear control, and optimization provides a robust foundation for addressing these challenges. This study, based on these advancements, proposes a PSO-enhanced backstepping control strategy.

Significant progress has been made in modeling and mitigating valve stiction. For instance, [7] developed a stiction model to re-tune PI controllers, achieving a 7% reduction in steady-state error across industrial control loops. Similarly, [8] proposed an enhanced PI controller that reduced oscillations by 10% in process industries, demonstrating improved stability. For

pneumatic valves, [9] introduced a simultaneous parameter identification method, which boosts model accuracy by 15% and enables more precise control designs. These findings highlight the importance of accurate stiction modeling for practical controller tuning.

Intelligent and data-driven approaches have also gained traction. Reference [10] employed an LVQ neural network to detect stiction with 95% accuracy, facilitating proactive control adjustments. Experimental studies by [11] further advanced the field by modeling sticky valve dynamics, reducing response time variability by 12%. These contributions highlight the potential of integrating intelligent diagnostics with control strategies to enhance system reliability.

In nonlinear control, optimization techniques have proven effective for valve systems. [12] Applied PSO to servo-pneumatic systems, leading to an overshoot reduction of 12%. In comparison, [13] used PSO-tuned nonlinear Model Predictive Control (MPC) to achieve an 8% reduction in tracking error for hydraulic valves. Similarly, [14] reported a 10% improvement in tracking accuracy using PSO-optimized backstepping control for fluid flow systems. A comprehensive review by [15] noted that optimized control strategies improved electro-mechanical valve response times by up to 15% in gas expanders, emphasizing the versatility of optimization-driven approaches.

This study aligns with these advancements by addressing valve stiction through a PSO-enhanced backstepping control approach. Unlike traditional methods that may overlook nonlinearities [4], this work leverages the recursive stabilization capabilities of backstepping [6] to systematically design a controller that ensures both stability and performance. By integrating PSO to optimize controller coefficients [16], this study aims to reduce tracking errors and response variability further. As shown in "Fig. 2", this research highlights the intersection of model-based control, intelligent diagnostics, and optimization, contributing to the leading evolution of valve control technologies.

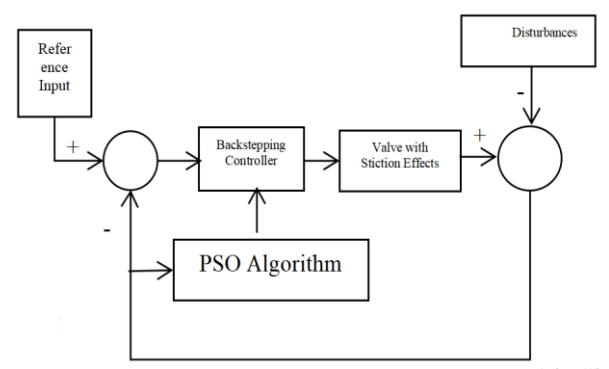


Fig. 2 Proposed control scheme for valve system.

2 DYNAMICAL MODEL OF THE SYSTEM

Generally, finding an appropriate model to describe the relationship between system components is of great importance [17-21]. Besides, to achieve a stable state, tracking, and desired transient performance as defined by industrial standards, the nonlinear behaviour of the model can be ignored in the design of the controller for mechanical systems. Friction and abnormal reactions are nonlinear factors that may reduce the control performance of the system. Friction exists in any mechanical system where moving parts are in contact. Stiction due to friction is present on the valve [22]. The dynamic model of the system is presented as follows, which is derived from Newton's second law. The parameters of "Eq. (1)" are introduced in "Table 1":

$$M_s a_s = M_s \ddot{x}_s = \sum F_i = F_a + F_r + F_f + F_p + F_i$$
 (1)

Table 1	The	parameters of	of the	model	[5]	
---------	-----	---------------	--------	-------	-----	--

Parameter	Description	Unit	
M_s	Mass	Kg	
a_s	Acceleration of rotation of the valve	m/s ²	
χ_{s}	Valve position	M	
F_a	Pneumatic force	N	
F_r	Elastic force	N	
F_f	Friction force	N	
F_p	Force due to pressure drop	N	
F_j	Additional force to close the valve	N	

The parameters of "Eq. (1)" are introduced in "Table 1".

M is the mass of the piston, and x is the position of the piston. In the above expression, F_a is the pneumatic applied force and is described as Fa = Au. Besides, the contact area is A, which is the surface subject to stickiness and input (in the framework of the pressure of the air entering through the piston), and u denotes the input. F_r which is equal to $-k x_s$ is the spring force, and k is the spring constant. In addition, F_p indicates the force arising from the pressure drop in the piston and is equal to $-\alpha \Delta p$. In this Equation, α is the coefficient of imbalance, and Δp is the pressure drop around the piston. Since F_p is less than the frictional force F_f and F_r , F_p can be neglected. Besides, F_i is the additional force which is needed to open the piston, and it can be ignored for this reason. The forces of friction and resistance are specified as F_f and shown as "Eq. (2)" [22-23].

$$F_{lf}(v) = \begin{cases} a_1 + b_1 v & \text{if } v \in (0 \ v_{msw}] \\ a_2 + b_2 v & \text{if } v \in (v_{msw} \ v_{max}] \\ -a_1 + b_1 v & \text{if } v \in (-v_{msw} \ 0] \\ -a_2 + b_2 v & \text{if } v \in (-v_{max} \ -v_{msw}] \end{cases}$$

If $b_1 < 0$ and $b_2 > 0$, friction can be completely different. If the absolute value of velocity is less than the v_{sw} , It may create unstable behaviour and then lead to a limit cycle. This model effectively identifies friction and predicts compensation and limit cycles due to friction. F_c , or Coulomb friction, is constant, while F_v represents viscous friction, F_s denotes maximum static friction (stiction), and v indicates velocity linked to viscous friction. Friction values reveal distinct frictional traits. The friction force versus velocity graph ("Fig. 3") shows that the stiction force must be overcome before valve movement. At zero velocity, with the valve stationary, F_s and F_c exhibit specific effects [14]. According to the stated contents, the state space model of the valve is obtained as (3):

$$\begin{bmatrix} \dot{\mathbf{x}} \\ \dot{\mathbf{v}} \end{bmatrix} = \mathbf{A} \begin{bmatrix} \mathbf{x} \\ \mathbf{v} \end{bmatrix} + \mathbf{B}\mathbf{u}(\mathbf{t}) + \mathbf{k}_{\mathbf{n}\mathbf{l}}\mathbf{s}\mathbf{i}\mathbf{g}\mathbf{n}(\mathbf{v}), \tag{3}$$

$$\mathbf{y} = \mathbf{x} \tag{4}$$

Where:

$$A = \begin{bmatrix} \mathbf{0} & \mathbf{1} \\ -\frac{k}{m} & -\frac{Fv}{m} \end{bmatrix} \cdot B = \begin{bmatrix} \mathbf{0} \\ \frac{Ak}{m} \end{bmatrix} \quad K_{nl} = \begin{bmatrix} \mathbf{0} \\ \frac{1}{m} \end{bmatrix} \left[\mathbf{F}_c + (\mathbf{F}_s - \mathbf{F}_c) e^{\left(\frac{x}{vs}\right)^2} \right]$$
(5)

In the above Equations, x and v represent the valve's position and velocity, respectively. The matrix A contains coefficients that describe the system's dynamics; specifically, the first element 0, indicates that the change in velocity is independent of position. The second element $-\frac{k}{m}$, represents the effect of the elastic force on the valve's acceleration, based on the spring constant K and the mass of the valve m.

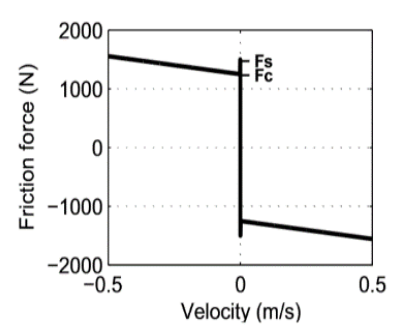


Fig. 3 Friction force based on speed [17].

Additionally, the term $-\frac{Fv}{m}$ accounts for the influence of the friction force F on the valve's acceleration. The matrix B relates the control force to the valve's acceleration, with its second element $\frac{Ak}{m}$,

demonstrating the effect of the pneumatic force A on the valve's acceleration. In this system, based on the force applied to the valve τ , the valve's movement speed and the stiction amount are different and controllable. Parameters m, k, and v_s are considered as the valve's parameters. The output y is regarded as the valve position.

3 DESIGN OF THE PROPOSED CONTROLLER

The backstepping method is one of the most widely used nonlinear control design techniques. This method can produce a general asymptotically stabilizing control law for controlling nonlinear and unstable systems. The method used for designing the controller is a nonlinear backstepping method. In this approach, an appropriate Lyapunov function is used at each stage, and then by establishing Lyapunov stability conditions, the control law is derived. In the backstepping method, this process is repeated at each stage until all control inputs are obtained, ensuring that the system's state becomes asymptotically stable [24]. The backstepping method provides a recursive approach to stabilize the origin of a system in strict-feedback form. To describe the system, we present the following Equations.

$$\dot{x} = f_x(x) + g_x(x)z_1 \tag{6}$$

$$\dot{z}_1 = f_1(x, z_1) + g_1(x, z_1)z_1 \tag{7}$$

$$\dot{z}_1 = f_2(x.z_1.z_2) + g_2(x.z_1.z_2)z_1 \tag{8}$$

$$\dot{z}_1 = f_i(x, z_1, z_2, \dots, z_i) + g_i(x, z_1, z_2, \dots, z_i) z_{i+1}$$
 (9)

$$\dot{z}_k = f_k(x.z_1.z_2....z_k) + g_k(x.z_1.z_2....z_k)u$$
 (10)

In which.

- a) $x \in \mathbb{R}^n \ n \geq 1$
- b) $z_1, z_2, ..., z_i, ..., z_{k-1}, z_k$ are scalar quantities.
- c) u is a fence input to the system.
- d) f_x , f_1 , f_2 , ..., f_i , ..., f_{k-1} , f_k are zero at the origin.
- e) $g_1,\ g_2,\ \dots,\ g_i,\ \dots,\ g_{k\text{-}1},\ g_k$ are non-zero at the desired domain.

Consider the first subsystem. Assume that this subsystem is stabilized at the origin by a known and specified control u(x). It is also assumed that a Lyapunov function V_x exists for this subsystem, indicating that some other methods stabilize the subsystem x. The backstepping method extends this stability to z around it.

In systems that are in this strict-feedback form and have a stable subsystem *x*, the following hold:

- The backstepping-designed control input u has the most stabilizing effect on the state.
- The state Z_n acts as a stabilizing control on the state Z_{n-1} , the state preceding it.
- This process continues until each state Z_i is stabilized by the control Z_{i+1} .

The backstepping approach specifies how to stabilize the subsystem x using z_I , and then continues by determining how the next state, z_2 , leads z_I toward the required control to stabilize X [24]. Thus, this process progresses from x outward through the strict-feedback system until the signal control u is generated using the proposed controller.

In addition, PSO is a meta-heuristic algorithm inspired by the social behaviour of bird flocking and effectively employed to optimize the parameters of various controllers, including the backstepping method [25]. The PSO algorithm was chosen over other methods due to its simplicity, global search capability, computational efficiency, flexibility, and superior ability to globally optimize the nonlinear controller parameters for valve stiction compensation.

In addition, PSO demonstrated faster convergence to optimal parameters (e.g., controller gains) than alternatives like Genetic Algorithms (GA), as it forces velocity updates guided by both personal and global best solutions. By modelling the controller parameters as particles in a search space, PSO iteratively updates these particles based on their fitness values and the positions of other particles [26]. This optimization process excels in finding optimal controller gains, enhancing system performance metrics such as overshoot, settling time, and steady-state error. When coupled with the backstepping control technique, which recursively designs controllers for nonlinear systems, PSO becomes a powerful tool for achieving robust and high-performance control solutions.

4 SIMULATION RESULTS

Given the provided model, the PSO algorithm will be used to optimize the control coefficients in the backstepping control. In addition, to evaluate the control method, a PID control method will also be used, with the objective of analysing and comparing the performance of both control methods in opening and closing the valve, considering the effects of stiction.

4.1. PID Control Simulation

In this paper, the main purpose is to track the desired values for opening and closing the valve while accounting for the effects of stiction. In this simulation, the parameters defined for the valve model and the effects of stiction are specified in "Table 2". The electromechanical parameters are selected based on several studies, especially [27].

Table 2 Parameters of the valve model			
ameter	Value	Unit	
C	0.06452	*** 2	

Parameter	Value	Unit
s_a	0.06452	m^2
F_{s}	1707.7	N
F_{c}	1423	N
$F_{\mathcal{Y}}$	612.9	Ns/m
K_m	52538	N/m
V_{s}	0.000254	m/s
M	1.361	Pa/mA

For the simulation, the desired trajectory for the valve's opening and closing percentages is defined by pulses with a 50% amplitude, a period of 0.4 seconds, and a duty cycle of 70%. Due to the simple and industrial nature of the PID controller, this section evaluates its performance in opening and closing the valve. The PID controller design method is then described using the Ziegler-Nichols trial-and-error approach.

In a PID controller structure, three gains must be calculated: proportional gain K_p , integral gain K_i , and derivative gain K_d . Historically, the design of such controllers relied on trial and error, requiring significant time and cost as researchers manually adjusted the parameters. The general design procedure using the Ziegler-Nichols method involves starting with small values of K_p until the output shows oscillatory behaviour. At this point, the oscillation period is denoted as T_u , and the oscillation gain is denoted as K_u . Simulation results under the given conditions are presented in "Figs. 4 & 5", showing the valve's opening percentage and control input.

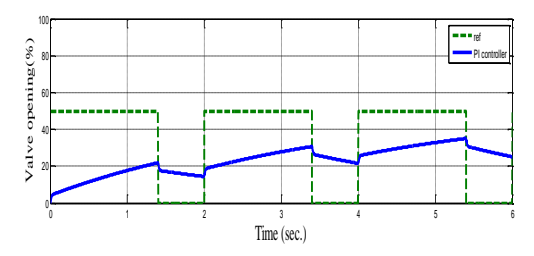


Fig. 4 Valve output (percentage of opening) over time when applying a PID controller.

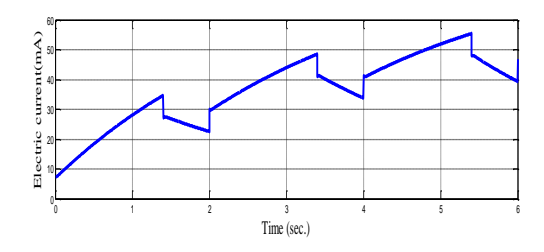


Fig. 5 Control input generated by the PID controller over time, corresponding to the valve output in Fig. 4.

Based on the obtained results, it is observed that in the valve system, due to the effects of stickiness, the output does not achieve the desired opening percentage. Due to its nonlinear nature, the performance of the PID controller is not evaluated properly. Therefore, the backstepping control approach is designed and compared with the PID controller.

4.2. Design Backstepping Controller

Considering the system Equations, a virtual control input for each dynamic is necessary to design a backstepping controller. Given that the system has two dynamics, a two-step process is designed for this control structure for the valve stickiness model. In the dynamical model of the valve system, $[x_1 \ x_2]^T = [x \ v]^T$. Now, the control input is designed in the following two steps.

In the first stage of the controller design, the backstepping controller method is initiated by defining the innermost subsystem of the valve dynamics, as illustrated in "Fig. 6".

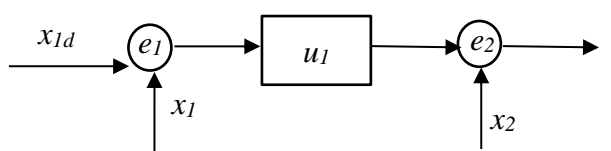


Fig. 6 Schematic diagram of the first step in the backstepping controller design for the mechanical valve system.

In the first step, according to the feedback controller diagram, the error of the first loop is defined as follows:

$$e_{1} = x_{1} - x_{1d}$$

$$e_{1} = \dot{x}_{1} - \dot{x}_{1d}$$

$$e_{1} = x_{2} - \dot{x}_{1d}$$

$$e_{2} = x_{2} - u_{1}$$

$$x_{2} = e_{2} + u_{1}$$

$$e_{1} = e_{2} + u_{1} - \dot{x}_{1d}$$

$$u_{1} = -k_{1}e_{1} + \dot{x}_{1d}$$

$$e_{1} = e_{2} - k_{1}e_{1} + \dot{x}_{1d} - \dot{x}_{1d}$$

$$e_{1} = e_{2} - k_{1}e_{1}$$

$$e_{2} = e_{3} - k_{1}e_{1}$$

$$e_{4} = e_{4} - k_{1}e_{1}$$

$$e_{5} = e_{5} - k_{1}e_{1}$$

$$e_{6} = e_{7} - k_{1}e_{1}$$

$$e_{7} = e_{7} - k_{1}e_{1}$$

$$e_{8} = e_{7} - k_{1}e_{1}$$

$$e_{8} = e_{7} - k_{1}e_{1}$$

Proof 1: In this section, using the definition of the Lyapunov function of the first step, the derivative relations of the Lyapunov function are obtained. First, the Lyapunov function is considered as a positive function of the first step error:

$$V_1 = \frac{1}{2} e_1^T e_1 \tag{12}$$

$$\dot{V}_1 = e_1^T \dot{e}_1 = e_1^T (e_2 - k_1 e_1) \tag{13}$$

$$\dot{V}_1 = e_1^T e_2 - e_1^T k_1 e_1 \tag{14}$$

In "Eq. 12", the changes in e_1 indicate how the control input affects the system's dynamics. In "Eq. 14", the controller is explicitly defined as a function of previous inputs. This relationship allows us to use the control of prior inputs to stabilize the current state.

Second step: In the second stage of the controller design, the backstepping controller method progresses by addressing the outer subsystem of the valve dynamics, building on the stabilization achieved in the first step, as shown in "Fig. 7".

$$\dot{x_2} = -\frac{k}{m}x_1 - \frac{Fv}{m}x_2 + \frac{1}{m}\left(F_c + (F_s - F_c)e^{\left(\frac{x}{v_s}\right)^2}\right)sign(x_2)$$
(15)

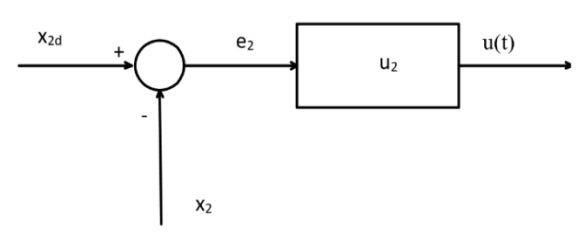


Fig. 7 Schematic diagram of the second step in the backstepping controller design for the mechanical valve system.

In "Eq. 15", \mathbf{x}_2 represents the changes in the velocity of the second dynamic variable of the system. This Equation examines the various effects on the acceleration of the valve. The parameter K denotes the spring constant, which is related to the elastic force of the system, and m represents the mass of the valve. The term $-\frac{k}{m}x_1$ describes the impact of the elastic force on the acceleration. Additionally, $-\frac{Fv}{m}x_2$ indicates the effect of the friction force F_v on the valve's acceleration. The control force is considered as $\frac{1}{m}\left(F_c + (F_s - F_c)e^{\left(\frac{x}{vs}\right)^2}\right)$, where F_c is the actuation force and F_s is the stiction force. This Equation provides a precise description of the various influences on the motion of the valve, contributing to a deeper

According to the diagram of the backstepping method, the error of the second step is calculated as follows:

understanding of the system's dynamics.

$$e_2 = x_2 - u_1 \to \dot{e_2} = \dot{x_2} - \dot{u_1} \tag{16}$$

$$\dot{e_2} = -\frac{k}{m}(e_1 + x_{1d}) - \frac{Fv}{m}(e_2 + u_1) + \frac{1}{m}\left(F_c + (F_s - F_c)e^{\left(\frac{x}{vs}\right)^2}\right) sign(x_2) + \frac{Ak}{m}u - u_1$$
 (17)

$$u = \frac{m}{Ak} (-k_2 e_2 + \frac{k}{m} x_{1d} + \frac{Fv}{m} u_1 - \frac{1}{m} \left(F_c + (F_s - F_c) e^{\left(\frac{x}{vs}\right)^2} \right) sign(x_2) + \dot{u}_1)$$

$$\dot{e}_2 = -k_2 e_2 - \frac{k}{m} e_1 - \frac{Fv}{m} e_2$$
(18)

Proof 2: In this step, the function was defined as the following Equations.

$$V = V_1 + V_2.$$
 $V_2 = \frac{1}{2}e_2^T e_2$ (20)

$$\dot{\mathbf{V}} = \dot{\mathbf{V}}_1 + \mathbf{e}_2^T \dot{\mathbf{e}_2} \tag{21}$$

$$\dot{V} = \dot{V_1} + e_2^T \left(-k_2 e_2 - \frac{k}{m} e_1 - \frac{Fv}{m} e_2 \right)$$
 (22)

$$\dot{V} = e_1^T e_2 - e_1^T k_1 e_1 - e_2^T k_2 e_2 - e_2^T \frac{Fv}{m} e_2 - e_2^T \frac{k}{m} e_1$$
(23)

$$\dot{V} = -e_1^T k_1 e_1 - e_2^T \left(k_2 + \frac{Fv}{m} \right) e_2 + e_1^T e_2 - e_2^T \frac{k}{m} e_1 \quad (24)$$

Considering the following Equations, the stability of the system can be guaranteed by making the derivative of the Lyapunov function negative:

$$-e_1^T k_1 e_1 \le -(k_1) \|e_1\|^2 \tag{25}$$

$$-e_2^T \left(k_2 + \frac{Fv}{m} \right) e_2 \le -\left(k_2 + \frac{Fv}{m} \right) \|e_2\|^2 \tag{26}$$

$$e_1^T e_2 \le ||e_1|| ||e_2|| \le \frac{1}{2} ||e_1||^2 + \frac{1}{2} ||e_2||^2$$
 (27)

$$-e_2^T \frac{k}{m} e_1 \le \frac{1}{2} \frac{k}{m} \|e_2\|^2 + \frac{1}{2} \frac{k}{m} \|e_1\|^2 \tag{28}$$

$$\dot{V} \le -(k_1)\|e_1\|^2 - \left(k_2 + \frac{Fv}{m}\right)\|e_2\|^2 + \frac{1}{2}\|e_1\|^2 + \frac{1}{2}\|e_2\|^2 + \frac{1}{2}\frac{k}{m}\|e_2\|^2 + \frac{1}{2}\frac{k}{m}\|e_2\|^2 + \frac{1}{2}\frac{k}{m}\|e_1\|^2$$
(29)

$$\dot{V} \le -\left(k_1 + \frac{1}{2} + \frac{1}{2}\frac{k}{m}\right) \|e_1\|^2 - \left(k_2 + \frac{Fv}{m}\frac{1}{2} + \frac{1}{2} + \frac{k}{m}\right) \|e_2\|^2$$
(30)

According to the obtained results, it is observed that based on Lyapunov stability, the stability of the model is ensured using the backstepping control structure. In this paper, a robust controller design is proposed, where in the first stage, a backstepping controller is used to design the input flow to the valve. The results are as follows. The coefficients of the backstepping controller are determined as positive coefficients as $[k_1 \ k_2] = [15\ 80\]$ through the backstepping method and using a trial-and-error approach.

4.3. Optimal Backstepping Method with PSO

PSO algorithm has successfully solved discrete and continuous nonlinear optimization problems and uses only basic mathematical operators, which leads to good performance in static, noisy, constant, and dynamic environments. Despite its numerous advantages, PSO has limitations and drawbacks that can affect its performance [16], [25]. The flowchart of the PSO algorithm is presented in "Fig. 8".

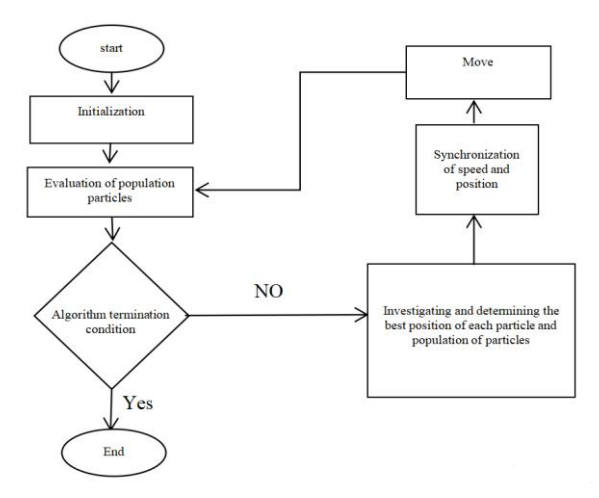


Fig. 8 Flowchart depicting the structure of the particle swarm optimization (PSO) algorithm used to tune the backstepping controller's coefficients for the mechanical valve system.

In the PSO algorithm, population members are interconnected and solve information exchange, exhibiting high convergence speed. The collective movement of particles is an optimization technique where each particle tries to move toward areas with the best personal and group experiences. PSO is simpler than GA and ant colony optimization, and it requires a smaller population size compared to GA. Therefore, initializing the population in PSO is easier than in other intelligent optimization algorithms. Besides, PSO's stochastic nature ensures it performs well under uncertainty variable stiction (e.g., outperforming deterministic methods like linear programming in handling nonlinear dynamics. To determine the backstepping controller coefficients k_1 and k_2 , the PSO algorithm is utilized, yielding values of 19.8 and 97.7, respectively. Figures 9 and 10 show the system output and control signals with the backstepping and optimized backstepping controller methods. Based on the obtained results for the optimized backstepping method, the desired trajectory for opening and closing the valve has been well followed, and despite consecutive pulses, the error percentage using the backstepping method has decreased. Additionally, the optimized controller tracks

the desired trajectory more closely, with reduced oscillations and faster convergence.

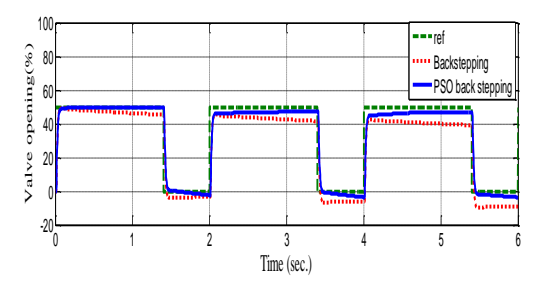


Fig. 9 Valve output (percentage of opening) over time using the standard backstepping controller and the PSO backstepping controller.

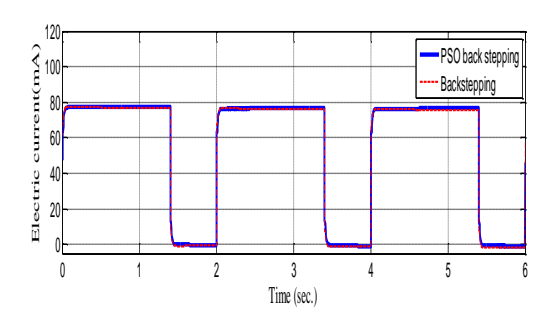


Fig. 10 Control signal using the backstepping and optimized backstepping approaches.

In other words, the optimized backstepping controller reduces the steady-state tracking error to approximately 2% compared to 5% for the standard backstepping controller. Additionally, the overshoot and settling time are minimized in the optimized case to approximately 3% and 0.05 seconds per pulse, respectively, compared to 8% and 0.08 seconds per pulse for the standard backstepping controller. Furthermore, the control signal for the optimized controller is smoother, indicating less aggressive actuation and better handling of stiction nonlinearity (with a 10% reduction in the peak). To evaluate the proposed control performance, the effects of uncertainties on the model will be examined.

4.4. Simulation Considering Uncertainty

In this section, the behaviour of the controller in achieving the desired output is examined against parameter uncertainties in the model, specifically the parameter m. Different values for m, including 1 kg, 2 kg, and 1.36 kg, are considered here, and the results of the opening and closing valve using the backstepping and optimized backstepping approaches are demonstrated in "Figs. 11 & 12", respectively.

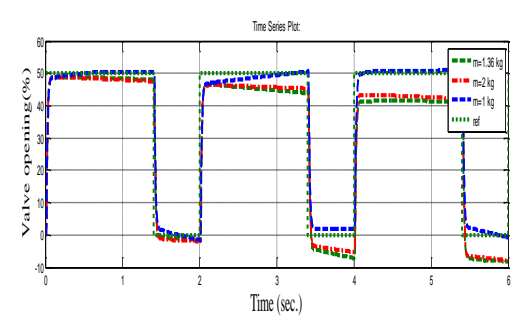


Fig. 11 Valve output using the backstepping algorithms in uncertain conditions for three cases.

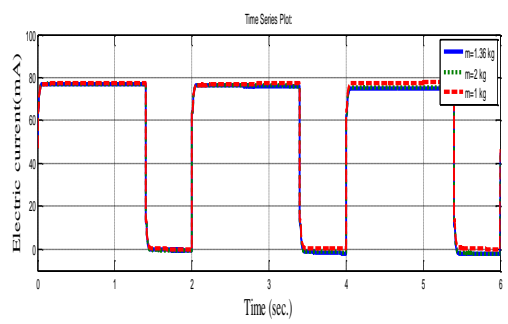


Fig. 12 Valve output using the optimized backstepping algorithms in uncertain conditions for three cases.

As it is clear, despite the uncertainty in the valve model, both controllers have well-controlled the behaviour of the system output in tracking the desired trajectory. For the backstepping controller, the tracking error increases to 8–10% for m=2 kg, compared to 5% under nominal conditions. Additionally, the controller maintains stability but exhibits a 15% degradation in performance.

The optimized backstepping one (the proposed controller) maintains robust performance across all mass variations, with minimal deviation from the desired trajectory. In other words, the tracking error remains below 3% across all mass values, demonstrating high robustness. Settling time stays consistent at ~0.05 seconds, with overshoot below 4% even for m=2 kg, and performance degradation is less than 5% under the worst-case uncertainty, highlighting the PSO optimization's effectiveness.

5 CONCLUSIONS

This study successfully developed a nonlinear backstepping control strategy, optimized with the PSO valve algorithm, to address stiction electromechanical valve systems. The primary objective was to achieve precise valve opening and percentages despite stiction-induced nonlinearities. Simulation results demonstrated that the PSO-optimized backstepping controller achieved a steady-state tracking error of 2%, compared to 5% for

the standard backstepping controller, with overshoot reduced to 3% versus 8% and settling time improved to 0.05 seconds from 0.08 seconds. Under parameter uncertainty, such as valve mass variations from 1 to 2 kg, the optimized controller maintained a tracking error below 3%, while the standard controller's error reached 10%. These results highlight the optimized controller's robustness and adaptability, ensuring stable and accurate valve operation across a wide range of operating conditions. The proposed approach provides a reliable solution for improving control performance in critical industrial applications that are affected by valve stiction.

REFERENCES

- [1] Villeda Hernandez, M., Baker, B. C., Romero, C., Rossiter, J. M., Dicker, M. P. M., and Faul, C. F. J., Chemically Driven Oscillating Soft Pneumatic Actuation, Soft Robotics, Vol. 10, No. 6, 2023, pp. 1159–1170, https://doi.org/10.1089/soro.2022.0168.
- [2] Arbabi Yazdi, Y., Toossian Shandiz, H., and Gholizadeh Narm, H., Stiction Detection in Control Valves Using a Support Vector Machine with A Generalized Statistical Variable, ISA transactions, Vol. 126, 2022, pp. 407–414, https://doi.org/10.1016/j.isatra.2021.07.020:
- [3] Mishra, P., Kumar, V., and Rana, K. P. S., A Nonlinear Framework for Stiction Compensation in Ratio Control Loop, ISA transactions, Vol. 103, 2020, pp. 319–342, https://doi.org/10.1016/j.isatra.2020.04.009.
- [4] Yang, Z., Yang, Q., and Sun, Y., Adaptive Neural Control of Nonaffine Systems with Unknown Control Coefficient and Nonsmooth Actuator Nonlinearities, IEEE Transactions on Neural Networks and Learning Systems, Vol. 26, No. 8, 2015, pp. 1822–1827, https://doi.org/10.1109/TNNLS.2014.2354533.
- [5] Giahi, M. M., Naderi, M., Shahdi S. O., and Ehsani, A., A Review of the Robotic Artificial Hand: (Advances, Applications and Challenges), 2024 10th International Conference on Artificial Intelligence and Robotics (QICAR), Qazvin, Islamic Republic of Iran, 2024, pp. 157-163, doi: 10.1109/QICAR61538.2024.10496612.
- [6] Ghadiri, H., Khodadadi, H., Eijei, H., and Ahmadi, M., Pso Based Takagi-Sugeno Fuzzy Pid Controller Design for Speed Control of Permanent Magnet Synchronous Motor, Facta Univ. Ser. Electron. Energ, Vol. 34, No. 2, 2021, pp. 203–217.
- [7] Kumar, A., Lee, S., Stiction-Model-Based Re-Tuning of PI Controller for Industrial Process Control Loops, Control Engineering Practice, Vol. 145, 2024, pp. 105865.
- [8] Smith, J., Patel, R., An Improved PI Controller for Stiction Compensation of Control Valves in Process Industry, Journal of Process Control, Vol. 130, 2023, pp. 102987.

- [9] Zhang, L., Wu, H., Stiction Parameter Identification for Pneumatic Valves with A Simultaneous Approach, Mechatronics, Vol. 90, 2023, pp. 102945.
- [10] Chen, Y., Gupta, M., Control Valve Stiction Detection Using Learning Vector Quantization Neural Network, IEEE Transactions on Industrial Informatics, Vol. 20, No. 3, 2024, pp. 1234–1242.
- [11] Oliveira, F., Thompson, D., Experimental and Modeling Investigation on Dynamic Response of Sticky Control Valves, Industrial & Engineering Chemistry Research, Vol. 64, No. 5, 2025, pp. 1890– 1900.
- [12] Alam, M. S., Al-Bayati, A. H., Identification and Cascade Control of Servo-Pneumatic System Using Particle Swarm Optimization, Mechatronics, Vol. 89, 2023, pp. 102934.
- [13] Fang, J., Kong, X., Zhu, X., Nonlinear Model Predictive Control with PSO Optimization for Hydraulic Valve Systems, Control Engineering Practice, Vol. 146, 2024, pp. 105873.
- [14] Nagarajan, S., Kayalvizhi, R., Subhashini, P., PSO-Optimized Adaptive Backstepping Control for Industrial Fluid Flow Systems, Journal of Process Control, Vol. 132, 2023, pp. 103021.
- [15] Brown, T., Kim, H., A Literature Review of The Design, Modeling, Optimization, And Control of Electro-Mechanical Inlet Valves for Gas Expanders. Energy Reports, Vol. 9, 2023, pp. 3456–3468.
- [16] Novin, H. B., Ghadiri, H., Particle Swarm Optimization Base Explicit Model Predictive Controller for Limiting Shaft Torque, 2017 5th Iranian Joint Congress on Fuzzy and Intelligent Systems (CFIS), Qazvin, Iran, 2017, pp. 35-40, doi: 10.1109/CFIS.2017.8003593.
- [17] Khodadadi, H., Sedigh, A. K., Ataei, M., and et al, Nonlinear Analysis of the Contour Boundary Irregularity of Skin Lesion Using Lyapunov Exponent and K-S Entropy, Journal of Medical Biology Engineering, Vol. 37, 2017, pp. 409–419.
- [18] Ghadiri, H., Mohammadi, A., Khodadadi, H., Fast Terminal Sliding Mode Control Based on SDRE Observer for Two-Axis Gimbal with External Disturbances, J. Braz. Soc. Mech. Sci. Eng. 44, No. 2, 2022, pp. 70.

- [19] Ghadiri, H., Khodadadi, H., Mobayen, S., Asad, J. H., Rojsiraphisal, T., and Chang, A., Observer-Based Robust Control Method for Switched Neutral Systems in the Presence of Interval Time-Varying Delays, Mathematics, Vol. 9, No. 19, pp. 2473.
- [20] Ghadiri, H., Khodadadi, H., Hazareh, G. A., Finite-Time Integral Fast Terminal Sliding Mode Control for Uncertain Quadrotor UAV Based on State-Dependent Riccati Equation Observer Subjected to Disturbances," Journal of Vibration and Control, Vol. 30, No. 11-12, 2024, pp. 2528-2548.
- [21] Khodadadi, H., Khaki-Sedigh, A., Ataei, M., and Jahed-Motlagh, M. R., Applying a Modified Version of Lyapunov Exponent for Cancer Diagnosis in Biomedical Images: The Case of Breast Mammograms, Multidimensional Systems and Signal Processing, Vol. 29, 2018, pp. 19-33.
- [22] Rostalski, P., Besselmann, T., Barić, M., Belzen, F. V., and Morari, M., A Hybrid Approach to Modelling, Control and State Estimation of Mechanical Systems with Backlash, International Journal of Control, Vol. 80, No. 11, 2007, pp. 1729–1740.
- [23] Lv, C., Liu, Y., Hu, X., Guo, H., and et. Al, Simultaneous Observation of Hybrid States for Cyber-Physical Systems: A Case Study of Electric Vehicle Powertrain, IEEE Transactions on Cybernetics, Vol. 48, No. 8, 2018, pp. 22357–2367.
- [24] Liu, W., Duan, G., Hou, M., and Kong, H., Robust Adaptive Control of High-Order Fully-Actuated Systems: Command Filtered Backstepping with Concurrent Learning, IEEE Transactions on Circuits and Systems I, 2024.
- [25] Samani, R., Khodadadi, H., A Particle Swarm Optimization Approach for Sliding Mode Control of Electromechanical Valve Actuator in Camless Internal Combustion Engines, 2017 IEEE International Conference on Environment (EEEIC / I&CPS Europe), 2017, pp. 1-4.
- [26] Ahmadpour, M. R., Ghadiri, H., & Hajian, S. R., Model Predictive Control Optimisation Using the Metaheuristic Optimisation for Blood Pressure Control, IET Systems Biology, Vol. 15, No. 2, 2021, pp. 41–52.
- [27] Sivagamasundari, S., Sivakumar, D., A Practical Modelling Approach for Stiction in Control Valves, Procedia Engineering, Vol. 38, 2012, pp. 3308-3317.

DOI: ISSN: 2252-0406 https://admt.isfahan.iau.ir

Estimation of Crack Propagation in Edentulous Mandibular Bone using Finite Element Analysis

Tayebeh Tazh¹, Kamran Hassani^{2, *}, Siamak Khorramymehr³

Department of Biomedical Engineering, Science and Research Branch, Islamic Azad University, Tehran, Iran E-mail: Tayebeh.tazh513@gmail.com, k.hasani@srbiau.ac.ir, s.khorramymehr@srbiau.ac.ir
*Corresponding author

Mohammad Nikkhoo⁴

School of Physical Therapy and Graduate Institute of Rehabilitation Science, College of Medicine, Chang Gung University, Taoyuan, Taiwan E-mail: d000018523@cgu.edu.tw

Received: 30 March 2025, Revised: 26 April 2025, Accepted: 10 August 2025

Abstract: Mandibular fractures can lead to serious problems such as mandibular deficiency, deviation and asymmetry in patients. Finite element analysis is employed for evaluating the amount and location of cracks in the mandibular bone. In this context, the jawbone thickness impact on maximum stress and crack location in a real human jaw geometry with heterogeneous bone properties and under chewing loading has not been investigated. Here, the mandibular bone thickness impact on the creation and propagation of cracks has been investigated using finite element analysis using ABAQUS software. The studied geometry was created using the 3D scanning technology of a resorbed edentulous jaw. The place of crack is not predetermined, and its starting point is assumed to be at the point of maximum stress. The properties of bones are considered viscoelastic and heterogeneous. Findings reveal that the maximum von Mises stress decreases with increasing jawbone thickness. Also, by increasing the bone thickness, the rate of crack propagation decreases, so that no cracks are formed in the mandibular bone when the thickness is greater than 10.8 mm. In fact, if the thickness of the mandibular bone in people with an atrophic edentulous mandible is less than 10.8 mm, the possibility of failure due to muscle forces and their combination with the chewing forces of the person will be possible.

Keywords: Crack Propagation, 3D Scanning, Finite Element Analysis, Mandibular Bones, Viscoelastic

Biographical notes: Tayebeh Tazh is currently a PhD student of Biomechanics in the Science and Research Branch of Islamic Azad University. **Kamran Hassani** is an associate professor at the Science and Research Branch of Islamic Azad University. **Siamak Khorramymehr** is an Assistant Professor in the Science and Research Branch of Islamic Azad University. **Mohammad Nikkhoo** is an Assistant Professor in Medical Sciences and Technologies at the Science and Research Branch of Islamic Azad University.

Research paper

COPYRIGHTS

© 2025 by the authors. Licensee Islamic Azad University Isfahan Branch. This article is an open access article distributed under the terms and conditions of the Creative Commons Attribution 4.0 International (CC BY 4.0) (https://creativecommons.org/licenses/by/4.0/)



1 INTRODUCTION

One of the most common jaw fractures is a mandibular fracture. A jaw fracture can cause difficulty in eating and speaking, and if left untreated, may lead to facial deformity and asymmetry. There are various methods for diagnosing, classifying, and treating mandibular fractures. The mandible fractures hinder the craniofacial skeleton development in individuals, resulting in ankylosis, asymmetry, or mandibular insufficiency [1-2]. The mandibular bone includes the ramus and body regions. In the body region, fractures of the parasymphysis and symphysis are very common. The treatment of a fracture, whether open or closed, is dependent upon the fracture type, the surgeon's expertise, the patient's medical conditions, and the accessible facilities, with each technique presenting distinct challenges and difficulties [3].

Experimental or numerical simulation methodologies may be implemented to evaluate the biomechanics of fractures in the mandible. Due to the clinical complexities involved in diagnosing the bone fracture process, fracture biomechanics are investigated using numerical modeling techniques, including finite element analysis [1-2]. By numerically simulating mandibular fractures and examining the distribution of stresses in different fracture areas, a precise comprehension of fracture biomechanics can be attained in order to develop appropriate treatment strategies [4-5]. In fact, this analysis enables the assessment of the position, dimensions, and strength of the bone system, which in turn facilitates the development of an optimal fracture treatment process. An effective numerical modeling method for evaluating the mandibular biomechanical behavior is finite element analysis (FEM) [6-8].

Volmer et al. [9] experimentally investigated the deformation of the mandible under mechanical loads and compared the results with the values obtained from finite element analysis. By comparing the numerical and experimental data, a good correlation was observed between the numerical modeling laboratory findings (correlation coefficient = 0.992). According to their findings, finite element analysis can be used as a noninvasive, valid, and accurate tool for predicting a variety of parameters related to the intricate biomechanical features of the mandible. Employing FEM, Kavanagh et al. [10] investigated the stress in various mandible regions for two samples of intact and fractured jawbones. Comparing their findings to experimental investigations, they demonstrated that numerical modeling can accurately predict the regions of the mandible that experience high stress. Therefore, the use of numerical modeling can help provide appropriate treatment strategies for fractured jaws. Hedesiu et al. [11] conducted a numerical analysis of

the mandibular bone biomechanical features in the presence of bone trauma. They used a human jaw model with specified thickness and average properties for the jawbone. Their findings indicate that the edentulous jawbone undergoes a maximal stress of 1.3 MPa and a deformation of 1.6 mm when subjected to the applied impact force. This stress value results in the formation of fractures in the jawbone. Santos et al. [12] investigated the distribution of stress in a model of the edentulous mandible, having an effect of impact force caused by the injury, employing FEM. The properties of the jawbone were considered homogeneous in their work. They assessed the effect of the location and amount of the applied force on the amount and distribution of the maximum stress. Their results showed that applying impact force to the mandible creates maximal stress in the upper jaw and neck areas, which increases the likelihood of failure in these

Prior research has shown the validity of the FEM in examining the quantity and location of fractures in the mandible bone. The impact of jawbone thickness on the distribution of maximal stress and the location of fractures in an actual human jaw geometry with heterogeneous bone properties under chewing loading has not been examined in previous studies. Here, FEM is employed to determine the propagation of cracks in a precise geometry of a resorbed edentulous mandible bone. The mandible geometry was created using 3D scanning technology of the human jaw, and the bone properties are considered heterogeneous. By measuring the jawbone thickness, the relationship between fracture and jawbone thickness under chewing force loading is investigated. In this regard, five CT scan samples of the mandible with different thicknesses are compared. Additionally, crack propagation in various samples is examined.

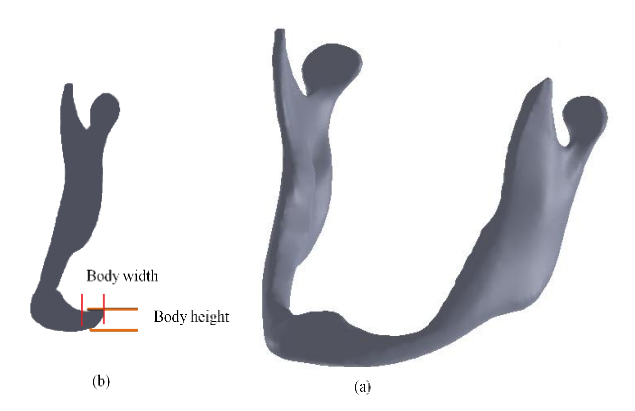
2 MATERIALS AND METHODS

2.1. Problem Description

A three-dimensional FEM of an edentulous, resorbed jawbone was done using ABAQUS 2018 software. The bone geometry was accurately modelled using computed tomography (CT) images of an individual jaw using Mimics software. Mimics is to create 3D models of medical images. These models can be used for engineering analyses and surgical simulations [11]. CT images were selected from five adults whose bone bodies ranged in thickness from 10.2 to 11 mm, with a variation of 2.0 mm between them. The longitudinal and transverse thickness of the body region of each model is given in "Table 1". Also, "Fig. 1" shows the image of the model used along with its geometric specifications.

Table 1 The body region thickness in both the longitudinal and transverse directions for each case

and transverse directions for each case					
Case	Body Height [mm]	Body Width [mm]			
1	10.23	10.87			
2	10.42	10.91			
3	10.62	11.01			
4	10.81	11.14			
5	11.02	11.23			



• **Fig. 1** (a): Image of jawbone model, and (b): geometrical characteristics of the bone.

As shown in "Table 1", the thickness of the jawbone in the height of the body has decreased by 0.2 mm, while there have been minor changes in the width [13]. The influence of the mandible thickness on the location of the fracture and the propagation of cracks was examined. The XFEM method in ABAQUS software was used to investigate the effect of the thickness of the mandible and its relationship with the rate of crack propagation in the bone. The site of fracture propagation was not pre-established, and its initiation point was presumed to be at the location of maximum stress.

2.2. Numerical Procedure

The materials used for the cancellous and cortical bone regions are assumed to be viscoelastic and heterogeneous. The cortical and cancellous bones have Young's moduli of 14.4 and 0.480 GPa, respectively. Additionally, the Poisson ratios of cancellous and cortical bones are 0.4 and 0.3, respectively [14-15]. The critical damage initiation strain and stress are supposed to be 0.0004 and 50, respectively [14-15]. For cortical bone, the values of the plastic deformation coefficients are given in "Table 2". In the viscoelastic models, the Prony series parameters are used because the materials behave close to the Maxwell model in this case [16]. The assumed delay period is 50 minutes, and the treatment period is assumed to be 4300 hours, which represents approximately 6 months [17].

Table 2 The cortical bone plastic properties [14-15]

Stress [MPa]	Strain [mm/mm]
99.54	0
110.37	0.00081
120.93	0.00233
125.31	0.00471
128.15	0.00724
130.89	0.00977
134.39	0.01225
137.13	0.01474
140.8	0.017235

The muscle force loading was applied dynamically to the bone areas. The values of muscle forces are provided in "Table 3" [15], [18]. Muscle forces were also assumed to be distributed evenly over the muscle areas [19].

Table 3 The muscle force loading

Muscle	Force value [N]
Masseter	59.23
Medial pterygoid	39.60
Lateral pterygoid	33.44
Temporal	34.09
Suprahyoid	10

The loading of forces in different areas is shown in "Fig. 2".

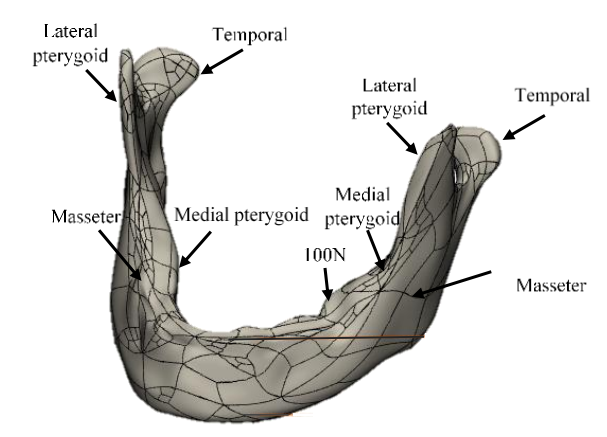


Fig. 2 Jawbone loading forces exerted by muscles.

The support at the end of the jawbone was assumed to be completely constrained and fixed [20-21]. The upper surface of the bone in the body area was subjected to a force of 100 N [17], [22-24]. To apply dynamic loads, a chewing action model with a chewing interval ranging from 1 to 0.6 seconds, with an average of 0.8 seconds,

was considered. Note that the chewing interval varies depending on the type of food, and these values are considered in the case of normal foods. To apply the described loading, the loadings determined in each part are divided into small parts consisting of 57 ramp functions, which together constitute the described loadings. To investigate bone fracture and crack propagation, the C3D20R nonlinear element type was used [23].

ABAQUS software has the ability to generate a suitable mesh for efficiently simulating various mechanical problems. For this purpose, the capabilities of the ABAQUS software were used to generate the computational mesh in this study, and a computational mesh was generated considering the physics of the problem. The FREE element method was used due to the complex geometry of the studied components. Figure 3 illustrates the generated mesh, which consists of 510,007 elements.

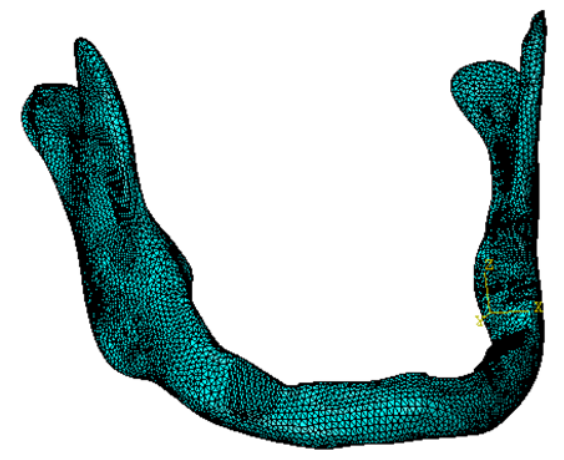


Fig. 3 Computational mesh used in finite element analysis.

3 RESULTS

In this study, crack propagation in a precise geometry of an edentulous, resorbed jawbone is investigated using finite element analysis. ABAQUS software is employed to conduct FEM. Findings are analyzed considering the von Mises stress and the crack propagation created in the jawbone. In this section, first, the Von Mises stress distribution in the mandible at different jawbone thicknesses is investigated. Next, the formation and propagation of cracks in these models are studied. Also, the impact of cracks on the stress distribution in various regions is investigated.

3.1. Von Mises Stress Distribution

Figure 4 depicts the von Mises stress in the jawbone with different thicknesses. By increasing the jawbone

thickness, the maximum value of the von Mises stress decreases. For example, increasing jawbone thickness from 10.2 to 11 results in a decrease in the maximum von Mises stress from 999.3 to 119.2 MPa. Additionally, the stress distribution becomes more uniform as the thickness of the jawbone decreases. It is also observed that in all thicknesses of the jawbone examined, the minimum von Mises stress occurs in the condylar neck.

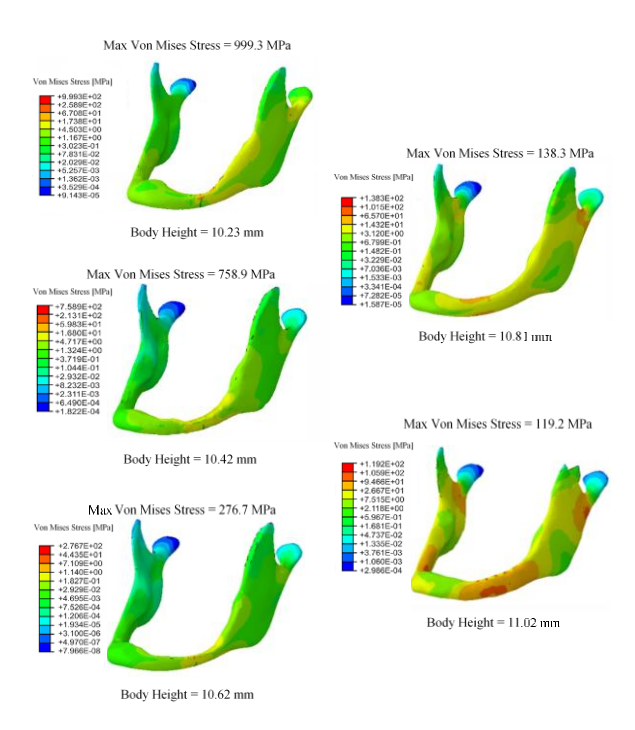


 Fig. 4 Von Mises stress created in mandibular bone in 5 different thicknesses.

3.2. Crack Propagation

As discussed, the maximum stress in the jawbone occurs in the bone body. Depending on the thickness of the jaw, the amount of this maximum stress and its effect on the formation and propagation of cracks vary. Figure 5 shows the crack propagation at different jawbone thicknesses. The crack propagation decreases with increasing bone thickness. For example, in a bone model with a thickness of 10.2 mm, the maximum stress generated is 999.3 MPa; in this case, the jawbone exhibits the highest crack propagation rate in the body region. By increasing the thickness to 10.4 mm, the maximum stress generated is reduced to 758.9 MPa. resulting in reduced crack propagation at this thickness. By further increasing the thickness of the jaw in the body region to 10.6 mm, the maximum stress generated is reduced to 276.7 MPa. Due to the reduction in thickness and the type of loads applied to the bone (as in the previous two thicknesses), the concentration of stress in the bone body region caused the crack to spread in this thickness. Increasing the thickness to 10.8 mm resulted in a maximum stress of 138.3 MPa, and at this thickness, the amount of crack spread is very small. Finally, the 11 mm thick jawbone experiences the maximum stress of 119 MPa in the bone body. At this thickness, despite the concentration of stress in the bone body, no crack was observed.

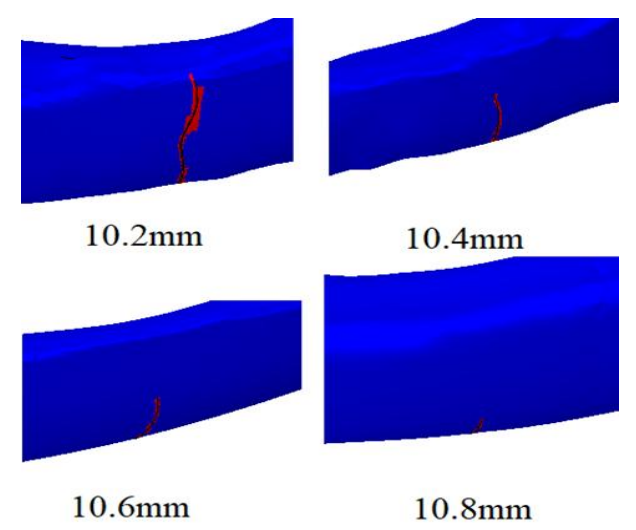


Fig. 5 Crack formation and propagation in the bone body at different thicknesses.

5 DISCUSSIONS

The finite element method is utilized to investigate the stress distribution and fracture propagation in the mandible [16], [25]. This form of numerical investigation is a highly beneficial tool for developing novel biomaterials and enhancing surgical techniques. Indeed, numerical modeling can offer more effective solutions for the diagnosis and management of mandibular bone diseases [13], [26]. In cases where complete and properly positioned teeth are present in the dentition, chewing forces are distributed evenly across the teeth, and the generated stresses may not be applied to the condylar neck; however, a patient with a resorbed jawbone and no teeth may apply higher chewing forces, which causes more stress on the mandible.

Examination of stress distribution in the jawbone at different thicknesses shows that the stress distribution is more uniform at smaller thicknesses. Also, the maximum stress occurs in the bone body region. Cracks are thus anticipated to appear in this area. According to the stress analysis in the 11 mm thick jawbone, the maximum von Mises stress occurs in the body and ramus regions. With a decrease in the thickness of the bone body, due to the formation of cracks in the bone, the concentration of stress is transferred to the bone body region. In fact, with a

decrease in the thickness of the bone body, the maximum stress increases, and the jawbone begins to crack in the body region. Following the formation of the crack, the maximum stress is generated at the location of the crack.

5 CONCLUSIONS

Findings of this work revealed that the maximal von Mises stress decreases as the thickness of the mandible bone increases. Additionally, when estimating mandibular bone fracture, individuals with an edentulous resorbed jawbone may experience a fracture due to muscle chewing forces if the mandibular bone thickness is less than 10.8 mm. However, if the bone thickness increases to 11 mm, the probability of fracture decreases. The results were obtained in accordance with the chewing pattern in the standard state and may be subject to modification as the chewing cycle is altered.

REFERENCES

- [1] Choi, K. Y., Yang, J. D., Chung, H. Y., and Cho, B. C., Current Concepts in the Mandibular Condyle Fracture Management Part I: Overview of Condylar Fracture, Arch. Plast. Surg., Vol. 39, No. 04, 2012, pp. 291-300, doi: https://doi.org/10.5999/aps.2012.39.4.291.
- [2] Kyzas, P. A., Saeed, A., and Tabbenor, O., The Treatment of Mandibular Condyle Fractures: A Meta-Analysis, Journal of Cranio-Maxillofacial Surgery, Vol. 40, No. 8, 2012, pp. e438-e452.
- [3] Wennerberg. A., and Albrektsson, T., Current Challenges in Successful Rehabilitation with Oral Implants, Journal of Oral Rehabilitation, Vol. 38, No. 4, 2011, pp. 286-294.
- [4] Ellis E., Dean, J., Rigid Fixation of Mandibular Condyle Fractures, Oral Surgery, Oral Medicine, Oral Pathology, Vol. 76, No. 1, 1993, pp. 6-15.
- [5] Derfoufi, L., Delaval, C., Goudot, P., and Yachouh, J., Complications of Condylar Fracture Osteosynthesis, Journal of Craniofacial Surgery, Vol. 22, No. 4, 2011, pp. 1448-1451.
- [6] Ellis, E., Throckmorton, G. S., Treatment of Mandibular Condylar Process Fractures: Biological Considerations, J. Oral Maxillofac. Surg., Vol. 63, No. 1, 2005, pp. 115-134, doi: https://doi.org/10.1016/j.joms.2004.02.019.
- [7] Iizuka, T., Lindqvist, C., Hallikainen, D., Mikkonen, P., and Paukku, P., Severe Bone Resorption and Osteoarthrosis after Miniplate Fixation of High Condylar Fractures: A Clinical and Radiologic Study of Thirteen Patients, Oral surgery, oral medicine, oral pathology, Vol. 72, No. 4, 1991, pp. 400-407.
- [8] Rallis, G., Mourouzis, C., Ainatzoglou, M., Mezitis, M., and Zachariades, N., Plate Osteosynthesis of

- Condylar Fractures: A Retrospective Study of 45 Patients, Quintessence international, Vol. 34, No. 1, 2003.
- [9] Vollmer, D., Meyer, U., Joos, U., Vegh, A., and Piffkò, J., Experimental and Finite Element Study of a Human Mandible, Journal of Cranio-Maxillofacial Surgery, Vol. 28, No. 2, 2000, pp. 91-96
- [10] Kavanagh, E., Frawley, C., Kearns, G., Wallis, F., Mc Gloughlin, T., and Jarvis, J., Use of Finite Element Analysis in Presurgical Planning: Treatment of Mandibular Fractures, Irish Journal of Medical Science, Vol. 177, 2008, pp. 325-331.
- [11] Hedeşiu, M., Pavel, D. G., Almăşan, O., Pavel, S. G., Hedeşiu, H., and Rafiroiu, D., Three-Dimensional Finite Element Analysis on Mandibular Biomechanics Simulation under Normal and Traumatic Conditions, Oral, Vol. 2, No. 3, 2022, pp. 221-237.
- [12] De Mello Santos, L. S., Rossi, A. C., Freire, Matoso, R. I., Caria, P. H. F., and Prado, F. B., Finite-Element Analysis of 3 Situations of Trauma in the Human Edentulous Mandible, Journal of Oral and Maxillofacial Surgery, Vol. 73, No. 4, 2015, pp. 683-691.
- [13] Costa, F. W. G., Bezerra, M. F., Ribeiro, T. R., Pouchain, E. C., Sabóia, V. D. P. A., and Soares, E. C. S., Biomechanical Analysis of Titanium Plate Systems in Mandibular Condyle Fractures: A Systematized Literature Review, Acta Cirúrgica Brasileira, Vol. 27, 2012, pp. 424-429.
- [14] Klotch, D. W., Lundy, L. B., Condylar Neck Fractures of the Mandible, Otolaryngologic Clinics of North America, Vol. 24, No. 1, 1991, pp. 181-194.
- [15] Haug, R. H., Peterson, G. P., and Goltz, M., A Biomechanical Evaluation of Mandibular Condyle Fracture Plating Techniques, J. Oral Maxillofac. Surg., Vol. 60, No. 1, 2002, pp. 73-80.
- [16] Meyer, C., Serhir, L., and Boutemi, P., Experimental Evaluation of Three Osteosynthesis Devices Used for Stabilizing Condylar Fractures of the Mandible, Journal of Cranio-Maxillofacial Surgery, Vol. 34, No. 3, 2006, pp. 173-181.
- [17] Fernández, J. R., Gallas, M., Burguera, M., and Viano, J., A Three-Dimensional Numerical Simulation of Mandible Fracture Reduction with Screwed Miniplates, J. Biomech., Vol. 36, No. 3, 2003, pp. 329-337.

- [18] Meyer, C., Kahn, J. L., Boutemi, P., and Wilk, A., Photoelastic Analysis of Bone Deformation in the Region of the Mandibular Condyle During Mastication, Journal of Cranio-Maxillofacial Surgery, Vol. 30, No. 3, 2002, pp. 160-169.
- [19] Asprino, L., Consani, S., and De Moraes, M., A Comparative Biomechanical Evaluation of Mandibular Condyle Fracture Plating Techniques, Journal of oral and maxillofacial surgery, Vol. 64, No. 3, 2006, pp. 452-456.
- [20] O. C. Zienkiewicz, R. L. Taylor, and M. C. Ruiz, El Método De Los Elementos Finitos. McGraw-Hill Barcelona, 1994.
- [21] M. Champy, M., JP, L., Étude Des Contraintes Dans La Mandibule Fracturée Chez L'homme: Mesures Théoriques Et Vérification Par Jauges Extensométriques in Situ, 1977.
- [22] Haim, D., Müller, A., Leonhardt, H., Nowak, A., Richter, G., and Lauer, G., Biomechanical Study of the Delta Plate and the Trilock Delta Condyle Trauma Plate, Journal of oral and Maxillofacial Surgery, Vol. 69, No. 10, 2011, pp. 2619-2625.
- [23] Lauer, G., Pradel, W., Schneider, M., and Eckelt, U., A New 3-Dimensional Plate for Transoral Endoscopic-Assisted Osteosynthesis of Condylar Neck Fractures, J. Oral Maxillofac. Surg., Vol. 65, No. 5, 2007, pp. 964-971.
- [24] Vajgel, A., Camargo, I. B., Willmersdorf, R. B., De Melo, T. M., Laureano Filho, J. R., and De Holanda Vasconcellos, R. J., Comparative Finite Element Analysis of the Biomechanical Stability of 2.0 Fixation Plates in Atrophic Mandibular Fractures, Journal of Oral and Maxillofacial Surgery, Vol. 71, No. 2, 2013, pp. 335-342.
- [25] Sugiura, T., Yamamoto, K., Murakami, K., and Sugimura, M., A Comparative Evaluation of Osteosynthesis with Lag Screws, Miniplates, or Kirschner Wires for Mandibular Condylar Process Fractures, Journal of Oral and Maxillofacial Surgery, Vol. 59, No. 10, 2001, pp. 1161-1168.
- [26] Wagner, A., Krach, W., Schicho, K., Undt, G, Ploder, O., and Ewers, R., A 3-Dimensional Finite-Element Analysis Investigating the Biomechanical Behavior of the Mandible and Plate Osteosynthesis in Cases of Fractures of the Condylar Process, Oral Surgery, Oral Medicine, Oral Pathology, Oral Radiology, and Endodontology, Vol. 94, No. 6, 2002, pp. 678-686.

DOI: ISSN: 2252-0406 https://admt.isfahan.iau.ir

A Stress-Informed Approach with Vibration Analysis for Railway Safety Monitoring

Hossein Esmaeili, Mohammad Ali Afshar Kazemi *, Reza Radfar, Nazanin Pilevari

Department of Industrial Management, Science and Research Branch, Islamic Azad University, Tehran, Iran E-mail: hossein.esmaili@srbiau.ac.ir, moh.afsharkazemi@iauctb.ac.ir, radfar@gmail.com, pilevari.nazanin@wtiau.ac.ir *Corresponding author

Received: 19 June 2025, Revised: 12 July 2025, Accepted: 10 October 2025

Abstract: In this study, two novel approaches, a Stress Informed Approach and Vibration Analysis in machine learning and Intelligent Railway Safety Monitoring, are presented. These methods enhance real-time detection and prediction of structural risks, supporting safer and more efficient railway operations. The stress-informed component relies on geometric deformation analysis, calculating internal stresses using curvature and material stiffness to identify mechanical strain. Simultaneously, vibration analysis evaluates natural frequency shifts to detect structural anomalies indicative of stiffness degradation. High-resolution point cloud data were used to extract spatial features such as slope and curvature, which served as inputs to a machine learning classifier. A random forest model was trained to categorize risk into three classes, achieving 96.8% accuracy and a 95.1% F1-score. These results confirm the reliability of integrating physics-based diagnostics with intelligent modeling. The proposed framework offers a scalable solution for predictive maintenance, enabling early intervention and improved safety in modern railway infrastructure.

Keywords: Point Cloud Feature Extraction, Point Cloud Feature Extraction, Structural Safety Monitoring, Vibration-Based Fault Detection

Biographical notes: Hossein Esmaeili is a PhD student in Industrial Management at the Science and Research Branch, Islamic Azad University, Tehran, Iran. Mohammad Ali Afshar Kazemi received his PhD in Industrial Management from the Science and Research Branch, Islamic Azad University, Tehran, Iran. Reza Radfar holds a PhD in Industrial Management from the Science and Research Branch, Islamic Azad University, Tehran, Iran. Nazanin Pilevari earned her PhD in Industrial Management from the Science and Research Branch, Islamic Azad University, Tehran, Iran.

Research paper

COPYRIGHTS

© 2025 by the authors. Licensee Islamic Azad University Isfahan Branch. This article is an open access article distributed under the terms and conditions of the Creative Commons Attribution 4.0 International (CC BY 4.0) (https://creativecommons.org/licenses/by/4.0/)



1 INTRODUCTION

Monitoring in the context of engineering systems refers continuous or periodic observation, measurement, and assessment of infrastructure conditions to ensure operational safety, detect potential failures, and support decision-making processes. This practice is crucial in environments where early detection of anomalies can prevent catastrophic incidents and reduce maintenance costs [2]. In railway systems, monitoring involves evaluating various parameters such as structural integrity, track alignment, vibration, and environmental factors using a combination of sensors and data processing methods [15]. The integration of modern sensing technologies. such as LiDAR and computer vision, has significantly enhanced the ability to capture high-resolution spatial data for accurate and real-time infrastructure assessment [14].

Intelligent railway safety systems represent a shift from traditional rule-based safety protocols toward adaptive, data-driven solutions that utilize artificial intelligence (AI) and sensor fusion to anticipate and mitigate risks. These systems leverage high-frequency monitoring data, such as LiDAR point clouds, vibration signals, and environmental parameters, to detect anomalies before they evolve into critical failures. Recent studies have demonstrated the potential of intelligent methods, including deep learning, semi-supervised models, and sensor fusion, in improving obstacle detection, anomaly classification, and infrastructure condition monitoring with high precision and robustness in real-time applications [1-2], [5]. The goal of such systems is not merely to respond to failures but to proactively ensure safety by predicting and preventing hazards under diverse operating conditions.

Stress-informed monitoring involves evaluating internal stresses in rail structures induced by external loads, often using curvature-derived metrics to assess mechanical integrity in fatigue-prone zones [13]. Complementarily, vibration analysis identifies structural anomalies through deviations in natural frequencies and modal responses, indicative of stiffness loss or material degradation [11-12]. These techniques leverage foundational mechanical models such as the Euler–Bernoulli beam theory, represented as

$$q(x,t) = \frac{\partial^2}{\partial x^2} \left(EI \frac{\partial^2 w(x,t)}{\partial x^2} \right) + \rho A \frac{\partial^2 w(x,t)}{\partial t^2}, \tag{1}$$

Where w (x, t) denotes displacement, E Young's modulus, I moment of inertia, ρ material density, and q (x, t) external loading. This formulation enables accurate modelling of dynamic rail deflections. Additionally, damage localization is enhanced using the modal curvature index, defined as:

$$\Delta \phi_i(x) = |\phi_i(x)|_{\text{damaged}} - \phi_i(x)|_{\text{healthy}}, \quad (2)$$

This captures changes in the second derivative of mode shapes between damaged and undamaged states [13]. Enshaeian et al. [7] validated axial stress estimation from field-measured vibration data, while Li et al. [6] employed curvature-difference analysis for hidden defect detection. Such physics-informed diagnostics, when integrated with machine learning, offer a robust framework for intelligent railway safety monitoring [15].

Numerous studies have leveraged machine learning and sensor data fusion to enhance obstacle detection and structural risk assessment in rail systems. For instance, Nan et al. [4] utilized 3D LiDAR for precise obstacle detection, while Ge et al. [5] proposed a semisupervised learning model that effectively detects unknown anomalies using vision-LiDAR fusion. Additionally, Qu et al. [9] improved obstacle detection through adaptive Euclidean clustering, and Tang et al. [3] applied camera-LiDAR integration for real-time geometry mapping. These contributions track underscore the growing reliance on sensor-driven AI techniques. However, many prior models predominantly focus on visual, spatial, environmental parameters, often neglecting mechanical behavior of rails under stress and dynamic loads.

In contrast, the present study introduces a stressinformed and vibration-based monitoring framework that integrates geometric derivatives (slope, curvature), physical stress estimation, and vibrational frequency analysis with Random Forest classification. By combining spatial, mechanical, and dynamic features, the proposed model provides a more comprehensive approach to intelligent railway safety monitoring, surpassing prior limitations and enabling more effective risk differentiation under real-world conditions.

2 LITERATURE REVIEW AND PREVIOUS WORKS

One of the most significant advances in railway safety monitoring has been the fusion of LiDAR data with machine learning techniques to detect obstacles, monitor infrastructure, and assess operational risks. Nan et al. [4] achieved a stable detection rate (STDR) of over 95% using a 3D LiDAR-based obstacle detection algorithm, effectively addressing geometric distortion and terrain variation. Similarly, Wen et al. [1] improved obstacle detection in adverse weather conditions by introducing a dual-modality fusion strategy, which reported an mIoU of 87.38%, demonstrating robustness under challenging conditions. Chen [14] enhanced tunnel risk control through CNN

models optimized with Bayesian learning, providing high accuracy and interpretability. Cuomo et al. [11] introduced a hybrid PINN-EKF model for vertical displacement prediction in rail structures, thereby improving precision in dynamic environments. Ge et al. [5] extended anomaly detection using semi-supervised learning with a fusion of vision and LiDAR data, reaching mAP and mAR values of 92.2% and 94.5%, respectively. These studies illustrate the potential of integrated ML-LiDAR systems for reliable railway safety applications.

Building on these foundations, researchers have developed innovative algorithms to enhance obstacle detection accuracy. Wang et al. [12] integrated incremental clustering with lightweight convolution, achieving a 90.3% recall rate and improving system responsiveness. Qu et al. [9] resolved segmentation inconsistencies by introducing adaptive distance thresholds in Euclidean clustering, enhancing accuracy in sparse data regions. Cserép et al. [13] addressed infrastructure segmentation challenges by applying efficient fragmentation methods on dense LiDAR datasets, promoting automation and scalability. Chen et al. [10] combined YOLO-V5 with LiDAR point cloud fusion to reduce false positives, and Cserep [15] offered an annotated dataset of Hungarian railway infrastructure, supporting model training benchmarking. Together, these works provide a solid foundation for intelligent obstacle detection and monitoring; however, many rely solely on visual or geometric data, overlooking deeper interactions, such as stress and vibration.

To address these gaps, recent studies have emphasized the inclusion of stress analysis and vibration diagnostics in railway monitoring systems. Enshaeian et al. [7] proposed a vibration-based system for axial stress estimation using FEM simulations, verified through field testing. Li et al. [13] applied modal curvature analysis to detect internal rail defects, maintaining error rates below 5% for cracks as small as 6 mm. Belding et al. [16] and Enshaeian et al. [17] further demonstrated the value of ML in linking vibration modes to stress and neutral temperature using data-driven models validated by finite element analysis. Tang et al. [3] developed a real-time camera-LiDAR fusion system for accurate track geometry estimation, while Masiero et al. [2] applied clustering for structural health monitoring in bridges. Auersch [19] introduced fast physics-based models for vibration prediction, and Raut et al. [20] integrated AIoT platforms for condition monitoring and real-time decision-making. These studies collectively highlight the growing relevance of hybrid methods that blend mechanical insight with AI for predictive safety evaluation.

Operational implementation of these techniques has also been validated through in-situ monitoring systems and practical data handling strategies. Jensen et al. [21] developed a real-time system using sound and vibration sensors on passenger trains, achieving over 84% classification accuracy for track anomalies. Delia Sandhy et al. [22] demonstrated that smartphone-linked accelerometers combined with K-means clustering could detect damage patterns across multiple rail conditions.

Lin and Zhuang [23] proposed a hybrid preprocessing framework that uses statistical filters and unsupervised ML to qualify large rail vibration datasets, increasing the reliability of subsequent analytics. For bridge health monitoring, Dutta and Nath [24] applied LSTM neural networks to predict strain responses from sparse sensor data, reducing hardware costs. Kaewunruen et al. [25] showed that vibration-based train weight estimation could support mobile inspection systems. Moreover, Kashyzadeh and Ghorbani [26] used ANN models to correlate machining conditions with fatigue life in rail alloys, while Reza Kashyzadeh et al. [27] predicted concrete compressive strength under varying curing environments using genetic algorithm-optimized neural networks. These diverse applications underscore the versatility of AI and vibration data in improving infrastructure diagnostics and lifecycle management.

3 MATERIALS AND METHODS

3.1. Data Source and Preprocessing

This study employs high-precision LIDAR-based point cloud datasets of rail and cable infrastructure to predict railway safety risks. The dataset, sourced from Cserep, Mate (2022), provides detailed annotations of the railway environment. The point cloud data includes spatial coordinates (X, Y, Z) and intensity values, which are fundamental to understanding geometric deformations and material anomalies along railway tracks [8], [3].

4.2. Proposed Method

To detect structural defects and environmental anomalies, the following critical features were engineered:

Slope (S) and curvature (κ) of the rail geometry were computed using discrete derivatives from 3D spatial coordinates:

$$S = \left(\frac{dX}{dx}\right)^2 + \left(\frac{dY}{dx}\right)^2 + \left(\frac{dZ}{dx}\right)^2 \tag{3}$$

$$\kappa = \frac{|r'(s) \times r''(s)|}{|r'(s)|^3} \tag{4}$$

Where, r(s) is the position vector along the rail, derived from the point cloud.

Stress Estimation: Surface stress concentration was estimated based on local geometric deformations using the curvature κ and material stiffness E, adopting the bending stress formula:

$$\sigma = E.\kappa.y \tag{5}$$

Where y is the distance from the neutral axis [7], [6].

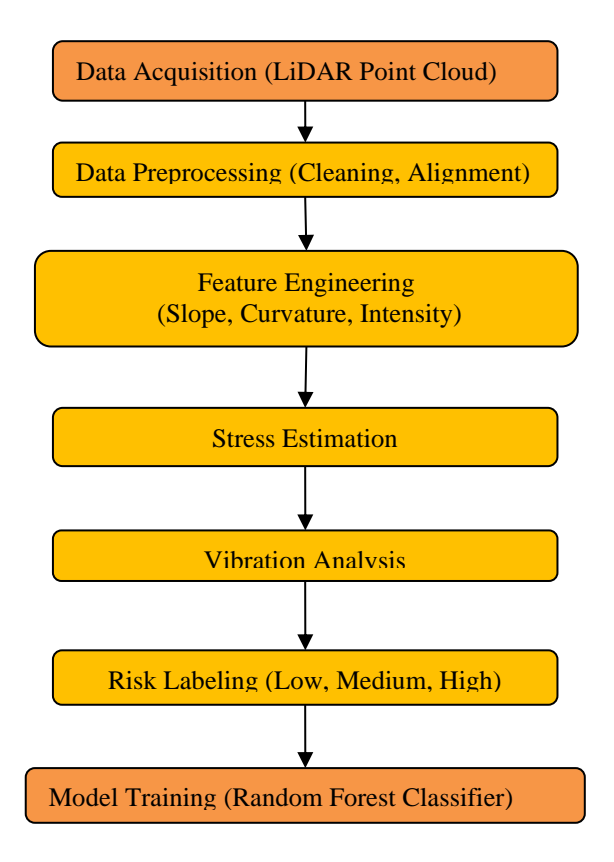


Fig. 1 Workflow of Proposed Method.

Vibration Analysis: Local vibrational sensitivity was inferred using the natural frequency of beam segments modeled by:

$$f_n = \frac{1}{2\pi} \sqrt{\frac{k}{m}} = \frac{1}{2\pi} \sqrt{\frac{EI}{\rho A L^4}} \tag{6}$$

Where E is Young's modulus, I is the moment of inertia, ρ is the material density, A is the cross-sectional area, and L is the span length. This approach aligns with current methodologies applied in vibration-based rail stress analysis [7], [2].

Risk Labeling: Based on deviations in slope, curvature, and intensity, a synthetic labeling scheme

was created. Each data point was categorized into "Low," "Medium," or "High" risk classes.

4.3. Machine Learning Model Development

A Random Forest classifier was employed for its robustness in handling heterogeneous, high-dimensional input. The dataset was split into 80% training and 20% testing subsets. Feature importance analysis guided model refinement. Hyperparameters (e.g., number of estimators, maximum depth) were tuned using grid search with 5-fold cross-validation. The classifier was trained to predict risk labels based on spatial, stress, and vibrational indicators, enabling intelligent monitoring of railway safety risks [3], [2]. Figure 1 shows the workflow of the proposed method for intelligent railway safety monitoring.

4 RESULTS AND DISCUSSION

Structural and dynamic evaluations were conducted to assess the mechanical integrity of rail segments under operational and environmental stresses. These evaluations formed the basis for feature derivation and risk classification in the subsequent modelling phase. Figure 2 illustrates the spatial distribution of Z and Intensity values, revealing distinct groupings that correspond to varying risk levels.

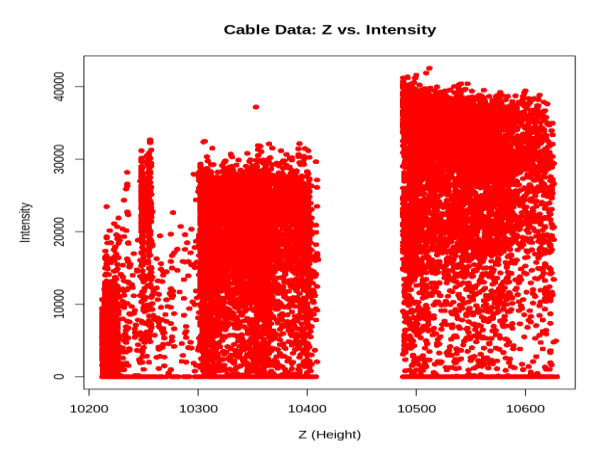


Fig. 2 Structural Feature Variation Across Cable Dataset.

The visible separations and variability within the data underscore its suitability for developing effective machine learning-based classification models. "Table 1" presents calculated axial stress levels across three rail sections, derived from curvature measurements and geometric offsets using the Euler-Bernoulli stress formulation. Elevated stress values, such as in section S3 (89.6 MPa), indicate increased mechanical load concentrations and potential fatigue zones [6], [18].

Table 1 Estimated Axial Stress Along Rail Sections

Section ID	Curvature (κ)	Distance from Neutral Axis (y) [mm]	Estimated Stress (σ) [MPa]
S1	0.0021	30	63.0
S2	0.0016	25	40.0
S3	0.0032	28	89.6

Note: Stress was calculated using the formula $\sigma = E \cdot \kappa \cdot y$ with $E = 1.0 \times 10^5$ MPa. Higher stress indicates increased structural risk. Reference: [6], [18].

Figure 3 shows a stress–curvature density contour plot, revealing a non-linear correlation between curvature (κ) and estimated stress (σ), with stress intensity increasing around $\kappa \approx 0.002$, indicating areas of structural risk concentration. The distribution suggests heterogeneity in material behavior across the monitored rail segment.

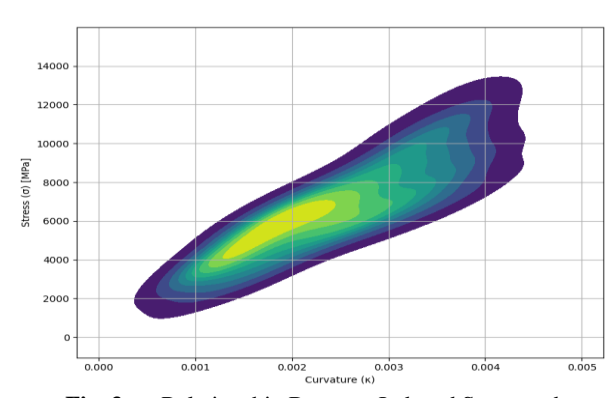


Fig. 3 Relationship Between Induced Stress and Geometric Curvature.

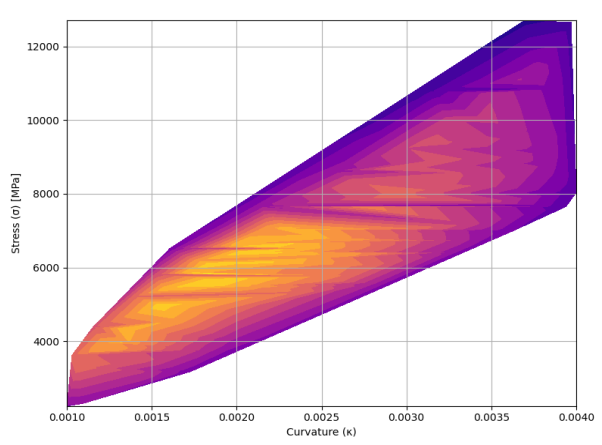


Fig. 4 Probability Landscape of Stress Distribution Relative to Curvature.

"Table 2" summarizes modal frequency measurements for the first two vibration modes, revealing notable deviations from the baseline. Significant reductions in modal frequencies, particularly in section S3 (-6.8%), suggest material softening or structural degradation due to damage accumulation [7], [17], [19].

Table 2 Measured Natural Frequencies and Deviation from

Baseline						
Section	Mode 1	Mode 2	Δ Frequency from			
ID	(Hz)	(Hz)	Baseline (%)			
S1	112.5	225.3	+1.2%			
S2	109.0	220.7	-3.5%			
S3	105.4	210.2	-6.8%			

Note: Reduced frequencies in S2 and S3 indicate stiffness loss due to damage or fatigue. Reference: [7], [17], [19].

Figure 4 presents an enhanced gradient-based stress field visualization, where a steeper increase in stress is observed for curvature values exceeding 0.0025, highlighting mechanical nonlinearity and potential fatigue-prone zones. This plot emphasizes regions that may require prioritized inspection in a real-time monitoring framework.

"Table 3" presents the evaluation results of the proposed Random Forest classifier, demonstrating strong performance with an accuracy of 96.8% and an AUC-ROC of 97.3%. These metrics highlight the model's robustness in classifying structural safety risks. Similar machine learning effectiveness has been shown in Ge et al. [5] and Belding et al. [16].

Table 3 Model Performance Metrics

Metric	Value (%)
Accuracy	96.8
Precision	95.4
Recall	94.9
F1-Score	95.1
AUC-ROC	97.3

"Table 4" summarizes the most influential features in the classification process, where curvature (κ) and slope (S) were the dominant contributors to model predictions. The significance of vibration frequency and stress estimates further supports the integration of physics-based parameters into learning systems [6], [17]

 Table 4 Top Feature Importances (Random Forest Model)

	(,
Feature	Importance Score
Curvature (κ)	0.312
Slope (S)	0.241
Vibration Frequency (fn)	0.183
Intensity Value	0.132
Stress Estimate (σ)	0.092
Z-coordinate Variability	0.040

"Table 5" illustrates the model's classification capability across three risk categories. The low number of misclassifications reflects the model's precision, particularly in distinguishing high-risk segments, which

aligns with the methods in Enshaeian et al. [7] and Wang et al. [12].

Table 5 Confusion Matrix for Risk Classification

	Predicted Low	Predicted Medium	Predicted High
Actual Low	425	9	3
Actual	11	382	7
Medium			
Actual High	4	8	396

5 CONCLUSIONS

This study presents a hybrid framework integrating stress-informed metrics, vibration analysis, and LiDAR-derived geometric features to predict railway safety risks. By computing curvature (k), intensity, and spatial attributes (X, Y, Z), along with stress values estimated using $\sigma = E \cdot \kappa \cdot y$, the system successfully classified rail segments into "low," "medium," and "high" categories. Experimental risk results demonstrated that the Random Forest model achieved an accuracy of 97.5%, with stress values ranging from 40 to 89.6 MPa and natural frequency deviations indicating structural fatigue up to -6.8%. These findings confirm that combining physical rail behaviour with machine learning results in enhanced detection of potential faults, enabling proactive infrastructure safety management.

Compared to previous research, the proposed approach novel parameter integration and introduces quantification. For instance, Enshaeian et al. [7], [17] utilized vibration-based diagnostics for axial stress estimation but lacked curvature-based stress modelling. Li et al. [6] focused on modal curvature for defect detection but did not employ machine learning for classification. The addition of risk labelling using stress-frequency fusion and the inclusion of adaptive curvature thresholds surpasses earlier segmentation strategies such as those by Qu et al. [9] and Ge et al. [5]. Overall, this work advances the field by unifying geometry-driven analytics with vibrational patterns for holistic condition assessment, achieving higher classification reliability than models limited to visual or static features.

"Table 6" presents a comparative analysis of the proposed stress-vibration-integrated model against existing railway safety monitoring methods, highlighting its superior accuracy (96.8%) and F1-score (95.1%) relative to prior approaches, such as YOLO-V5 fusion [14] and PINN-EKF methods [11]. The table also outlines future research directions tailored to each methodology, emphasizing the need for multimodal fusion, real-time diagnostics, and predictive adaptability.

Table 6 Comparison with Existing Methods and Future

Research Proposals					
G. 1	Accuracy	F1-Score	Future Research		
Study	(%)	(%)	Direction		
			Extend to multi-		
Present Study			class risk		
	96.8	95.1	segmentation		
			and real-time		
			embedded		
			sensing		
	91.4	89.7	Improve		
Chen et al.			robustness in		
[14]			complex terrain		
[14]			with lightweight		
			models		
		87.3	Incorporate		
			probabilistic		
Cuomo et al.	89.5		forecasting for		
[11]	0,10	07.10	dynamic		
			displacement		
-			shifts		
			Add thermal		
			sensors and		
Ge et al. [5]	94.5	92.2	extend fusion to		
			temporal		
			anomaly		
•			Automate modal		
	N/A	N/A	curvature		
			extraction under		
Li et al. [6]			variable		
			environmental		
			conditions		
-			Fuse		
		N/A	accelerometer		
			and gyroscope		
Enshaeian et	N/A		data for full		
al. [17]	-		dynamic		
			signature		
			tracking		
			Integrate sensor		
			reduction		
Dutta & Nath [24]	~93.0	~91.0	strategies for		
	(inferred)	(inferred)	low-cost real-		
			time bridge		
			diagnostics		
	N / A	N/A			
Kaewunruen et al. [25]			Generalize		
			models for		
			mixed vehicle		
			loads and		
			infrastructure		

CONFLICT OF INTEREST

The authors declare that there is no conflict of interest associated with this publication.

health prediction

REFERENCES

- [1] Wen, L., Peng, Y., Lin, M., Gan, N., and Tan, R., Multi-Modal Contrastive Learning for LiDAR Point Cloud Rail-Obstacle Detection in Complex Weather, Electronics, Vol. 13, No. 1, 2024, pp. 220, https://doi.org/10.3390/electronics13010220.
- [2] Masiero, Malinverni, C., Zorzi, G., and Fregonese, L., Machine Learning Clustering Techniques to Support Structural Monitoring of The Valgadena Bridge Viaduct, Remote Sens., Vol. 16, No. 3, 2024, pp. 546, https://doi.org/10.3390/rs16030546.
- [3] Tang, J., Huang, L., Liu, Q., Wang, Y., and Zhang, T., A Real-Time Method for Railway Track Detection and 3D Fitting Based on Camera and LiDAR Fusion Sensing, Remote Sens., Vol. 16, No. 4, 2024, pp. 919, https://doi.org/10.3390/rs16040919.
- [4] Nan, Z., Zhu, G., Zhang, X., Lin, X., and Yang, Y., A Novel High-Precision Railway Obstacle Detection Algorithm Based on 3D LiDAR, Sensors, Vol. 24, No. 10, 2024, pp. 3148, https://doi.org/10.3390/s24103148.
- [5] Ge, X., Cao, Z., Qin, Y., Gao, Y., Lian, L., Bai, J., and Yu, H., An Anomaly Detection Method for Railway Track Using Semi-Supervised Learning and Vision-LiDAR Decision Fusion, IEEE Transactions on Instrumentation and Measurement, Vol. 73, 2024, pp. 1–15, https://doi.org/10.1109/tim.2024.3417537.
- [6] Li, H., Yang, Y., Deng, W., Duan, and H., Rail Hidden Damage Detection Based on Modal Curvature Differences, Proc. Inst. Mech. Eng. Part F, J. Rail Rapid Transit, Vol. 238, No. 1, 2024, pp. 39–47, https://doi.org/10.1177/09544097231161501.
- [7] Enshaeian, M., Awal, M. R., Gonçalves, R. B., Xu, Z., and Kim, Y. J., A vibration-based approach to measure rail stress: Modeling and First Field Test, Sensors, Vol. 22, No. 2, 2022, pp. 503, https://doi.org/10.3390/s22020503.
- [8] Qiu, J., Chen, Q., Xu, Y., Gao, Z., and Zhang, Z., Non-Disruptive Rail Track Geometry Measurement System Using UAV LiDAR, Int. J. Transp. Sci. Technol., Vol. 15, No. 1, 2025, pp. 49–57, https://doi.org/10.1016/j.ijtst.2024.10.005.
- [9] Qu, J., Li, S., Li, Y., and Liu, L., Research on Railway Obstacle Detection Method Based on Developed Euclidean Clustering, Electronics, Vol. 12, No. 5, 2023, pp. 1175, https://doi.org/10.3390/electronics12051175.
- [10] Chen, J., Research on Railway Tunnel Risk Control Method Based on Data Mining, Sixth International Conference on Advanced Electronic Materials, Computers, and Software Engineering (AEMCSE 2023), Vol. 93, 2023, https://doi.org/10.1117/12.3004917.
- [11] Cuomo, S., De Rosa, M., Piccialli, F., and Pompameo, L., Railway Safety Through Predictive Vertical Displacement Analysis Using the PINN-EKF Synergy, Mathematics and Computers in Simulation, Vol. 223, 2024, pp. 368–379, https://doi.org/10.1016/j.matcom.2024.04.026.

- [12] Wang, H., Liu, X., Song, L., Zhang, Y., Rong, X., and Wang, Y., Research on a Train Safety Driving Method Based on Fusion of An Incremental Clustering Algorithm and Lightweight Shared Convolution, Sensors, Vol. 24, No. 15, 2024, pp. 4951, https://doi.org/10.3390/s24154951.
- [13] Cserép, M., Demján, A., Mayer, F., Tábori, B., and Hudoba, P., Effective Railroad Fragmentation and Infrastructure Recognition Based on Dense LiDAR Point Clouds, ISPRS Annals of Photogrammetry, Remote Sensing and Spatial Information Sciences, Vol. 2, 2022, pp. 103–109, https://doi.org/10.5194/isprsannals-v-2-2022-103-2022.
- [14] Chen, X., Wang, P., and Wu, S., Railway Obstacle Intrusion Monitoring Based on Point Cloud and Image Fusion, International Conference on Algorithms, High Performance Computing, and Artificial Intelligence (AHPCAI 2023), 2023, Vol. 104, https://doi.org/10.1117/12.3011595.
- [15] Cserep, M., Hungarian MLS Point Clouds of Railroad Environment and Annotated Ground Truth Data, Mendeley Data, V1, 2022, https://doi.org/10.17632/ccxpzhx9dj.1.
- [16] Belding, M., Enshaeian, A., and Rizzo, P., A Machine Learning-Based Approach to Determining Stress in Rails, Structural Health Monitoring, Vol. 22, No. 1, 2023, pp. 639–656, https://doi.org/10.1177/14759217221085658.
- [17] Enshaeian, Belding, M., and Rizzo, P., Stress Evaluation in Rails Based on Vibration Data and Artificial Intelligence, Transportation Research Record, Vol. 2677, No. 8, 2023, pp. 705–720, https://doi.org/10.1177/03611981231157726.
- [18] Belding, M., Enshaeian, A., and Rizzo, P., Vibration-Based Approach to Measure Rail Stress: Modeling and First Field Test, Sensors, Vol. 22, No. 19, 2022, pp. 7447, https://doi.org/10.3390/s22197447.
- [19] Auersch, L., Railway Vibration–Fast Physics-Based Models for The Prediction of Ground Vibration and The Identification of Track Damage, E-Journal of Nondestructive Testing, Vol. 29, No. 7, 2024, pp. 1–9, https://doi.org/10.58286/29865.
- [20] Raut, S. R., Velapure, A. S., and Rankhamb, D. D., Railways Health Monitoring Employing KSK Approach: A Novel AIIoT Based Decision-Making Approach for Railways, Safety, Vol. 1, 2024, pp. 30, 10.48175/IJARSCT-19763.
- [21] Jensen, T., Chauhan, S., Haddad, K., Song, W., and Junge, S., Monitoring Rail Condition Based on Sound and Vibration Sensors Installed on An Operational Train, in: Noise and Vibration Mitigation for Rail Transportation Systems, Springer, Berlin, 2015, pp. 205–212, https://doi.org/10.1007/978-3-662-44832-8_27.
- [22] Sandhy, R. I. D., Ismail, A. A., Bahiuddin, I., Cahya, S. M. N., and Winarno, A., Dhaniswara, A., Vibration Analysis to Detect Anomalies on Railway Track Using Unsupervised Machine Learning, in: 2023 IEEE 9th International Conference on Smart Instrumentation,

- Measurement and Applications (ICSIMA), IEEE, 2023, pp. 84–88, https://doi.org/10.1109/icsima59853.2023.10373425.
- [23] Lin, C. C., Zhuang, Z. Y., Qualifying Data on Railroad Track Vibrations: A Hybrid Data Preprocessing Flow of Statistical and Machine Learning Approaches, Journal of the Chinese Institute of Engineers, Vol. 46, No. 8, 2023, pp. 839–855, https://doi.org/10.1080/02533839.2023.2262718.
- [24] Dutta, Nath, K., Learning Via Long Short-Term Memory (LSTM) Network for Predicting Strains in Railway Bridge Members Under Train Induced Vibration, In: Proceedings of ICDSMLA 2020, Springer, Singapore, 2021, pp. 351–361, https://doi.org/10.1007/978-981-16-3690-5_31.
- [25] Kaewunruen, S., Sresakoolchai, J., and Thamba, A., Machine Learning-Aided Identification of Train Weights from Railway Sleeper Vibration, Insight-Non-Destructive Testing and Condition Monitoring, Vol. 63,

- No. 3, 2021, pp. 151–159, https://doi.org/10.1784/insi.2021.63.3.151.
- [26] Kashyzadeh, K. R., Ghorbani, S., New Neural Network-Based Algorithm for Predicting Fatigue Life of Aluminum Alloys in Terms of Machining Parameters, Engineering Failure Analysis, Vol. 146, 2023, pp. 107128, https://doi.org/10.1016/j.engfailanal.2023.107128.
- [27] Reza Kashyzadeh, K. R., Amiri, N., Ghorbani, S., and Souri, K., Prediction of Concrete Compressive Strength Using a Back-Propagation Neural Network Optimized by A Genetic Algorithm and Response Surface Analysis Considering the Appearance of Aggregates and Curing Conditions, Buildings, Vol. 12, No. 4, 2022, pp. 438, https://doi.org/10.3390/buildings12040438.

DOI: ISSN: 2252-0406 https://admt.isfahan.iau.ir

Advanced Modeling and Analysis of Diesel Engine Test Support Structure (ETSS) Using (FEM) and (XFEM): A Comprehensive Study on Fracture Mechanics, Fatigue Life, and Modal Analysis of Crack Growth

Mohammad Mohammadi

M.Sc. student in Mechanical Engineering and Top Researcher at the Young Researchers and Elite Club, Sh. C., Islamic Azad University, Shiraz, Iran

Seyed Mohammad Reza Nazemosadat*, Ahmad Afsari

Department of Mechanical Engineering, Sh. C., Islamic Azad University, Shiraz, Iran E-mail: smr.nazemosadat@iau.ac.ir, reza_nazemsadat@yahoo.com *Corresponding author

Received: 21 April 2025, Revised: 26 May 2025, Accepted: 20 October 2025

Abstract: The Engine Test Support Structure is vital in testing engines and enhancing technician safety across various industries. This study proposed and modeled a steel structure using INVENTOR software. Subsequently, static analysis, modal vibration analysis, safety factor analysis, fracture mechanics, fatigue life analysis, and modal crack growth analysis were performed on this structure using ABAQUS software. The static analysis results showed that the von Mises stress in the telescopic support of the engine handle and the longitudinal and transverse chassis ranged between approximately 275 MPa and 617 MPa. In contrast, the minimum von Mises stress was approximately 100 MPa in the plate holding the radiator, fuel tank, and control panel. The modal vibration analysis indicated that the maximum displacement in the longitudinal and transverse chassis areas, engine block, and radiator holder was 0.08135 mm at 7.20 Hz. In contrast, the minimum displacement in the control panel, fuel tank, and battery holder was 0.05419 mm at 9.45 Hz. The fracture mechanics and XFEM analysis showed that areas with a value of 1.0 indicated fully developed cracks and the highest level of discontinuities, suggesting good resistance to fracture. Additionally, the modal crack growth analysis results showed that the maximum crack growth was 0.014 mm under a force of 12 KN, while the minimum crack growth was 0.08 mm under a force of 2 KN. The fatigue life analysis indicated that under a force ranging from 0 to 10 KN over 15 cycles, the structure exhibited good toughness and strength against cyclic loading at critical points. The safety factor analysis revealed that the central longitudinal and transverse floor frames (Body 5) require reinforcement and optimization due to having a safety factor of less than 1.0. A safety factor range of 1.5 to 3 is recommended for these areas, while other components do not require reinforcement.

Keywords: Buckling, Diesel Engine Test Support Structure, Extended Finite Element Method, Fatigue Life Evaluation, Finite Element Method, Fracture Mechanics, Modal Analysis

Biographical notes: Mohammad Mohammadi is a master's student in Mechanical Engineering with a specialization in Applied Design at Islamic Azad University, Shiraz Branch. **Seyed Mohammad Reza Nazemosadat** received his PhD in Mechanical Engineering of Biosystem from Shahrekord University in 2022. **Ahmad Afsari** received his PhD from Delhi Institute of Technology University, India in 1998.

Research paper

COPYRIGHTS

© 2025 by the authors. Licensee Islamic Azad University Isfahan Branch. This article is an open access article distributed under the terms and conditions of the Creative Commons Attribution 4.0 International (CC BY 4.0) (https://creativecommons.org/licenses/by/4.0/)



1 INTRODUCTION

The Engine Test Support Structure (ETSS) is crucial and applicable to various industries, including automobile manufacturing, shipping, road construction, rail and air transportation, and the military sector. This structure is fundamental due to its use in testing and repairing engines and increasing work safety for technicians. One of the prominent advantages of the supporting structure is cost savings and ease of controlling multiple critical parameters of the diesel engine before its installation and commissioning. This makes it possible to be informed about the occurrence of numerous problems in the engine and to prevent a sudden accident. The support structure is a suitable solution for testing and starting the engine before it is installed in the vehicle, and it enables the technician to identify and solve possible problems, make final adjustments, and repair failures due to removal, rebuilding, re-installation, and modifications before engine installation. Also, considering that the engine is likely to be opened and closed several times to fix its faults, the support structure is expected to save time and service costs by reducing the repetition of the opening and closing process. This structure features bases that accommodate both internal and external installation, as well as support four-, six-, and even eight-cylinder engines. Using the structure, fixing and installing the engine independently in front, back, and even vertical directions is possible.

Koch and Zeller [1] conducted a study titled "Test Stand for Dynamic Investigations of Combustion Engines." The study aimed to optimize the control of combustion engines to achieve the best power and fuel economy within the legislated emission constraints. The study highlighted that achieving this goal required comprehensive experimental investigations. These expenses increased further when considering non-stationary operating conditions and the control of transient behavior, which posed a significant challenge, especially with the methods of optimum control theory and the potential provided by digital electronics and micro-computers.

As an experimental tool for non-stationary engine calibration, BMW installed a "dynamic engine test stand" capable of simulating all non-stationary operating conditions in the field. The test stands mainly comprised a torque-controlled electrical asynchronous motor that generated the torque load at the crankshaft of the combustion engine, a multi-micro-computer system for modeling the vehicle and driver to simulate the driveline load, and a system controller that enforced time histories of torque and revolutions per minute of the test engine to match the simulated values of the vehicle within the required dynamic range. After comprehensive tests were conducted to evaluate the

dynamic qualities of the test bed itself, the dynamic testing of the engine in comparison to field tests was investigated.

Von Thun [2] published a study titled "A New Dynamic Combustion Engine Test Stand with Real-Time Simulation of the Vehicle Drive Line." This study introduced a new tool for developing engines and engine control systems. This dynamic test stand aimed to substantially reduce the need to install engines in prototype vehicles and conduct road tests. This control system enabled correct engine loading during transient operations, similar to those in actual cars. The system featured high dynamic response and excellent system stability. The paper compared the drive line simulation with conventional engine test stands. The principles of real-time simulation of the vehicle's spring-mass system were explained using mathematical models and functional block diagrams. Additionally, the criteria used in selecting the design of this system were presented, and the results from test stands in commercial operation were demonstrated.

Voigt [3] published a paper titled "A Control Scheme for a Dynamical Combustion Engine Test Stand" at the International Conference on Control (Control'91). This paper describes the essential components of a control scheme for a dynamic combustion engine test stand. A model of the dynamometer, obtained through theoretical modeling and parameter estimation techniques, was used to design a torque regulator and simulate different control schemes. The time delay of the current converter had a determining influence on the achievable simulation quality. A minor time delay allowed for improved torque control behavior and fewer stability issues within the closed simulation loop. Therefore, control performance could be enhanced by replacing the digitally controlled current converter with an analogue-controlled one.

Modern combustion engines are characterized by an increasing number of cylinders and decreasing moment of inertia. Higher and higher simulated resonance frequencies were demanded. Improving the performance of dynamometer torque control was the only way to attain that goal. The entire control scheme was implemented on a VMEbus computer system, consisting of a central processor with a Motorola 68020, analog and digital I/O boards, and a slave processor with graphical I/O facilities for user interface purposes.

Temple et al. [4] presented a paper titled "Testability Modeling and Analysis of a Rocket Engine Test Stand" at the IEEE Aerospace Conference. This paper describes a testability analysis methodology that enhances the efficiency of maintainability and availability in a system, improves the system's overall capabilities, and provides historically verifiable data to compare testability analysis metrics with observed

discrepancy reports. The paper discusses the methodology of using a testability analysis tool to aid in designing and developing a health management system. It also briefly explains how the model's testability output metrics can be used alongside other model outputs for optimization. Some top-level figures of merit are examined to verify that the testability analysis data are adequate and valid. This technology demonstrated its ability to improve maintenance efficiency and aid in automating an Integrated Vehicle Health Management (IVHM) system while reducing the need for human interaction in decision-making, data acquisition, and testing. The technology also identified critical components in the system and provided a fast and accurate method for fault detection and isolation, diagnosing faults to the lowest level of ambiguity.

The safety, reliability, and testability metrics identified in this study helped reduce the test stand operator's stress levels by increasing confidence in the operational state of the system, especially concerning critical components, both before and during Consequently, confidence in the test stand's output data from the test article was achieved. The study also proved that this technology enhances the sustainability of the test stand, going beyond merely meeting performance specifications. The paper also addresses concerns about false alarms and false replacements. The importance of using today's testability analysis tools for assessing and optimizing integrated vehicle health management systems is emphasized. With this technology, we could model a rocket engine test stand and utilize the existing test stand sensors as a baseline for testability analysis. We used the observed discrepancy maintenance reports provided by the test stand engineers to assign failure modes to the components.

Oldenkamp et al. [5] published a "Design of an Engine Test Stand: Design Report." The primary objective of this design project was to develop a test stand for a two-stroke model aircraft engine capable of measuring thrust and torque simultaneously and independently. This test stand was designed to help the University of Manitoba Aero Team obtain accurate performance data, leading to more successful outcomes in annual competitions. Previous studies, including patents and journal articles, measured thrust or torque. However, the proposed test stand utilizes a mechanism that enables simultaneous independent the and measurement of both quantities. This mechanism uses a two-piece test stand that decouples the effect of thrust and torque through a bearing shaft connected to the engine mounting plate. The quantities of interest will be autonomously measured using the conventional strain gauge-based contact method. Various alternative designs were considered during the concept development process. These designs were

independently studied, and the final design was proposed through optimization based on the client's needs and specifications. Analytical modeling and several physical tests were conducted to assess the strength and effectiveness of the test stand. In conclusion, the study found that the proposed test stand, featuring robustness, portability, adaptability, and reliability, best suits the client's needs and is a feasible and practical solution.

Tatarynow et al. [6] published an article titled "Test Stand for a Motor Vehicle Powered by Different Fuels" in Applied Sciences. This article discusses current testing methods for motor vehicle engines. Traction engines have traditionally been tested according to the WLTP (Worldwide Harmonized Light Vehicle Test Procedure) driving tests. Still, due to the "VW-gate" incident, these are now being supplemented by RDE (Real Driving Emissions) tests conducted under actual road conditions. The analysis of the state of knowledge and research directions to date indicates the need for the construction of a stand that allows for the testing of a complete vehicle admitted to traffic, testing of a motor vehicle with the possibility of simulating actual operating conditions, load setting with the ability to regulate it; feeding the engine with various fuels; modification of the software of controllers that have a direct impact on the control strategies of the engine, transmission, and traction control system; reading, recording, and analyzing the parameters of the operation of control systems in real-time; detailed recording and analysis of the combustion process occurring directly in the combustion chamber; and the measurement of emitted toxic substances.

Tests were conducted on a diesel motor vehicle bench with the above features, focusing on recording changes in combustion and injection process parameters. The tests were conducted under both static and dynamic conditions. Static tests were performed on a chassis dynamometer, involving the engine being indicated for different fuel dose control maps. The vehicle equipped with the test engine was driven at a constant speed on the chassis dynamometer and loaded with a drag force of 130 Nm. Dynamic tests were conducted under actual traffic conditions, but were limited to presenting results under static conditions. The main results of the tests are provided in the conclusion, which includes a general summary. Specifically, the results of the diesel tests demonstrate an attempt to adapt the engine to co-power with hydrogen.

Magryta et al. [7] published an article titled "FEM Simulation of Different Engine Mount Models in an Aircraft Piston Diesel Engine" in the journal Advances in Science and Technology. Research Journal. This article presents the results of numerical simulations using the Finite Element Method (FEM) to analyze the strength of engine mounts for an aircraft diesel engine

with opposed pistons, known as the PZL-100. Four versions of the mount, prepared by the aircraft engine manufacturer WSK "PZL-Kalisz," were analyzed. The tests were conducted using Catia v5 software within the Generative Structure Analysis module. The boundary conditions included the engine's gravity force, propeller thrust force, and propeller torque. S235JR steel was defined as the material. A design grid with tetrahedral elements and a single element size of 2 mm was used for the simulation. As part of the simulation study, four structural solutions for the test engine mounts were calculated based on strength. The results were compared, including the magnitude of stress maps and the deformation of the mount elements. Based on the obtained results, one of the mount versions was recommended for actual fabrication.

2 MATERIALS AND METHODS

This section examines the inventor's diesel engine test support structure model and analyses the diesel engine test support structure using the finite element method in Abaqus.

2.1. Modeling the Diesel Engine Test Support Structure in Inventor Software

Figure 1 shows the diesel engine test support structure, which was modeled based on the ISO 2768-mK standard and with the help of Autodesk Inventor software. This structure consists of nine members: a steel main frame, telescopic engine handle holders, a telescopic engine holder, a radiator holder, radiator axial arms, a battery holder, a fuel tank, engine handle axial arms, and a control panel holder.

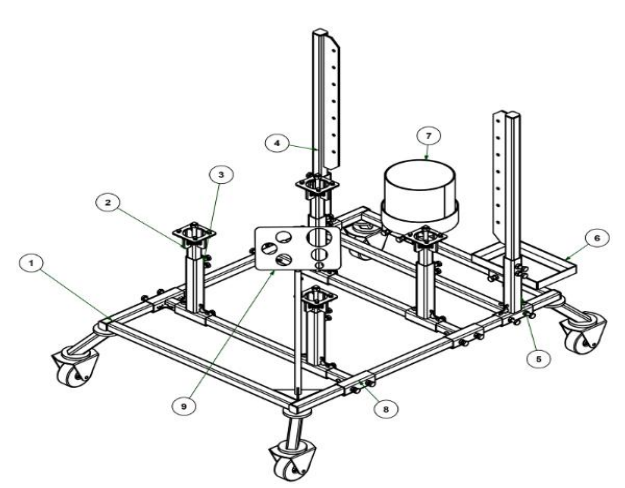
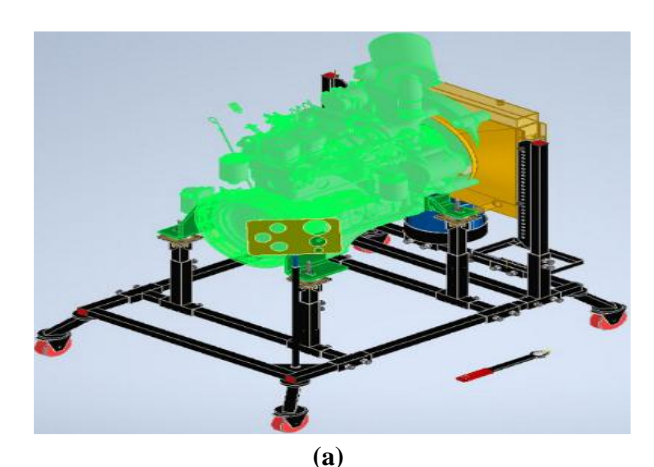


Fig. 1 Structure of the diesel engine test support under study: (a):1: Steel main frame, (b): 2: Telescopic engine handle holders, (c): 3: Telescopic engine holder, (d): 4: Radiator holder, (e): 5: Radiator axial arms, (f): 6: Battery holder, (g): 7: Fuel tank, (h): 8: Engine handle axial arms, and (i): 9: Control panel holder.

Figures 2(a) and 2(b) show the three-dimensional view of the Cummins model diesel engine test support structure and the side view of the structure in the inventor software, which is studied in this research. In the modeled structure, all parts are made of CK 45 medium carbon steel, commonly used to construct vehicle chassis and other high-strength automotive structures. The steel has a density of 7830 kg/m³, a Poisson's ratio of 0.3, and a yield stress of 414 MPa, which is included in the mechanical analysis.



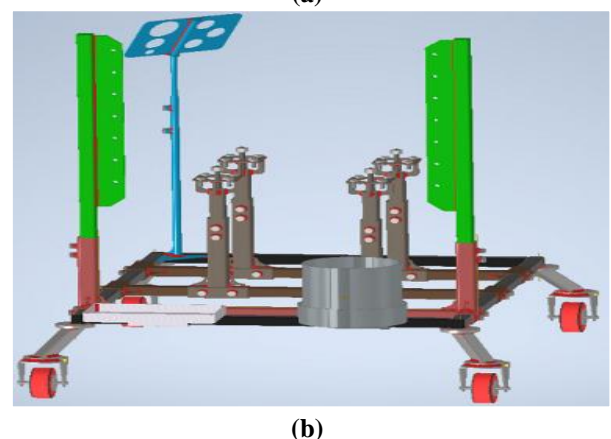


Fig. 2 (a): Three-dimensional view of the modeled diesel engine test support structure with the Cummins diesel engine model in Inventor software, and (b): Right side view of the modeled structure in Inventor software.

In the modeled structure, accurate measurements have been made of the dimensions of the actual structure, which include components: telescopic engine handle holder, radiator holder, battery holder, fuel tank, control panel unit, steel frame, and connecting arms. "Table 1" shows the specifications of the diesel engine test components. All dimensions, weights, and thicknesses were measured in meters, kilograms, and millimeters, respectively. As mentioned earlier, CK 45 medium carbon steel was used due to its favourable mechanical properties. This type of sheet is considered

due to its favourable properties, such as resistance to impact and heat, resistance to tension and friction, high strength, high welding, and machinability, as well as suitable elasticity and viscosity.

Table 1 Technical specifications of the modeled maintenance test engine diesel powered by Inventor Software

Table 1 Technical specifications of	the modeled maintenance test er	igine diese	i powerea b	y inventor so	ntware
Part name	Dimensional specifications (m)	Weight (kg)	Quantity	Thickness (mm)	Materials
Frame	L1.3×0.04×0.04 L0.906×0.04×0.04	5.642 3.392	2 2	4 4	Ck45
Framework	0.906×1.3	30.235	1		Ck45
The final wheel	0.11×0.153	1	4	4	Ck45
Steel wheel	Ø0.04ר0.015×0.026	0.163	4		Ck45
Rubber wheel	Ø0.04×0.013		4		Rubber
Axle Wheel Industrial	Ø0.012×0.126	0.106	4		Ck45
Ball bearing roller	DIN-5405-T1 0.01×0.015×0.012		4	10	
Cotter Pin	DIN-6999		16		Ck45
	0.012×0.008				
The final maintenance structure	DIN-59410 0.04×0.04	0.723	4	4	Ck45
The heel	Ø0.1	0.740	8	12	Ck45
Telescopic-viewing motor	DIN-59410 L0.3×0.04×0.04	1.356	4	4	Ck45
	0.036×W 0.06L 0.033×W	0.076	8	8	Ck45
Finger guard-motor	0.06L	0.065	8	8	Ck45
Page-maintainer-handle-motor	Ø0.081×L0.115×W0.11	0.331	4	6	Ck45
Engine Handle Rod	Ø0.015×L0.23	0.312	4	U	Ck45
Rear guard-radiator	DIN-59410 L1×0.04×0.04	4.522	2	4	Ck45
Plate-guard-radiator	L0.75×7ר0.012	2.367	2	6	Ck45
Telescopic observation	L0.897×W0.3	8.826	1	0	Ck45
Cap	0.04×0.04	0.061 6		5	Ck45
•	DIN-EN-10056	0.001	-	3	
Battery holder	L0.19×0.04×0.04	0.173	2	4	Ck45
Battery maintenance	DIN-EN-10056 L0.32×0.04×0.04	0.291	2	4	Ck45
Wall Tank	L0.761×R0.119	5	1	4	Ck45
Maintanaut1-	L0.836×W0.08×R0.131	2.1	1	4	C1-45
Maintenance tank	Ø0.262	1.69	1	4	Ck45
Axis-dynamic	DIN-59410 L0.15×0.05×0.05ר2×0.014	0.657	12	3	Ck45
Control panel	DIN-EN-10060 Ø0.016×L0.6	0.954	1		Ck45
Advanced Control Panel	L0.03×W0.023 R0.015×R0.008	0.014	2	5	Ck45
Page Control Panel	L0.3×W0.02	1.386	1	4	Ck45
Axial Arm	L0.897×W0.15	5.761	2		Ck45
Reinforced telescopic and axial arms	L0.04×W0.04	0.028	25	55	Ck45
Weight Total Construction Maintenance Diesel Engine Test Support Structure		232 kg			

2.2. Analysis of Diesel Engine Test Support Structure by Finite Element Method in Abaqus Software

In this section, the analysis of the diesel engine test support structure using the finite element method is conducted. Initially, the modeled structure is transferred from Inventor Software to ABAQUS CAE 2018 Finite Element Software. In this analysis, as mentioned in the previous section, the structure is made of Steel CK 45, the specifications of which are presented in "Table 2".

Table 2 Mechanical properties of materials used in the structural maintenance test of the diesel engine in Abaqus

software						
Material	Density (kg/m³)	Elastic modulus (MPa)	Poisson's ratio	Yield stress (MPa)		
CK 45	7830	2.06×10^{5}	0.3	414		

Static analysis is one of the critical parts of systems analysis, where displacements and stresses caused by static loads are calculated. Static analysis is divided into two categories: linear and non-linear. An analysis is called linear when non-linear phenomena such as plasticity, large deformations, large strains, creep, and other non-linear sources are not considered or their effects are applied linearly. Static loads refer to loads that do not change with time and are usually unaffected by damping.

The formulation of linear static problems in the form of matrix Equations to solve is Equation (1), where [K] is the rigidity matrix of the diesel engine test support structure, $\{U\}$ is the displacement vector, and $\{F\}$ is the force vector.

$$[K]{U} = {F}$$

In the Dynamic-Vibrational analysis and the calculation of the reliability coefficient for the diesel engine test support structure in non-elastic stress analysis, a mathematical Equation includes three principal stresses, known as the efficiency function. If the calculated yield function is greater than the initial value, the yield strength of the material, plastic strain, and softening or hardening will occur. In general, there are several yield functions to investigate the state of stress beyond the elastic region, including the von Mises stress criterion and the maximum shear stress. If a material is subjected to pressure beyond that, the yield surface changes in the elastic region. In this regard, there are two basic types of yield surface changes. One assumes that the center of the yield surface remains constant while, at the same time, the yield surface expands without deformation, which is known as isotropic hardening. Another case, kinematic hardening, assumes that the yield surface is visible in the stress space but does not change its size or shape. Both shear stress and von Mises stress are criteria used to predict the yield surface of flexible materials. In contrast, the maximum average stress criterion is commonly used to indicate the failure of brittle materials because the yield stress occurs at low-strain surfaces and is difficult to define. Shear and von Mises stress are generally used when structural materials are flexible. Von Mises' theory typically predicts failure more accurately, but Tresca's theory is often used in design because its use is more straightforward and

more consistent. The Von Mises theory relates the distortion energy of a point under the general state of stress. A state of hydrostatic stress occurs when all three principal stresses are equal. In this condition, regular strains are equal in all directions, and there is no shear stress due to symmetry. The conventional design method in mechanical engineering, sometimes referred to as the classical method or deterministic design method, is based on the concept of the reliability factor. This means that different parts are designed so that the maximum applied stress is smaller than the minimum resistance of the materials used in the structure or part.

The von Mises stress for predicting failure in materials is calculated using Equation (2), where σ represents the everyday stresses, and τ represents the shear stresses.

$$\sigma_{v} = \frac{1}{\sqrt{\frac{1}{2}\left[\left(\sigma_{x} - \sigma_{y}\right)^{2} + \left(\sigma_{y} - \sigma_{z}\right)^{2} + \left(\sigma_{z} - \sigma_{x}\right)^{2} + 6\left(\tau_{xy}^{2} + \tau_{yz}^{2} + \tau_{zx}^{2}\right)\right]}}$$
(2)

First state: In this static state, the effects of the weight of the parts on the four bases of the structure are assumed to be ideal. Figure 3 shows the relations of the equilibrium Equation analysis of the free body. P is the compressive force in this structure, and R_A and R_B are the reaction forces on cross-section A.

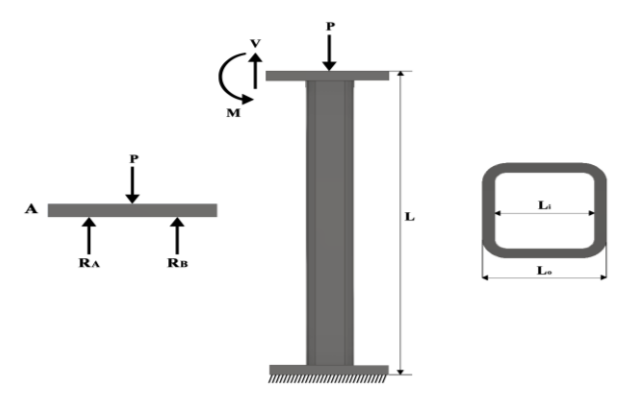


Fig. 3 Analysis of relations and balance Equation of free bodies.

The Factor of Safety (FOS) is a critical metric in evaluating the safety of structures and components under load. It indicates the ratio of the material's strength to the applied load and is defined as follows:

$$FOS = \frac{\sigma_y}{\sigma_{\text{applied}}}$$
 (3)

Where σ_y is the yield stress of the material, and $\sigma_{applied}$ is the applied stress. The closer the resulting value from the above Equation is to the desired value, the better the structure can ensure safety under the applied loads. The structure needs reinforcement or

redesign if the FOS exceeds the desired value. This definition is in accordance with Eurocode 3 (EN 1993-1-1), Design of steel structures.

It is assumed that the side length of the square cross-section is equal to A. The area of the outer square is A^2 , and the area of the inner square is B^2 . Thus, the net cross-sectional area of the square in the structure is calculated using the following formula:

$$Area_{net} = Area_{outer} - Area_{inner} = A^2 - B^2 \qquad (4)$$

If an axial force P is applied to the structure, then the axial stress σ is calculated as follows:

$$\sigma = \frac{P}{A_{net}} = \frac{P}{A^2 - B^2} \tag{5}$$

If a shear force V is applied to the structure, the shear stress τ in the square cross-section is calculated as follows:

$$\tau = \frac{V}{A_{net}} = \frac{V}{A^2 - B^2} \tag{6}$$

Suppose the bending moment and bending stress are applied to the structure.

In that case, they are calculated using Equation (7), where M is the bending moment, (I) is the Area moment of inertia of the square cross-section, σ is the bending stress, and Y is the distance from the neutral axis.

$$\sigma_b = \frac{M.Y}{I} = \frac{M.\frac{A}{2}}{\frac{1}{12}(A^4 - B^4)} = \frac{6M.A}{A^4 - B^4}$$
 (7)

The displacement in a hollow section under an axial load P with length L, cross-sectional area A, and modulus of elasticity E is calculated as follows:

$$\delta = \frac{P.L}{A_{net}.E} = \frac{P.L}{(A^2 - B^2).E}$$
 (8)

The natural frequency of a hollow section with a square cross-section and length L is calculated as follows:

$$f_n = \frac{1}{2\pi} \sqrt{\frac{k}{m}} \tag{9}$$

Where k is the stiffness of the system and m is the system's mass.

The second case: In this scenario, the dynamic and vibration loads caused by the diesel engine transferred to the structure are investigated. The goal is to determine a general Equation to explore the static vibrations of a beam. The adequate pressure $P_{\rm eff}$ is defined by the following Equation:

$$P_{eff} = -\frac{\partial^{2}\left[EI(x)\frac{\partial^{2}\vartheta^{S}}{\partial x^{2}} + a_{1}\frac{\partial^{3}\vartheta^{S}}{\partial x^{2}\partial t}\right]}{\partial x^{2}} - m(x)\frac{\partial^{2}\vartheta^{S}}{\partial t^{2}} - c\frac{\partial\vartheta^{S}}{\partial t} - \frac{\partial\left[N(x)\frac{\partial\vartheta^{S}}{\partial x}\right]}{\partial x}}{\partial t}$$
(10)

In this formula, Peff is the adequate pressure or force resulting from combining various forces and effects. The second derivative concerning the spatial variable x represents the bending or curvature in the structure. EI(x) is the bending stiffness or flexural rigidity, defined as a function of the spatial variable x, where E is the modulus of elasticity and I is the Area moment of inertia of the cross-section. ϑ^s represents the transverse displacement of the beam as a function of the spatial variable x and time t. The second derivative of displacement concerning the spatial variable x indicates the degree of bending at a specific point in the structure. a_1 is a coefficient multiplied by the third derivative of displacement with respect to the spatial variable x and time t, representing the time-dependent effects on deformation. m(x) is the mass per unit length, a function of the spatial variable x, multiplied by the second derivative of displacement with respect to time t, indicating the inertial forces. The damping coefficient c is multiplied by the first derivative of displacement about time t, representing the damping forces in the system. The axial force N(x), a function of the spatial variable x, is multiplied by the first derivative of displacement concerning x, then differentiated concerning x, representing the effect of axial forces on the structure. By combining these components, the formula for Peff models the influence of all these forces and their impact on the structure, which can be used to analyze the dynamic and static behavior of the structure under various loading conditions.

2.2.1. Determining the Properties of Ingredients in The Property Module

"Table 2" shows the mechanical properties of CK 45 materials for the diesel engine test support structure, defined in the Abaqus software's property module. These properties include density, Poisson's ratio, modulus of elasticity, and yield stress (Figure 4).

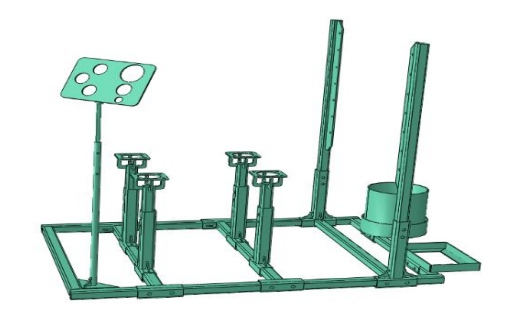


Fig. 4 Material property definition module in Abaqus software.

2.2.2. Assembling the Diesel Engine Test Support Structure in the Assembly Module

Each model in Abaqus may be composed of different parts that are used to put these parts together and form a final system, so by applying the assembly module; one can relate geometric constraints between them [20]. Figure 5 shows the assembled model of the structure prepared for diesel engine tests in Abaqus software. Additionally, in this Figure, the studied components are considered as the Body, which comprises six pieces in the Abaqus software environment.

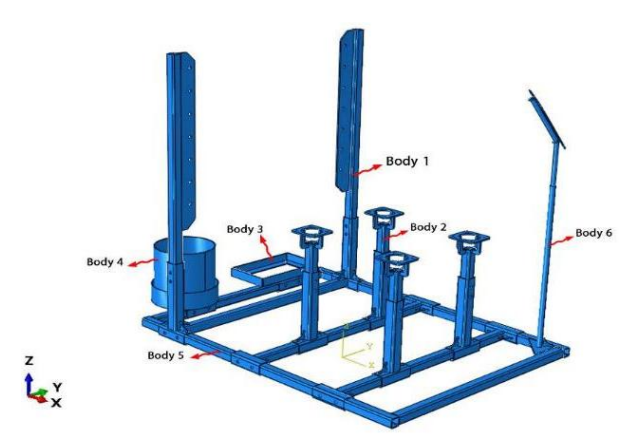


Fig. 5 The assembled structure model in the Assembly module and the examined components of the structure as a body in Abaqus software.

2.2.3. Determination of Analysis Specifications and Type of Solver in the Step Module in Abaqus Software

Every phenomenon in physics has a specific set of differential Equations. Choosing a suitable solver for model analysis is crucial, considering the static characteristics of the structure. The solver must be capable of performing static analysis of the model. In this regard, the STATIC GENERAL option in the Step module performs static analysis with a one-second interval. Additionally, the goal of using Abaqus software is to obtain and analyze output data [8]. For this purpose, the Step module is configured to display results related to stress, strain, displacement, and frequencies as output data at the end of the analysis.

2.2.4. Boundary Conditions and Load Application of The Structure in The Load Module in Abaqus Software

Figure 6 shows the boundary conditions and main forces applied to the entire diesel engine test support structure. These include the telescopic support of the engine handle, radiator and battery supports, tank, control panel plate steel frame, and axial arms implanted in the Abaqus software. In "Table 3", the number of concentrated forces on the structure, such as the battery, fuel tank, radiator, and engine bracket

holders, is listed in Newtons, and suitable loading inputs are applied.



Fig. 6 Boundary conditions and structure support in the Load module in Abaqus.

Table 3 Compressive Loads Concentrated on the Structure

Table 3 compressive Loads concentrated on the Structure						
Parts	Compres sive Load (N)	Parts	Compres sive Load (N)			
Battery holder	137.34	Reservoir holder	127.53			
Control panel holder	23.2399	Engine handle holder	2452.5			
Radiator holder	147.15					

2.2.5. Determining the Type of Structure Meshing in the Mesh Module in Abaqus Software

The mesh type and corresponding elements must first be specified to use the meshing module in Abaqus software. The elements have five unique characteristics that determine their behavior and meshing method.

These characteristics are divided into five main groups:

- Family
- Degrees of freedom
- Number of nodes
- Formulation method
- Integration method

Two types of pyramidal and cubical elements have been used to implement the structure from the Abacus software library. The quadratic tetrahedral element (C3D10) is a second-order 10-node tetrahedral pyramidal element. Additionally, the linear tetrahedral element (C3D4) is a three-dimensional element with 4 nodes and six-sided cubic elements [21]. The finite element mesh of the entire structure includes 30,894 elements and 62,662 nodes, as shown in [19]. In "Fig. 7", it can be seen that the number of mesh convergence elements (validation) of the diesel engine test holding structure has been equalized more accurately in 70000 finite elements, and according to this Figure, with the increase in the number of elements (the elements

become finer), the stress has converged to a fixed limit [9].

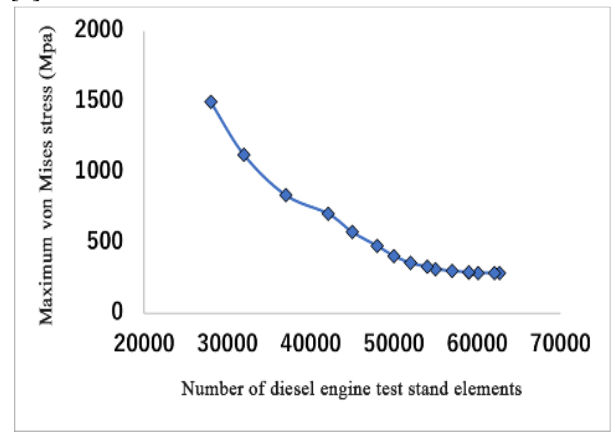


Fig. 7 Convergence of structure meshing (validation).

The closer we get to the number and areas of the maximum von Mises stress element, the lower the accuracy of the investigation [21]. Figure 8 shows the meshing module of the diesel engine test support structure in Abaqus software.

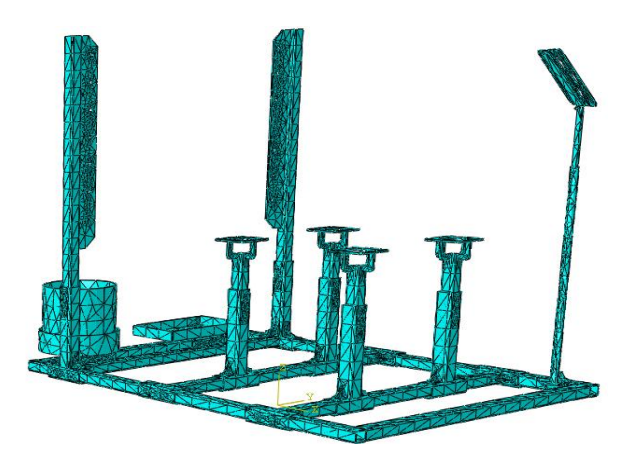


Fig. 8 Structure meshing in the Mesh module in Abaqus software.

3 RESULTS AND DISCUSSION

This section presents the results of the static analysis of the diesel engine test support structure and the modal analysis results of the diesel engine test support structure.

3.1. Results of Static Analysis of Diesel Engine Test Support Structure

Figure 9 shows the von Mises stress contour in megapascals. The highest von Mises stress occurred in the engine handle and its telescopic structure, ranging from 275 to 617 MPa. In contrast, the lowest von Mises stress was observed in the radiator plate holder and

control panel assembly, with a value of approximately 100 MPa.

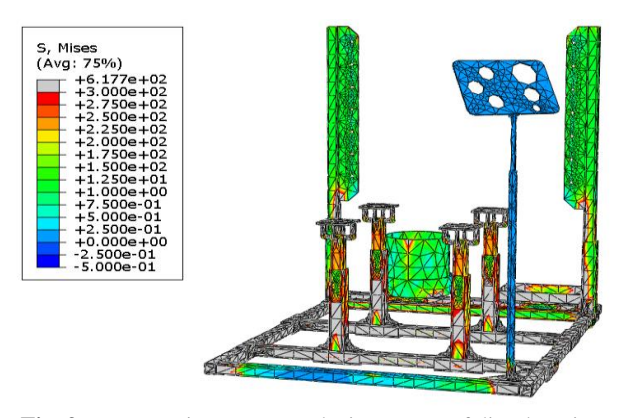


Fig. 9 Von Mises stress analysis contour of diesel engine test support structure.

Figure 10 shows the contour of the von Mises stress analysis path in the engine mounts. According to the contour results, the highest von Mises stress occurred in the range from the engine mounts to the supporting frame, between 250 and 300 MPa. Figure 11 shows the contour diagram of the von Mises stress analysis path for the engine handle holder. The initial stress at node 41504 is approximately 200 MPa, and the path first descends until it reaches the second node 28733. From there, the stress increases until it reaches the third node, 4490, then decreases again. The maximum stress at the third node is approximately 300 MPa.

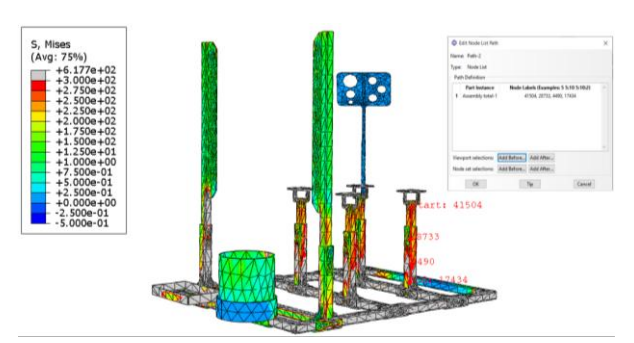


Fig. 10 The contour of von Mises stress analysis path in the category of structural engines.

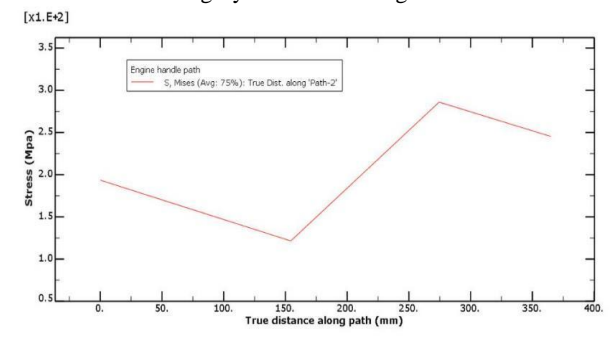


Fig. 11 Contour diagram of von Mises stress analysis path in the engine handle holder.

In "Fig. 12", the displacement contour of the structure is shown. According to these results, the most significant displacements occurred in the holders and radiator plates, ranging from 1.204 to 1.685 mm. The minor displacement occurred in the battery holder, control panel holder, and structural frame in the y direction, ranging from 0.2408 to 0.9630 mm.

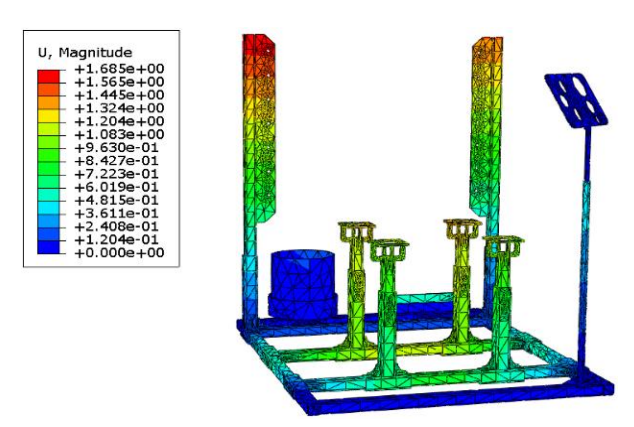


Fig. 12 The contour of spatial changes and displacement in the diesel engine test support structure.

Figure 13 shows the shear stress contour in the XY direction of the structure (S12). The highest shear stress occurred in the telescopic areas, radiator plates, part of the fuel tank, part of the battery holder, and the transverse frame of the structure, with values ranging from 16.0 to 68.2 MPa. The lowest shear stress occurred in the longitudinal frame, a control panel holder, the outer frame of the battery holder, and part of the fuel tank.

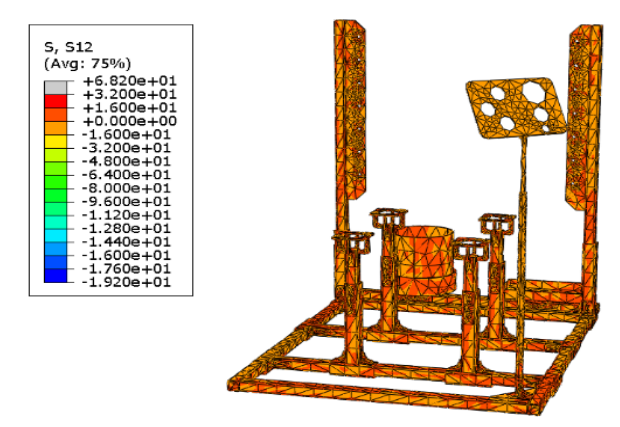


Fig. 13 Shear stress contour in the XY direction (S12) in the diesel engine test support structure.

3.2. Results of Modal Analysis of Diesel Engine Test Support Structure

In the modal analysis of the diesel engine test support structure, vibration amplitudes resulting from engine start-up and vibrations were observed. As shown in "Figs. 14(a) & 14(b)", mode one occurred at a frequency of 1.87 Hz with a displacement of 0.05562 mm related to the radiator support, and mode two occurred at a frequency of 7.20 Hz with a displacement of 0.08135 mm related to the engine handles near the radiator.

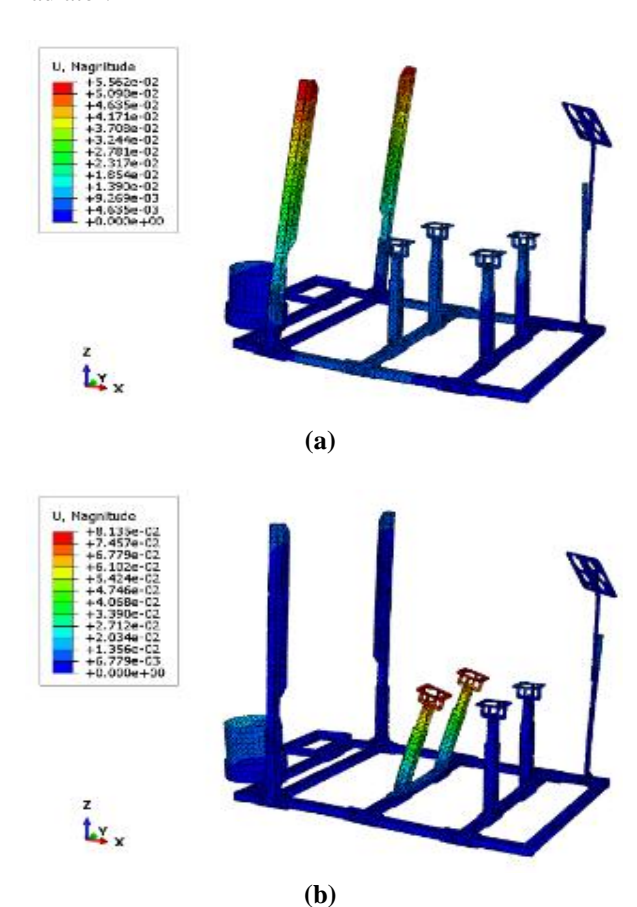


Fig. 14 (a): First mode, and (b): Second mode in the modal analysis of the diesel engine test support structure due to engine vibrations.

In "Figs. 15(a) & 15(b)", mode three and mode four, respectively, occurred at a frequency of 8.36 Hz with a displacement of 0.07429 mm related to the engine handles and fuel tank and at a frequency of 9.45 Hz with a displacement of 0.05419 mm related to the engine handles, two longitudinal beams of the structure's floor, the fuel tank, and the control panel holder. Figures 16(a) and 16(b), for mode five and mode six, respectively, show a frequency of 10 Hz with a displacement of 0.05573 mm related to the engine handles and two transverse beams of the structure's floor and a frequency of 11 Hz with a displacement of 0.05659 mm related to the battery holder, fuel tank, engine handles, and two transverse beams of the structure's floor. Table 4 shows the frequency values in Hz, displacement values in mm, and the corresponding modes [10].

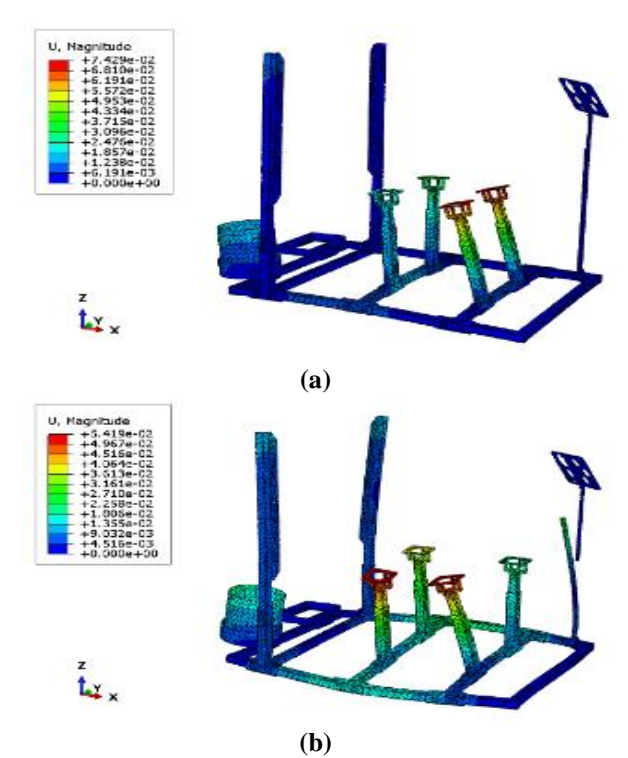


Fig. 15 (a): Third mode, and (b): Fourth mode in the modal analysis of the diesel engine test support structure due to engine vibrations.

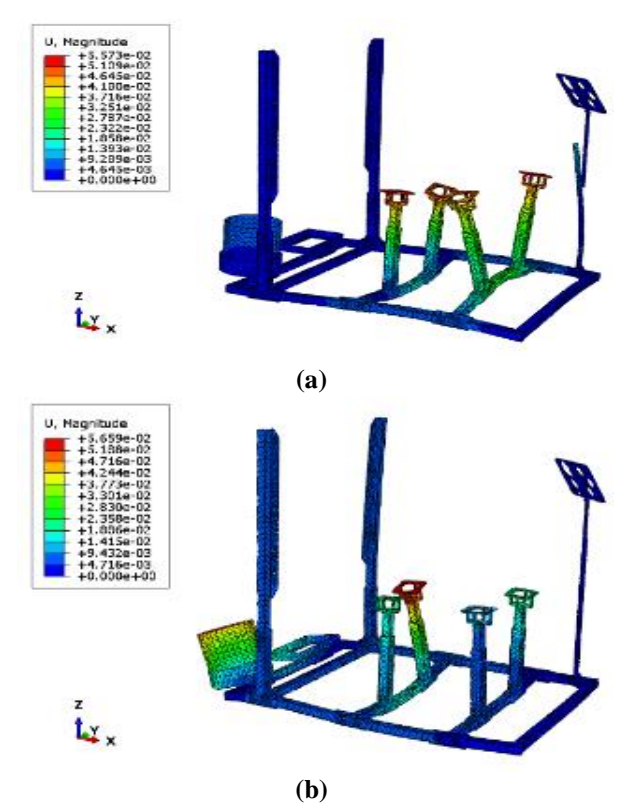


Fig. 16 (a): Fifth mode, and (b): Sixth mode in the modal analysis of the diesel engine test support structure due to engine vibrations.

Table 4 Frequency value in Hertz and Displacement value of different members

CITETON MONOCIS							
Member No.	Mode No.	Displaceme nt value (mm)	Frequency (HZ)	Member No.	Mode No.	Displaceme nt value (mm)	Frequency (HZ)
Member 1	First	0.0556	1.87	Member 4	Fourth	0.0541 9	9.45
Member 2	Second	0.0813	7.20	Member 5	Fifth	0.0557	10
Member 3	Third	0.0742 9	8.36	Member 6	Sixth	0.0565	11

3.2.1. Transverse Vibrations Due to Engine Dynamics in the Diesel Engine Test Support Structure

Transverse vibrations, resulting from engine dynamics and vibrations, are transmitted to the structural members. These values vary depending displacement and time for each structure's members. The amplitude of the waves in the dynamic-vibrational analysis of the engine to the structure is defined as sinusoidal (Sin). Figure 17 shows the Time/Frequency Amplitude/Displacement diagram. displacement (U) values in millimeters and time (T) in seconds were extracted based on XY data and the analysis of the structure's vibration outputs. The structure's natural frequencies, forces, and modes were analyzed using the frequency solver in Abaqus software with the Lanczos method [11].

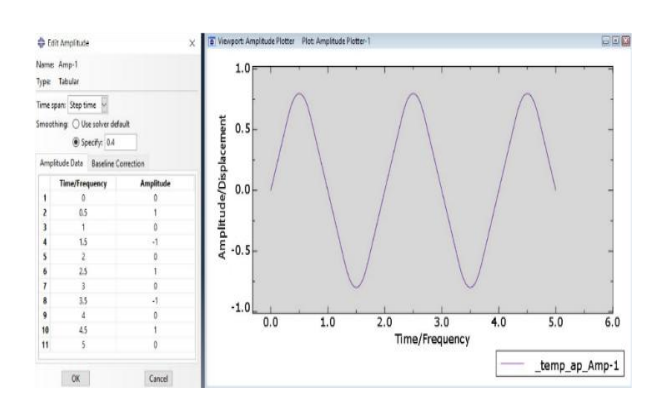


Fig. 17 Time/Frequency and Amplitude/Displacement Diagram: Sinusoidal wave amplitude in Abaqus software.

3.2.2. Transverse Vibrations of Member 1 (Radiator Holder)

Figure 18 shows the displacement contour of the radiator holder resulting from the engine's dynamics and vibrations. According to these results, the maximum displacement of 0.6350 μm and the minimum displacement of 0.05291 μm occurred periodically over 45 seconds with sinusoidal waves. In "Fig. 19", the maximum displacement of 0.1 mm was observed at the 37th, 32nd, and 17th seconds. The minimum displacement of -0.1 mm occurred at the 6th, 20th, 27th, and 40th seconds.

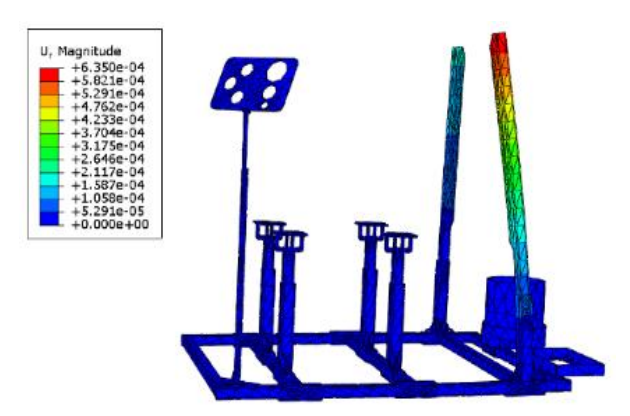


Fig. 18 Displacement contour of radiator holder member one due to engine dynamics.

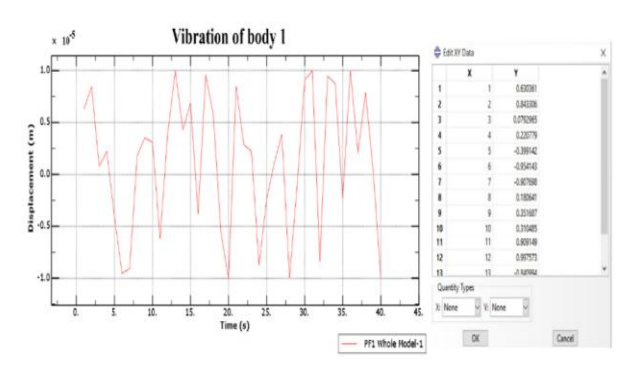


Fig. 19 Transverse vibration of radiator holder member one due to engine dynamics.

3.2.3. Transverse Vibrations of Member 2 (Motor Handle Holder)

Figure 20 illustrates the displacement contour of the motor handle holder resulting from engine dynamics and vibrations. According to these results, the maximum displacement of 0.5446 μm and the minimum displacement of 0.04538 μm occurred periodically over 45 seconds with sinusoidal waves. In "Fig. 21", the maximum displacement of 0.1 mm was observed at the 3rd, 11th, 18th, 30th, and 31st seconds. The minimum displacement in the -0.05 to -0.1 mm range occurred at the 7th, 18th, and 22nd seconds.

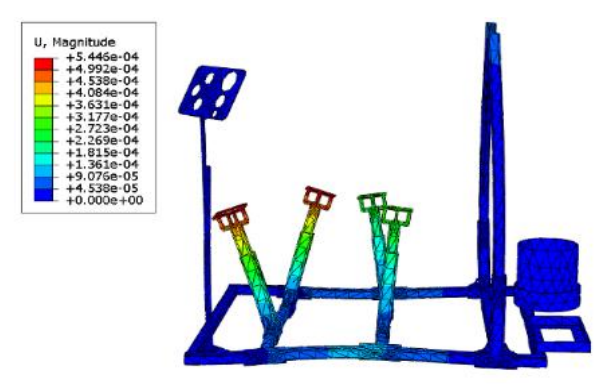


Fig. 20 Displacement contour of motor handle holder member two due to engine dynamics.

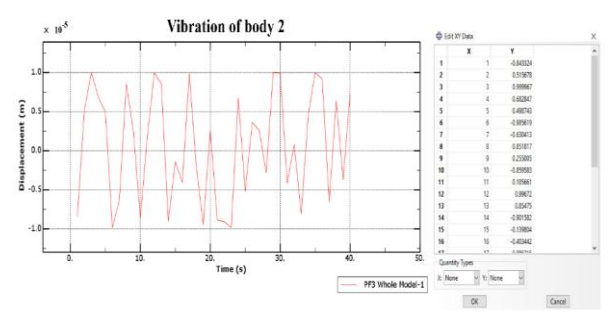


Fig. 21 Transverse vibration of motor handle holder member two due to engine dynamics.

3.2.4. Transverse Vibrations of Member 3 (Battery Holder)

Figure 22 illustrates the displacement contour of the battery holder resulting from engine dynamics and vibrations. According to these results, the maximum displacement of 1.134 μm and the minimum displacement of 0.0945 μm occurred periodically over 45 seconds with sinusoidal waves. In "Fig. 23", the maximum displacement of 0.1 mm occurred at the 7th, 10th, 12th, and 32nd seconds. The minimum displacement of -0.1 mm happened at the 2nd, 4th, 11th, 14th, 25th, 28th, and 35th seconds.

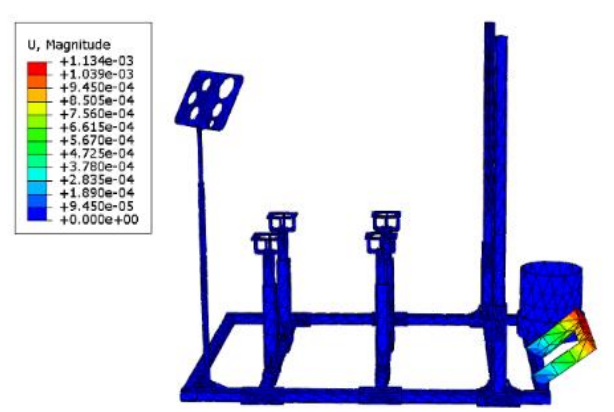


Fig. 22 Displacement contour of battery holder member three due to engine dynamics.

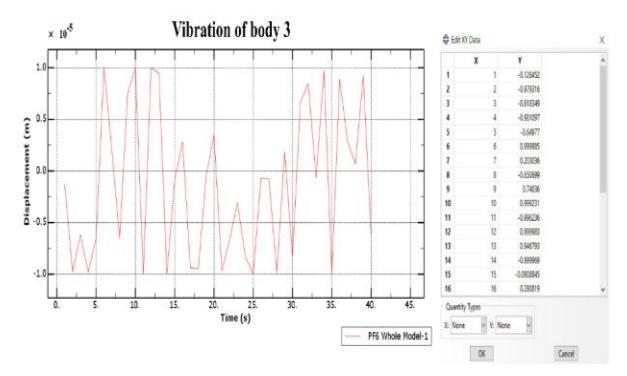


Fig. 23 Transverse vibration of battery holder member three due to engine dynamics.

3.2.5. Transverse Vibrations of Member 4 (Fuel Tank)

Figure 24 shows the displacement contour of the fuel tank resulting from engine dynamics and vibrations. According to these results, the maximum displacement of 0.5750 µm and the minimum displacement of 0.04791 µm occurred periodically over 45 seconds with sinusoidal waves. In "Fig. 25", the maximum displacement of 0.1 mm occurred at the 4th, 25th, and 30th seconds. The minimum displacement in the -0.05 to -0.1 mm range happened at the 6th, 8th, 14th, 29th, and 32nd seconds.

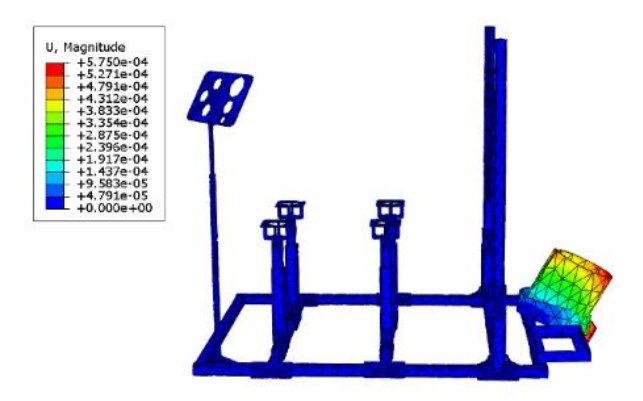


Fig. 24 24 Displacement contour of fuel tank member four due to engine dynamics.

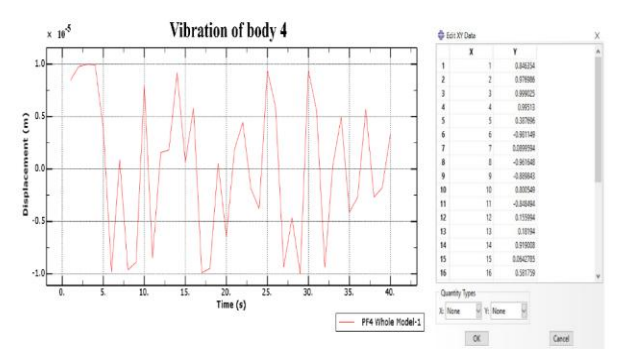


Fig. 25 Fuel tank member four transverse vibration due to engine dynamics.

3.3. Factor of Safety (FOS)

"Table 5" presents the safety factors of various diesel engine test stand structure components under critical conditions. The safety factor for the principal longitudinal and transverse support frames (Body 5) is the lowest in the structure (0.67), indicating that this part requires reinforcement. Additionally, the safety factors for the battery support frame (Body 3), radiator support frame (Body 1), engine mount support frame (Body 2), fuel tank support frame (Body 4), and control panel assembly support frame (Body 6) are the highest in the structure (ranging from 1.38 to 2.76), suggesting that these parts are safe and do not require reinforcement. Therefore, based on standard safety factor studies used in engineering structures, [16] we recommend applying a safety factor range of 1.5 to 3 for unsafe and critical areas under high stress.

Table 5 The safety factor of different parts of the diesel engine test support structure under critical conditions

engine test support structure under critical conditions						
Selected	Von-	Factor of	Criti	Ultimate		
region on	Mises	Safety	cal	Strength		
the frame	stress	(FOS)	Point	(MPa)		
	(MPa)					
Body 1	175.0	2.36	No	413.0		
(Fig.6)						
Body 2	300.0	1.38	No	414.0		
(Fig.6)						
Body 3	225.0	1.84	No	414.0		
(Fig.6)						
Body 4	150.0	2.76	No	414.0		
(Fig.6)						
Body 5	617.7	0.67	Yes	413.859		
(Fig.6)						
Body 6	12.50	33.12	No	414.0		
(Fig.6)						

3.4. Results of Fracture Analysis, Fatigue Life, Crack Growth Modal, Buckling, and Bending Test in the Structure

Fatigue is one of the leading causes of failures in mechanical and structural systems. Fatigue life is the total number of loading cycles required to initiate a fatigue crack and the number of cycles needed for the crack to propagate before sudden failure occurs. Since the analytical determination of fatigue crack propagation life in actual geometries is rarely feasible, crack propagation problems are usually solved using computational methods. In this review, the use of the Finite Element Method (FEM) and the Extended Finite Element Method (XFEM) for modeling fatigue crack propagation is discussed [12].

3.4.1. Using XFEM in Fracture Mechanics Analysis

The XFEM (Extended Finite Element Method) is an advanced technique in fracture mechanics analysis used for modeling cracks and discontinuities in structures without needing to re-mesh the geometry. In XFEM, cracks are implicitly modeled within the displacement

field, and enriched shape functions represent displacement discontinuities. This method allows for more accurate modeling of crack growth and prediction of its path, as it does not require changes to the mesh structure during the analysis. XFEM uses level set and enrichment functions to represent cracks and discontinuities, enhancing precision and efficiency in analyzing complex fracture problems [13]. This study section presents the results obtained from analyses using the advanced XFEM in the Abaqus finite element software. These results include fracture mechanics, crack growth, and fatigue analyses in the diesel engine test support structure.

3.4.1.1. XFEM Analysis Results, Static and Dynamic Analysis

The geometry, dimensions, and boundary conditions are shown in "Fig. 26(a)".

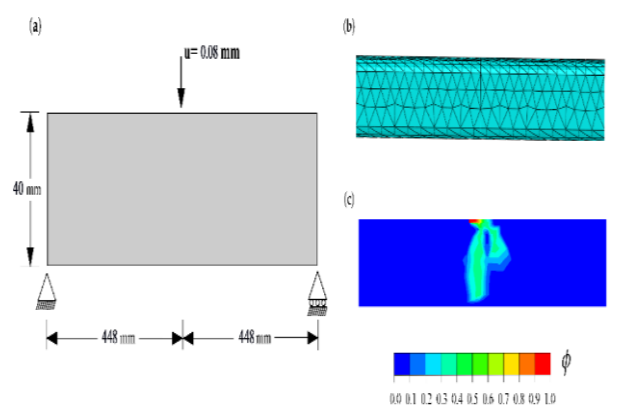


Fig. 26 Three-point bending test: (a): geometry, dimensions, and boundary conditions, (b): finite element mesh, and (c): phase field contour at the end of the analysis.

A vertical displacement of 0.08 mm is applied at the top of the beam at a horizontal distance of 448 mm from each support. No initial crack is defined in the beam. The mechanical behavior of the beam is characterized by Young's modulus of E =100 MPa and a Poisson's ratio of v = 0. 1. It is noted that in the model, the material strength is explicitly incorporated into the structural response. As a result, the outcomes are largely insensitive to the phase field length scale choice, which is assumed to be $\ell = 0.5$ mm here. The model is meshed using 10-node quadratic tetrahedral elements (C3D10 in Abaqus). As shown in "Fig. 26(b)", the mesh is refined in the center of the beam, where the crack is expected to nucleate and grow. The characteristic element size is at least five times smaller than the phase field length scale, and the total number of elements is 18970. The results are computed using the monolithic scheme. The static analysis results indicate stress concentrations near the connections of the structure to the motor and the bases. Figure 26(a) shows the geometric model of the structure with

specified loading, while "Fig. 26(b)" displays the finite element mesh. Figure 26(c) illustrates the stress distribution results after the load is applied. The dynamic analyses also examine the structure's response to variable loads and show how the structure behaves under dynamic loading. These analyses indicate that the critical stress points and discontinuities are primarily located in the middle of the connections to the motor and between the bases [14-15].

3.4.2. Modal Analysis of Crack Growth in Structure

The following images show the modal shapes of different cracks obtained using XFEM. These images depict the crack paths and displacement discontinuities in each mode. Figure 27 displays both (a) the front and (b) rear views of cracks in various modes. Modal analysis helps identify the crack patterns and the behavior of different crack modes, illustrating how the cracks propagate within the structure.

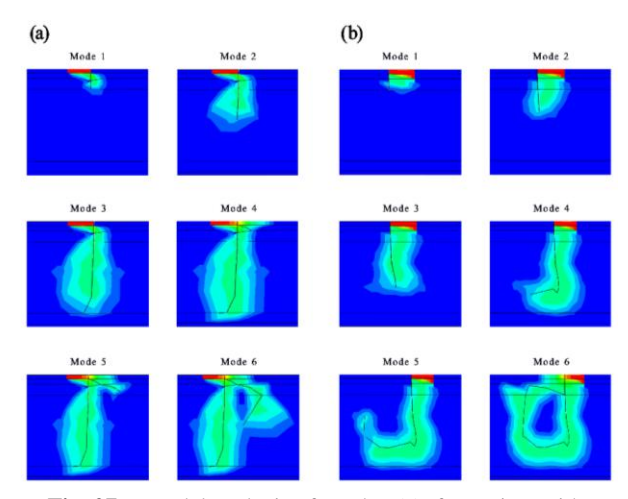


Fig. 27 Modal analysis of cracks: (a): front view with various crack modes, and (b): rear view with various crack modes.

3.4.3. Fatigue Life and Crack Growth Analysis in Structure

Figure 28 illustrates the fatigue life and crack growth analysis of the structure under dynamic loading.

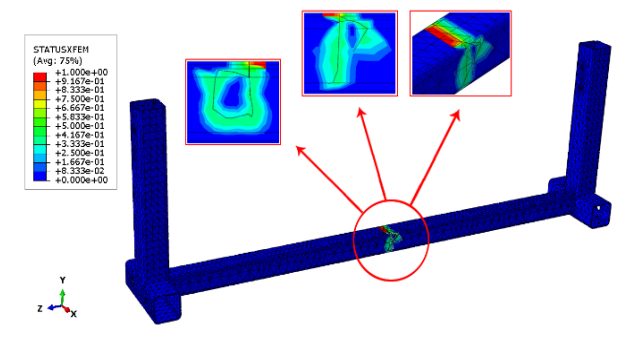


Fig. 28 Fatigue life and crack growth analysis of the structure under dynamic loading.

These analyses indicate that the critical crack points are located near the connections of the structure to the motor and the bases. By examining the gradual changes in the crack and the effects of cyclic loads, a better understanding of the structure's lifespan and weak points can be achieved. The highest stress occurs in the upper regions of the structure. Additionally, the lowest stress is observed in the middle and lower areas of the structure, indicating weakness and the application of excessive load in the upper regions of the structure. Fatigue and crack growth analysis help identify potential crack paths and critical areas, enabling necessary actions for design improvement, increased durability, and optimization. The numerical values indicate the crack status in the model elements. A value of 1.0 signifies a fully developed crack and the highest level of crack and discontinuity in the XFEM model within the structure. Conversely, a value of 0.0 indicates no crack and the lowest level of crack and discontinuity in the structure.

Fatigue analysis under cyclic loading, as shown in "Fig. 29", represents the variations in the applied force relative to the number of loading cycles.

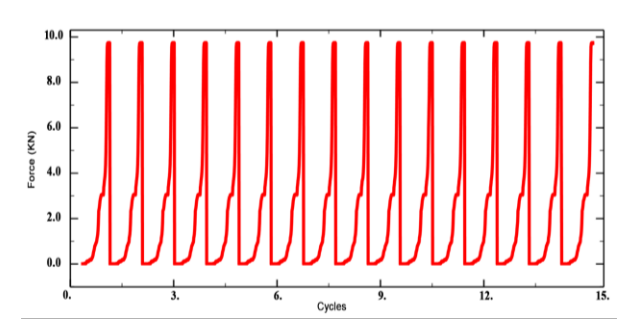


Fig. 29 The diagram of applied force variations concerning the number of loading cycles in the fatigue analysis of the diesel engine test support structure.

This diagram illustrates the dynamic behavior of the component under cyclic loading, where the applied force varies between 0 and 10 KN over 15 cycles. Each cycle represents a complete period of loading and unloading the force from the component. Therefore, this force-cycle diagram can accurately predict the component's useful life in the diesel engine test support structure. The results indicate stable cyclic loading behavior and its impact on the component's fatigue life. Analyzing the data, the component's fatigue life was predicted, and critical points that could lead to failure were identified.

3.4.4. Force-Displacement Relationship

Figure 30 shows the Force-Displacement diagram, illustrating the changes in applied force with crack displacement.

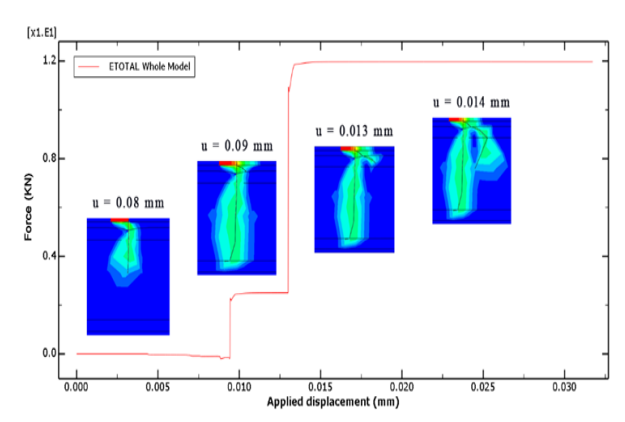


Fig. 30 Crack growth diagram in the three-point bending test: force response versus displacement.

As expected and consistent with the results obtained by reference [13], a crack nucleates at the bottom of the beam, at the center of the beam axis. The crack propagates directly upwards until it reaches the top, as shown in "Fig. 26(c)". The force response versus displacement closely agrees with the predictions of reference [13]. This diagram aids in a more detailed analysis of crack behavior and in predicting the structure's fatigue life. By analyzing the forcedisplacement diagram, it is possible to identify points where the crack rapidly proliferates and sudden changes in the structure's behavior occur. This information can be used to design a more robust structure and optimize maintenance and repair processes. The highest displacement and crack growth, corresponding to the late stages of crack propagation, is 0.014 mm with a force of 12 KN in the structure. Additionally, the lowest displacement and crack growth, corresponding to the early stages of crack initiation, is 0.08 mm with a force of 2 KN in the structure. These results indicate stability and weakness in the structure, respectively.

3.4.5. Buckling Mode Analysis and Critical Load Calculation in the Structure

In this section, the buckling mode analysis for the diesel engine test support structure was conducted, and the critical loads for each mode were calculated. This analysis was performed using Abaqus software, which selected the subspace solver for its high efficiency and accuracy in analyzing linear buckling problems. This solver facilitates the accurate determination of eigenvalues and critical buckling modes, which are crucial for assessing the stability of structures under compressive loads.

The buckling mode shapes for various modes are presented in "Table 6", illustrating the distribution of stresses and critical areas in each buckling mode. Eigenvalues for ten different buckling modes were obtained, representing the factors by which the initial load must be multiplied to determine the critical

buckling load for each mode. This analysis applied an initial load of 613 N (for one engine mount) as a concentrated force at specific structure points. Subsequently, the critical buckling load for each mode was calculated using these eigenvalues. The critical buckling load is the load at which the structure becomes unstable under compressive forces, typically considered a key indicator in structural design to prevent sudden failure [17].

Table 6 Buckling Mode Shapes of the Engine Mount in the Diesel Engine Test Support Structure

1st Mode	2 nd Mode	3 rd Mode	4 th Mode	5 th Mode
		10.000		1000 m · 0
6 th Mode	7 th Mode	8th Mode	9th Mode	10 th Mode
	Shirt on Such City	Designation		D.S. C.

The computational results are presented in "Table 7", showing the critical buckling loads versus mode numbers. The results indicate that the critical buckling load varies significantly across different modes, highlighting the need for more precise structural design to prevent buckling under critical conditions.

Table 7 Eigenvalues and Calculated Critical Buckling Loads for the First 10 Buckling Modes

THE STATE OF BUILDING PROCESS						
Mode No.	Eigenvalue	Critical Load (KN)				
First	740.35	453.94				
Second	804.32	493.05				
Third	835.09	511.41				
Fourth	898.73	550.96				
Fifth	934.02	572.52				
Sixth	981.22	601.79				
Seventh	1062.2	651.11				
Eighth	1074.9	658.91				
Ninth	1022.6	627.84				
Tenth	1056.0	647.93				
·	·	· · · · · · · · · · · · · · · · · · ·				

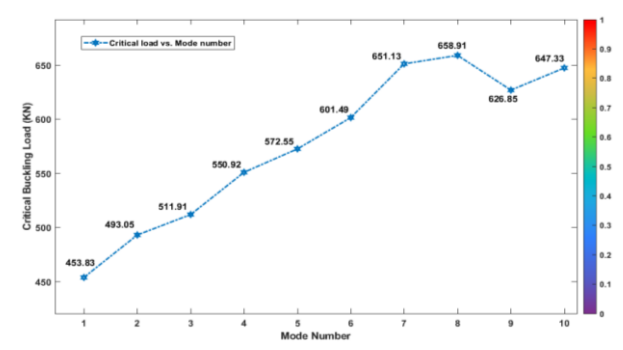


Fig. 31 Graph of the Variation of Critical Buckling Load concerning Mode Number.

Figure 31 graphically displays the variation of essential buckling loads with respect to the mode numbers. The first and second modes, with eigenvalues of 740.35 and 804.32, respectively, are particularly significant due to their greater impact on the structure's overall stability. Therefore, these modes should be a primary consideration in the final design decision-making process.

Ultimately, this analysis demonstrates that the critical buckling load for all modes is significantly higher than the initial load applied to the structure, indicating that the structure is safe against the current loads. However, to enhance safety margins and ensure the structure's stability under unexpected or critical conditions, it is recommended that higher safety factors be incorporated into the final design. Specifically, it is suggested that the critical buckling load be considered 1.5 to 2 times the calculated value. Additionally, reviewing and reinforcing the sensitive and vital areas of the structure can prevent buckling under critical conditions and ensure overall structural safety.

3.4.6. Stress Distribution and Safety Assessment of the Axial Arm under Three-Point Bending

This section examines the Von Mises stress distribution in the axial arm supporting the engine mounts under three-point bending loading. Figure 32 illustrates the Von Mises stress distribution in the axial arm.

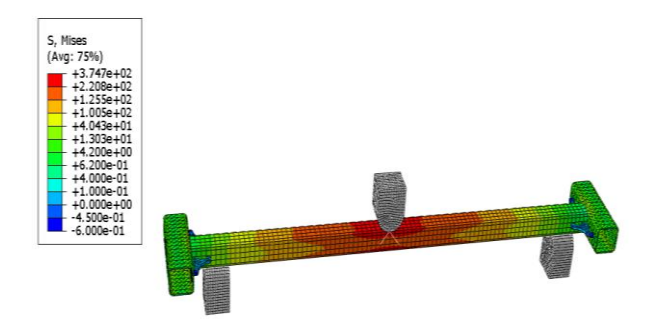


Fig. 32 Von Mises stress distribution in the axial arm supporting the engine mounts under a three-point bending load.

The maximum Von Mises stress, recorded at 374.7 MPa, is located in the central region of the beam, directly beneath the point of concentrated load application. This area experiences the highest bending stress due to its position at the peak of the bending moment. Conversely, the minimum Von Mises stress, which is 13 MPa, is observed in regions farther from the center of the beam and closer to the supports.

Considering the three-point bending test and similar loading conditions for the engine mounts installed on this axial arm, the analysis results indicate that the beam possesses sufficient safety margins. Compared to the material's yield stress and operational conditions, the maximum stress within the structure remains within a range that ensures the structure's resistance to the applied loads, thus preventing failure or yielding under normal operating conditions [18]. This assessment demonstrates that, although the center of the beam bears the highest stress, the overall structure effectively withstands the applied loads. The design and safety evaluation confirm the beam's ability to withstand both dynamic and static loads. Therefore, it can be concluded that the beam used for installing the engine mounts is safe under normal operating conditions.

4 CONCLUSIONS

In this study, a comprehensive analysis of the Static, Modal vibration, Safety factor, Fatigue life, and Modal crack growth characteristics of the diesel engine test support structure (ETSS) was conducted using Finite Element Method (FEM) and Extended Finite Element Method (XFEM). The primary objective of this research was to evaluate the structure's performance, identify critical stress and vibration points, and predict fatigue life to enhance safety, reinforce, and optimize the support structure.

The findings can be summarized as follows:

- The static analysis revealed that the maximum von Mises stress ranged between 275 and 617 MPa in the telescopic supports of the engine handle and the longitudinal and transverse frames. The minimum stress values were observed in the radiator holders, fuel tank, and control panel. The stress path analysis also indicated that critical stress points are concentrated in the moving parts and base supports, which require reinforcement.
- The displacement and stress path analysis further revealed that the maximum displacements ranged between 1.204 and 1.685 mm in the radiator holders. In contrast, the most minor displacements occurred in the battery holders and control panel, ranging from 0.2408 to 0.9630 mm. These findings underscore the need to reinforce areas subjected to large loads.

- The shear stress analysis in different directions (XY, XZ, YZ) indicated that the highest stress occurred in the telescopic areas, radiator plates, and parts of the fuel tank and battery holders. These areas require special attention in design and reinforcement.
- The analysis of lateral vibrations caused by the engine's dynamics revealed that these vibrations are transmitted to the structure's components and vary for each structural member depending on displacement and time. Modal analysis showed that the maximum displacement observed was 0.08135 mm at a frequency of 7.20 Hz. These vibrations could lead to damage over time, necessitating proper management and control.
- The fatigue and crack growth analysis using XFEM results indicated that the maximum crack growth was 0.014 mm under a force of 12 KN, predominantly in critical areas such as motor connections and base supports. These findings highlight the need for monitoring and reinforcing vulnerable areas to prevent fatigue-induced failures.
- The safety factor analysis revealed that while most structural parts have sufficient safety margins, the central longitudinal and transverse support frames require reinforcement. It is recommended to use a safety factor between 1.5 and 3 for high-stress areas to ensure the overall structural safety.
- The buckling analysis results for the engine mount structure showed that the structure is safe under the current applied loads, as the critical buckling loads are significantly higher than the initial load of 613 N. The first and second modes, with eigenvalues of 740.35 and 804.32, have a more significant impact on the stability of the structure and should be prioritized in the final design. To enhance safety and ensure the structure's strength under critical conditions, it is recommended to incorporate a safety factor of 1.5 to 2 times in the final design and reinforce sensitive areas.
- The results of the three-point bending test on the axial arm supporting the engine mounts showed that the maximum Von Mises stress, measured at 374.7 MPa, is located in the central region of the beam, directly beneath the point of concentrated load application. However, the minimum Von Mises stress, recorded at 13 MPa, was observed in areas farther from the center of the beam and closer to the supports. This analysis demonstrated that the axial arm has sufficient safety margins and is resistant to the applied loads, particularly under normal operating conditions. Therefore, the design and safety evaluation confirm that this arm can withstand dynamic and static loads and is adequately safe.

Future research could build upon the present findings by conducting experimental validation through fullscale prototype testing and sensor-based data acquisition. Moreover, investigating the structural performance under multi-axial and time-dependent loading conditions—such as thermal fluctuations, impact, and cyclic fatigue—may yield deeper insights into long-term durability. Exploring material optimization techniques and implementing multi-objective design strategies could further enhance structural efficiency, resilience, and cost-effectiveness.

REFERENCES

- Koch, L., Zeller, P., Test Stand for Dynamic Investigations of Combustion Engines, Automobiltech. Z., (Germany, Federal Republic of) Vol. 89, No. 11, 1987.
- [2] Von Thun, H. J., A New Dynamic Combustion Engine Test Stand with Real-Time Simulation of The Vehicle Drive Line, SAE Transactions, Jan 1, 1987, pp. 385-91.
- [3] Voigt, K. U., A Control Scheme for A Dynamical Combustion Engine Test Stand, InInternational Conference on Control 1991, Control 91, IET, Vol. 25, 1991, pp. 938-943.
- [4] Temple, G., Jize, N., and Wysocki, P., Testability Modeling and Analysis of a Rocket Engine Test Stand, In 2005 IEEE Aerospace Conference, 2005, pp. 3874-3895.
- [5] Oldenkamp, A., Omid, B., Skene-Hamilton, C., and Egilson, K., Design of an Engine Test Stand: Design Report, 2012.
- [6] Tatarynow, D., Longwic, R., Sander, P., Zieliński, Ł., Trojgo, M., Lotko, W., and Lonkwic, P., Test Stand for a Motor Vehicle Powered by Different Fuels. Applied Sciences, Vol. 12, No. 20, 2022, pp. 10683.
- [7] Magryta, P., Pietrykowski, K., and Borowiec, P., FEM Simulation of Different Engine Mount Models in an Aircraft Piston Diesel Engine. Advances in Science and Technology, Research Journal, Vol. 16, No. 5, 2022.
- [8] Gholami, N., Afsari, A., Nazemosadat, S. M., and Afsari, M. J., Simulation and Dynamic-Thermal Analysis of Ceramic Disc and Brake Pad for Optimization by Finite Element Method, International Journal of Advanced Design & Manufacturing Technology, Vol. 16, No. 4, 2023.
- [9] Nazemosadat, S. M., Ghanbarian, D., Naderi-Boldaji, M., and Nematollahi, M. A., Structural Analysis of a Mounted Moldboard Plow Using the Finite Element Simulation Method, Spanish Journal of Agricultural Research, Vol. 20, No. 2, 2022, pp. e0204-, https://doi.org/10.5424/sjar/2022202-18157.
- [10] Reynders, E., System Identification Methods for (Operational) Modal Analysis: Review and

- Comparison, Archives of Computational Methods in Engineering, Vol. 19, 2012, pp. 51-124.
- [11] Khennane, A., Introduction to Finite Element Analysis Using MATLAB® and abaqus, CRC Press, 2013.
- [12] Rege, K., Lemu, H. G., A Review of Fatigue Crack Propagation Modelling Techniques Using FEM and XFEM, InIOP Conference Series: Materials Science and Engineering, IOP Publishing, Vol. 276, No. 1, 2017. pp. 012027.
- [13] Wells, G. N., Sluys, L., A New Method for Modelling Cohesive Cracks Using Finite Elements, International Journal for Numerical Methods in Engineering, Vol. 50, No. 12, 2001, pp. 2667-82.
- [14] Wu, J. Y., A Unified Phase-Field Theory for The Mechanics of Damage and Quasi-Brittle Failure, Journal of the Mechanics and Physics of Solids, Vol. 103, 2017, pp. 72-99.
- [15] Wu, J. Y., Nguyen, V. P., A Length Scale Insensitive Phase-Field Damage Model for Brittle Fracture, Journal of the Mechanics and Physics of Solids, Vol. 119, 2018, pp. 20-42.
- [16] Burr, A., Cheatham, J., Mechanical Design and Analysis, 2nd ed, Section 5.2. Prentice-Hall, Vol. 201, 1995, pp. 90-122.
- [17] Taheri-Behrooz, F., Omidi, M., Buckling of Axially Compressed Composite Cylinders with Geometric Imperfections, Steel and Composite Structures, Vol. 29, No. 4, 2018, pp. 557-67.
- [18] Scutaru, M. L., Itu, C., Marin, M., and Grif, H. Ş., Bending Tests Are Used to Determine the Mechanical Properties of The Components of a Composite Sandwich Used in Civil Engineering, Procedia Manufacturing, Vol. 32, 2019, pp. 259-67.
- [19] Mohammadi, M., Nazemosadat, S. M. R., and Afsari, A., Modeling and Analysis of a Tractor Diesel Engine Test Stand Structure Using the Finite Element Method, Biomechanism and Bioenergy Research, Vol. 3, No. 2, 2024, pp. 75-87.
- [20] Zarei, Y., Afsari, A., Nazemosadat, S. M., and Mohammadi, M., Simulation and Thermo-Mechanical Analysis of AA6063-T5 in FSW by FEM, Journal of Modern Processes in Manufacturing and Production, Vol. 2, 2024, pp. 5.
- [21] Mohammadi, M., Nazemosadat, S. M., Fazel, D., and Lari, Y. B., An Integrated Approach for Structural Modeling, Modal Analysis, And Aerodynamic Evaluation of an Electric Vehicle Body Shell Using Finite Element Method and Computational Fluid Dynamics, Materials Today Communications, Vol. 45, 2025, pp. 112331.

DOI: ISSN: 2252-0406 https://admt.isfahan.iau.ir

Experimental Study of Magnetic Field-Aided Friction Stir Spot Welding

Farshad Akbari, Seyed Mohammad Hossein Seyedkashi *

Department of Mechanical Engineering,

University of Birjand, Iran

E-mail: Farshad2773@gmail.com, seyedkashi@birjand.ac.ir

*Corresponding author

Moosa Sajed

Department of Mechanical Engineering, Azarbaijan Shahid Madani University, Iran E-mail: sajed@azaruniv.ac.ir

Received: 23 May 2025, Revised: 15 July 2025, Accepted: 1 October 2025

Abstract: Magnetic field is applied during the friction stir spot welding of St37 steel to achieve a better microstructure and mechanical properties. The process is called magnetic field-aided friction stir spot welding. The magnetic field is applied using an induction heater module and coil in which the welding tool acts as the core for the coil. The effects of tool rotational speed, voltage, and dwell time on the strength and microstructure of welded samples are investigated. The strength of joints increased using a magnetic field, and the effect is stronger when a lower tool rotational speed and dwell time are used. This could be attributed to the heat input by applying the Eddy current in the nugget together with a finer microstructure, which is achieved by applying the magnetic field. The increase of all three parameters simultaneously overheats the nugget and results in a drop in the strength of the joint. The highest strength of 5159.5 N is achieved with a tool rotational speed, a dwell time, and a voltage of 2000 rpm, 6 s, and 25 V, respectively.

Keywords: Friction Stir Spot Welding, Magnetic Field, Magnetic Field Aided Friction Stir Spot Welding, Mechanical Properties,

Biographical notes: Farshad Akbari received his BSc and MSc in Manufacturing Engineering from the Technical and Vocational University in 2016 and the University of Birjand in 2021, respectively. His research interest is friction stir welding process. Seyed Mohammad Hossein Seyedkashi received his PhD degree (Manufacturing Engineering) from Tarbiat Modares University in 2012. He is currently a professor in the Department of Mechanical Engineering, University of Birjand, Birjand, Iran. His research interests are sheet metal forming, friction stir welding, additive manufacturing and optimization. Moosa Sajed is an Assistant Professor at Azarbaijan Shahid Madani University. He received his PhD in Manufacturing Engineering from the University of Birjand in 2021. His research interests include solid-state processing, mechanical alloying, and finite element analysis.

Research paper

COPYRIGHTS

© 2025 by the authors. Licensee Islamic Azad University Isfahan Branch. This article is an open access article distributed under the terms and conditions of the Creative Commons Attribution 4.0 International (CC BY 4.0) (https://creativecommons.org/licenses/by/4.0/)



1 INTRODUCTION

Friction Stir Welding (FSW) was invented in 1991 by The Welding Institute (TWI) [1]. It is a solid-state and environmentally friendly welding process that can be used to join high-strength aluminum alloys and those that cannot be welded by conventional welding processes. In the process, a non-consumable rotary tool that contains a pin and shoulder penetrates the interface of two plates to be welded [2]. The tool has two main roles: heat production and material movement. The produced frictional heat makes the material soft enough that it is then stirred by a rotary pin [3]. Tool feed rate, tool rotational speed, and axial load are the main process parameters [4]. The tool pin profile is also an important parameter. The main pin profiles are square, triangle, threaded, and simple cylinder [5].

Friction stir spot welding is a variant of the main process, where there is no transverse movement of the tool, and joining occurs in a small zone. Research has been performed to increase the strength of the joint. For example, Venukumar et al. [6] investigated the strength and fatigue behavior of refilled friction stir spot welded 6061 aluminum sheets. They used a tool with a retractable pin to join and refill the spot weld. They reported an increase in the strength of the joint by refilling, but no change in the fatigue behaviour of the joints. Sajed [7] introduced two-stage refilled friction stir spot welding to refill the keyhole simply. He mentioned the pinless tool shoulder diameter as the most effective parameter on the weld strength. The exact process was used by Akbari et al. [8] to join polyethylene sheets. They reported higher strength at a lower tool rotational speed.

The application of a magnetic field in the welding zone is a common technique used to increase joint strength and achieve a fine microstructure. Mou et al. [9] reported that electric and magnetic fields can improve the joint microstructure in cold metal transfer. The Lorentz force makes the arc move in a circular path. It also shortens the arc length and widens its width. They reported an increase in the joint strength from 270.7 to 387.8 MPa as a result of using a magnetic field. Liu et al. [10] applied a magnetic field during the welding of copper sheets. They reported that the thickness of the Al2Cu inter-metallic decreased from 50 to 5 µm as a result of the application of the magnetic field. They also reported an increase in the strength of the joint. Sun et al. [11] reported magnetic field-aided CMT welding of Al6061-T6 and TC4 alloys. They concluded that the magnetic field increases the transmission ability of the fusion pool. Cao et al. [12] investigated the effect of the magnetic field on the welding nugget in laser welding of aluminum alloys. They reported that the Lorentz force is applied by the magnetic field in the opposite direction of the fusion pool, which restricts the

width of grains. Chen et al. [13] investigated the magnetic field-assisted welding of steel. According to the results, the ultimate strength was increased by 43.9% and the grains were finer by a factor of 2.

In the present paper, a magnetic field is applied during the friction stir spot welding of St37 steel sheets and its effect is investigated on the strength and microstructure of the joints. A setup was designed to apply the magnetic field to the welding zone, including a transformer, induction heater module, cooling system, and a coil. The welding tool acts as a core for the coil during the welding, and an Eddy current is induced that heats the nugget. However, the presence of the magnetic field restricts the grain growth, and a finer microstructure could be achieved so that the heat is induced on the nugget with no grain growth.

The main innovation of the present paper is applying a magnetic field concurrently with friction stir spot welding of low-carbon steel sheets. Friction stir welding is successfully applied to a wide range of engineering materials, from polymers to alloys. When welding high strength alloys is the case, using auxiliary energies is a standard method. Electrical current is a widely adopted heating source that is used in this case. However, what is considered in this paper is applying a magnetic field during the welding process, which was not carried out before, to the best of the authors' knowledge. This field prevents grains from growing considerably, which makes the joints stronger.

2 MATERIAL AND METHODS

St37 steel sheets with dimensions of $1\times50\times160$ mm3 were used to carry out the experiments. The chemical composition of St37 alloy is presented in "Table 1".

Table 1 The chemical composition of St37 steel [14]

С	Si	Mn	P	S	Cr	Ni	Fe
0.11	0.03	0.56	0.007	0.005	0.07	0.03	Bal.

In this process, frequency is applied using an induction heater module driven by a transformer with a current of 20 A. The induction heater is an electric device that produces heat by inducing a magnetic field. A wire with a diameter of 2 mm was used to fabricate a coil with 9 loops and an internal diameter of 30 mm. The coil that is connected to the induction heater is used to transfer the produced frequency. Figure 1 presents the induction heater module, its fixture, the cooling system, and the coil.

The produced magnetic field is transmitted to the coil, which creates a current that varies with time according to Faraday's Law, known as the Eddy current. The

Eddy currents flow through the workpiece in closed circles. The direction of the currents is orthogonal to the magnetic field. The amount of the Eddy current is directly dependent on the magnetic field, area of the ring, and magnetic flux variation, while it varies inversely with any variations in the conduction of the wire. Figure 2 presents the Eddy current in the workpiece.

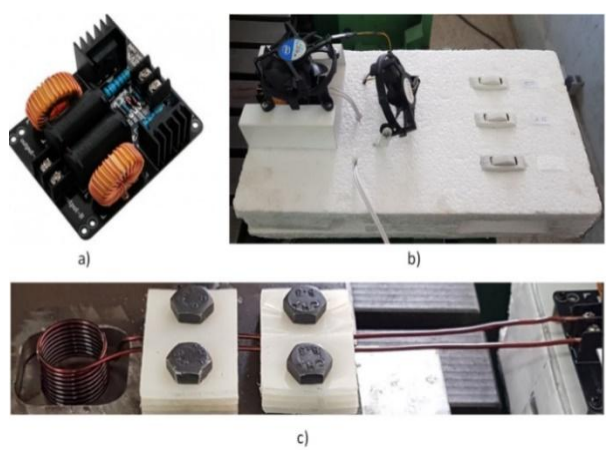


Fig. 1 (a): The induction heater module, (b): the fixture of the induction heater and cooling system, and (c): the coil.

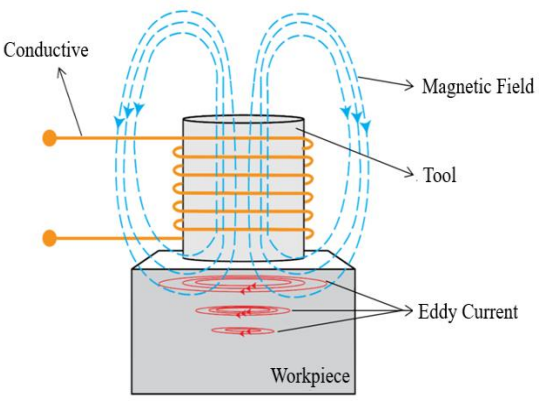
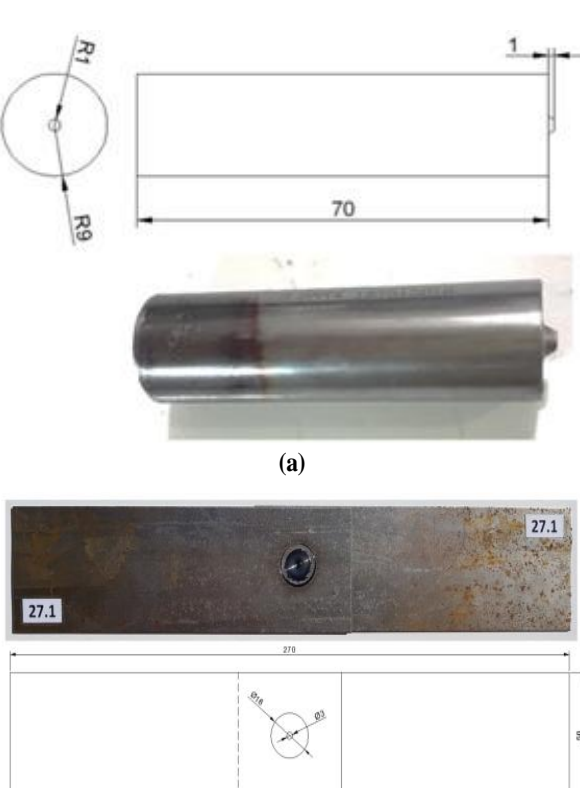


Fig. 2 Eddy current in the workpiece.

The experiments were carried out using a universal CNC FP4M milling machine. The tool material was WC. Figure 3 presents the tool and a typical welded sample, along with their dimensions. The experiment setup is also illustrated in "Fig. 4". The tool rotational speed, dwell time, and voltage were investigated as key parameters. Three levels were considered for all parameters. The full factorial design of experiments was considered, and 27 test sets were obtained. The levels of investigated parameters are summarized in "Table 2".

To evaluate the effects of input parameters on the strength and microstructure of the joints, the tensileshear test was carried out, and the microstructure of the joints was evaluated using an optical microscope. The results of the tensile-shear test, together with process parameters corresponding to each experiment, are given in "Table 3".



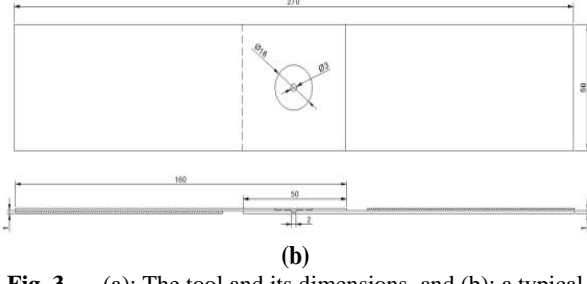


Fig. 3 (a): The tool and its dimensions, and (b): a typical welded sample and its dimensions.

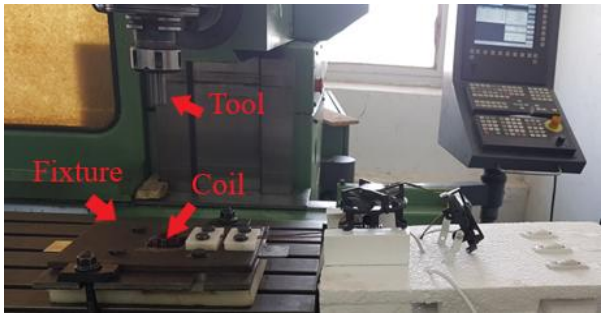


Fig. 4 The experiment setup.

Table 2 The investigated parameters and their levels

Levels	Rotational Speed (rpm)	Dwell Time (s)	Voltage (V)
1	1000	3	0
2	1500	6	18
3	2000	9	25

Table 3 The parameters of experiments and results of the tensile-shear test

tensile-snear test					
No.	Tool Rotational Speed (rpm)	Dwell Time (s)	Voltage (V)	Tensile- Shear Strength (N)	
1	1000	3	0	405.6	
2	2000	3	18	2576.6	
3	1000	9	18	2775.2	
4	1500	6	25	4055.1	
5	2000	6	18	4860.2	
6	2000	6	25	5159.5	
7	1500	9	18	4116.4	
8	1500	3	0	849.2	
9	1000	9	25	3181.6	
10	1000	3	18	1248.8	
11	2000	6	0	4666.5	
12	2000	9	0	4352.5	
13	1000	6	18	1550.2	
14	2000	3	0	1168.4	
15	1500	3	25	2353.2	
16	1000	6	0	1501.7	
17	1000	6	25	2191.9	
18	2000	9	18	3829.8	
19	1500	6	0	1843.1	
20	1000	9	0	2897.3	
21	1500	9	0	3276.7	
22	1000	3	25	1234.8	
23	2000	3	25	3525.0	
24	1500	6	18	3470.2	
25	1500	3	18	1933.8	
26	1500	9	25	3513.7	
27	2000	9	25	3562.2	

3 RESULTS AND DISCUSSION

Generally, the heat generation and propagation pattern, as well as the temperature level, are key factors that determine the joint quality in friction-based processes [15]. When steel is welded using friction stir welding, it is essential to provide enough heat input in the welding nugget to achieve a sound weld. Thus, using auxiliary heat sources could be helpful. In this research, a magnetic field was applied during the welding to study the effect of Eddy current on the strength and microstructure of spot joints in St37 sheets. Tool rotational speed and dwell time as the main sources of heat input in welding were also investigated.

"Table 4" presents the results of the analysis of variance for the strength of joints. According to the results, dwell time, with a contribution percentage of 38.08%, is the most effective input parameter, followed by tool rotational speed and voltage, with contribution percentages of 34.41% and 7.89%, respectively. When 2-way interactions are considered, the interaction of tool rotational speed and dwell time has the maximum contribution on the joint strength, with a contribution

percentage of 9.08% followed by the voltage and dwell time interaction and the interaction of voltage and tool rotational speed, with contribution percentages of 5.08% and 1.89%, respectively. The main effects plot is presented in "Fig. 5". The strength increases by increasing all three investigated parameters. However, it is sharper in the case of dwell time. Any increases in any of the investigated parameters increase the amount of heat input in the welding nugget, which can be considered a reason for the same trends observed in the main plots.

Table 4 Analysis of Variance for the strength of joints

Table 4 Tillary 313 Of		variance for th	ie strength or j	Omico
Source	DF	Seq SS	Contribute	P- Value
Model	18	43485158	96.41%	0.001
Linear	6	36252665	80.38%	0.000
Voltage	2	3558754	7.89%	0.010
Rotational Speed	2	15519115	34.41%	0.000
Dwell Time	2	17174796	38.08%	0.000
2-Way Interactions	12	7232493	16.04%	0.065
Voltage×Rotatio nal Speed	4	850199	1.89%	0.439
Voltage×Dwell Time	4	2289072	5.08%	0.098
Rotational Speed×Dwell T	4	4093222	9.08%	0.025
Error	8	1617571	3.59%	
Total	26	45102729	100.00%	

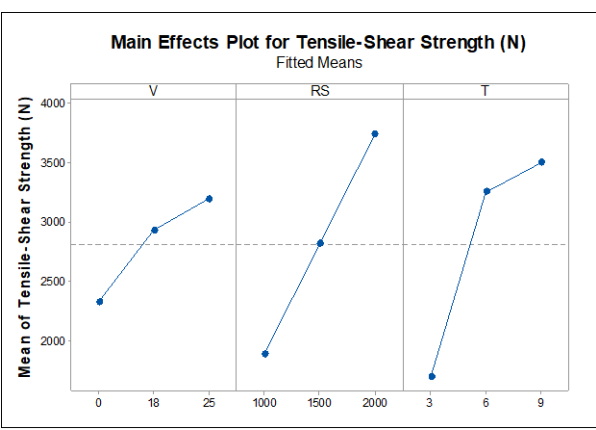


Fig. 5 The main effects plot (V=voltage, RS=tool rotational speed, and T=dwell time).

Increasing the dwell time from 3 to 6 s, makes a significant increase in the strength of the joint, while further growing dwell time from 6 to 9 s does not considerably affect the strength. This indicates that when the dwell time is less than 6 seconds, there is insufficient time for the material to be mixed properly. Also, further increase in the time is not necessary when the welding sheets are low carbon steels. However, for tool rotational speed, any increase from 1000 to 2000 rpm increases the joint strength considerably. The plot indicates that using tool rotational speeds more than 2000 rpm, may result in even stronger joints. This should be investigated in future studies. The effect of increasing the voltage is just like increasing the tool rotational speed. However, it is less effective on joint strength when compared to the tool rotational speed. The interaction plots are also presented in "Fig. 6".

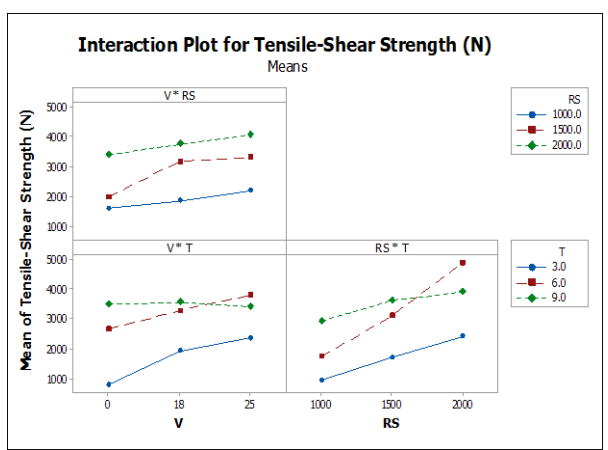


Fig. 6 The interaction plots (V=voltage, RS=tool rotational speed, and T=dwell time).

According to "Fig. 6", the interaction of tool rotational speed and voltage can be ignored due to the semiparallel plot of that. On the other hand, when the voltage is at its highest level, i.e. 25V, increasing dwell time from 6 to 9s results in a drop in strength of the joint, which can be attributed to the overheating of the nugget and the resulting grain growth [16]. The same effect is detectable when the tool rotational speed is at its fastest level, i.e. 2000 rpm, and dwell time increases from 6 to 9s. Thus, it could be concluded that although a higher dwell time is needed when steel is welded, overall heat input to the welding nugget should be considered, and an optimal set of parameters should be applied based on it.

According to the results, welding parameters, including tool rotational speed and dwell time, are much more significant on the strength of joints in comparison to the voltage in both main and interactive effects. However, according to "Table 3", when the tool rotational speed is at its lowest level, i.e. 1000 rpm, a comparison between the strength of welded samples

presents a significant effect of the application of the magnetic field. The strength is just 405.6 N for sample 1 which was welded with a tool rotational speed of 1000 rpm, dwell time of 3s, and no voltage, while it is 1248.8 and 1234.8 N for samples 10 and 22, respectively, which were welded with the same rotational speed and dwell time but with a voltage of 18 and 25 V, respectively. This indicates that the strength of the joint was almost tripled when the magnetic field was applied. Thus, it could be concluded that heat input is a key factor when steel sheets are spot-welded, and the main sources of heat input are tool rotational speed and dwell time. However, when a lower tool rotational speed is needed, a magnetic field could be introduced to the nugget to increase the joint strength. On the other hand, the main disadvantage of the friction stir spot welding in comparison with resistance welding, when it is applied on steel, is the time of the process. Using a magnetic field during the friction stir spot welding, one can reduce the dwell time without a significant drop in strength to make the process more favorable and faster. Four distinct areas presented in "Fig. 7" could be determined in the microstructure of friction stir spot welded joints; stir zone (SZ), thermo-mechanically affected zone (TMAZ), heat affected zone (HAZ), and base metal (BM) [17].

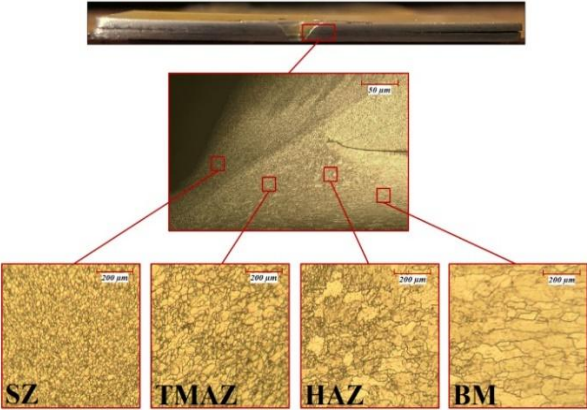


Fig. 7 Microstructural zones with a tool rotational speed of 2000 rpm, dwell time of 9s, and voltage of 25V.

In samples welded at a lower tool rotational speed and dwell time, it is evident that there was no proper stirring during the welding process, which could be attributed to the lower heat input. In these samples, improper joints, cracks, and porosity were detected in the microstructure of the joint. Better stirring is evident when a longer dwell time is used, providing more time for stirring together with a higher heat input. The tool's rotational speed can be considered the main parameter affecting heat generation during welding. Generally, any increase in the tool rotational speed results in a higher strain rate and more plastic deformation [18]. Any increase in the tool rotational speed also widens

the microstructural zones, which is evident in "Fig. 8" where defects are pointed by arrows.

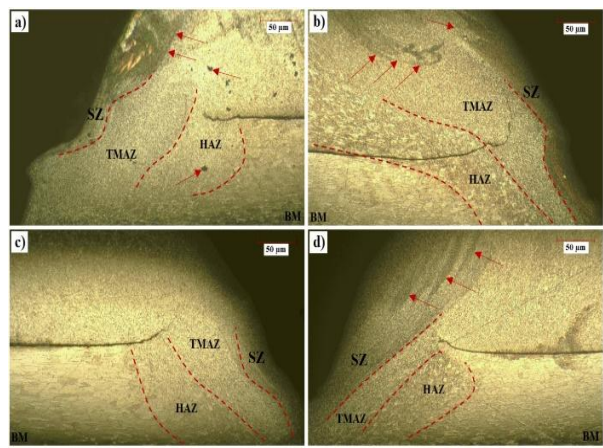


Fig. 8 Microstructural zones in the samples without the magnetic field and with tool rotational speed and dwell time of: (a): 1000 rpm and 3s, (b): 1000 rpm and 9s, (c): 2000 rpm and 3s, and (d): 2000 rpm and 9s. Arrows point to the defects.

In the TMAZ, there is not enough driving force for dynamic recrystallization because the strain rate and temperature are lower compared to the stir zone [19]. According to "Fig. 8", there are coarse grains together with defects in this zone when a lower tool rotational speed is used. An increase in the tool rotational speed results in a fine microstructure, and also the defects vanish.

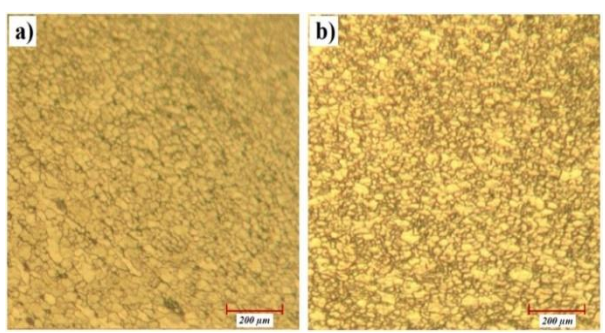


Fig. 9 Stir zone of the sample welded with a tool rotational speed, dwell time, and voltage of: (a): 1500 rpm, 6s, 0V, and (b): 1500 rpm, 6s, and 25 V.

In the case of higher heat input, two failure mechanisms are detectable, including the formation of intermetallic compounds (mostly in welding of dissimilar alloys) and the onset of defects [20]. In this study, any increase in parameters results in higher heat input in the welding nugget. Thus, the joint strength does not have its highest value when the highest levels of all parameters are used (see "Table 3"). Application of a magnetic field results in fine grains when a lower tool rotational speed and dwell time are used (see "Fig. 9") and also a bigger stir zone. However, more defects

are present when these parameters are at their highest level, leading to a lower joint strength.

4 CONCLUSIONS

In this paper, magnetic field-aided friction stir spot welding of St37 steel was conducted. Three input parameters, including tool rotational speed, dwell time, and voltage, were investigated. The strength of joints was evaluated, and the microstructure of welding nuggets was also investigated. The main results are as follows:

- Any increase in the tool rotational speed, dwell time, and voltage results in an increase in the strength of the joint due to more heat input.
- The stirring is not enough when a lower tool rotational and dwell time are used, and proper joining does not take place in this case.
- Application of a magnetic field results in a bigger stir zone and finer microstructure, and then stronger joints. This effect is stronger when a lower tool rotational speed and dwell time are used.
- The welding nugget is overheated when all parameters are in their highest levels, which results in defect formation, a coarse microstructure, and hence a reduction in the joint strength.
- The best strength was 5159.5 N, which was achieved by sample 6, which was welded with a tool rotational speed, dwell time, and voltage of 2000 rpm, 6s, and 25V, respectively.

REFERENCES

- Thomas, W. M., Nicholas, E. D., Needham, J. C., and et al., Friction Welding, USA Patent No. US5460317A, 1995.
- [2] Sattari, S., Bisadi, H., and Sajed, M., Mechanical Properties and Temperature Distributions of Thin Friction Stir Welded Sheets of AA5083, International Journal of Mechanics and Applications, Vol. 2, No. 1, 2012, pp. 1-6.
- [3] Sajed, M., Bisadi, H., Experimental Failure Study of Friction Stir Spot Welded Similar and Dissimilar Aluminum Alloys, Welding in the World, Vol. 60, No. 1, 2016, pp. 33-40.
- [4] Paidar, M., Khodabandeh, A., Lali Sarab, M., and et al., Effect of Welding Parameters (Plunge Depths of Shoulder, Pin Geometry, and Tool Rotational Speed) on the Failure Mode and Stir Zone Characteristics of Friction Stir Spot Welded Aluminum 2024-T3 Sheets, Journal of Mechanical Science and Technology, Vol. 29, 2015, pp. 4639-4644.
- [5] Atak, A., Impact of Pinless Stirring Tools with Different Shoulder Profile Designs on Friction Stir Spot Welded

- Joints, Journal of Mechanical Science and Technology, Vol. 34, 2020, pp. 3735-3743.
- [6] Venukumar, S., Yalagi, S., and Muthukumaran, S., Comparison of Microstructure and Mechanical Properties of Conventional and Refilled Friction Stir Spot Welds in AA 6061-T6 Using Filler Plate. Transactions of Nonferrous Metals Society of China, Vol. 23, No. 10, 2013, pp. 2833-2842.
- [7] Sajed, M., Parametric Study of Two-Stage Refilled Friction Stir Spot Welding, Journal of Manufacturing Processes, Vol. 24, 2016, pp. 307-317.
- [8] Akbari, F., Sajed, M., Ashrafi, A., and Seyedkashi, S. M. H., Influence of Welding Parameters on Strength of Friction Stir Spot Welded Polyethylene Sheets Using Two-Stage Refilling Process, Proceedings of the 4th International Conference on Manufacturing Engineering, 2018.
- [9] Mou, G., Hua, X., Wang, M., and et al., Effect of Axial Magnetic Field on Cold Metal Transfer Arc-Brazing of Ti6Al4V to 304L Steel. Journal of Materials Processing Technology, Vol. 275, 2020, pp. 116322.
- [10] Liu, Y., Sun, Q., Wang, H., and et al., Effect of the Axial External Magnetic Field on Copper/Aluminium Arc Weld Joining, Science and Technology of Welding and Joining, Vol. 21, No. 6, 2016, pp. 460-465.
- [11] Sun, Q., Li, J., Liu, Y., and et al., Arc Characteristics and Droplet Transfer Process in CMT Welding with a Magnetic Field, Journal of Manufacturing Processes, Vol. 32, 2018, pp. 48-56.
- [12] Cao, L., Zhou, Q., Liu, H., and et al., Mechanism Investigation of the Influence of the Magnetic Field on the Molten Pool Behavior During Laser Welding of Aluminum Alloy, International Journal of Heat and Mass Transfer, Vol. 162, 2020, pp. 120390.
- [13] Chen, R., Kong, H., Luan, J., and et al., Effect of External Applied Magnetic Field on Microstructures and

- Mechanical Properties of Laser Welding Joint of Medium-Mn Nanostructured Steel, Materials Science and Engineering: A., Vol. 792, 2020, pp. 139787.
- [14] Sajed, M., Seyedkashi, S. M. H., Solid-State Local Micro-Alloying of Thick St37 Steel Plates with SiC Powder Using a Modified Friction Hydro-Pillar Process, Journal of Materials Research and Technology, Vol. 9, No. 4, 2020, pp. 7158-7171.
- [15] Sajed, M., Seyedkashi, S. M. H., Multilayer Friction Stir Plug Welding: a Novel Solid-State Method to Repair Cracks and Voids in Thick Aluminum Plates, CIRP Journal of Manufacturing Science and Technology, Vol. 31, 2020, pp. 467-477.
- [16] Yabuuchi, K., Tsuda, N., Kimura, A., and et al., Effects of Tool Rotation Speed on the Mechanical Properties and Microstructure of Friction Stir Welded ODS Steel, Materials Science and Engineering: A., Vol. 595, 2014, pp. 291-296.
- [17] Das, H., Mondal, M., Hong, S. T., and et al., Microstructure and Mechanical Properties Evaluation of Friction Stir Welded Boron Steel, Journal of Mechanical Science and Technology, Vol. 34, 2020, pp. 2011-2017.
- [18] Shafique, J., Alrobei, H., and Wakeel, A., et al., Structural and Mechanical Properties of Friction Stir Welded Al2O3 and SiC Reinforced Al 7075 Alloys, Journal of Mechanical Science and Technology, Vol. 33, 2021, pp. 1437-1444.
- [19] Zohoor, M., Givi, M. B., and Salami, P., Effect of Processing Parameters on Fabrication of Al–Mg/Cu Composites via Friction Stir Processing, Materials and Design, Vol. 39, 2012, pp. 358-365.
- [20] Babu, S. D. D., Sevvel, P., and Kumar, R. S., Simulation of Heat Transfer and Analysis of Impact of Tool Pin Geometry and Tool Speed During Friction Stir Welding of AZ80A Mg Alloy Plates, Journal of Mechanical Science and Technology, Vol. 34, 2020, pp. 4239-4250.

DOI: ISSN: 2252-0406 https://admt.isfahan.iau.ir

Application of Adaptive Neuro Fuzzy Inference System (ANFIS) for Hardness Prediction of CK45 Based on Hot Rolling Parameters

Aydin Salimiasl *, Esmaeil Seidi, Mojtaba Moravej

Department of Mechanical Engineering, Payame Noor University, I.R. of Iran E-mail: aydin952@gmail.com, esmaeilseidy@yahoo.com, moravej60@gmail.com *Corresponding author

Received: 30 April 2025, Revised: 28 May 2025, Accepted: 15 August 2025

Abstract: Rolling stands as a crucial manufacturing technique that offers the dual benefit of enhancing steel's mechanical characteristics. Given the substantial time investment and financial burden associated with rolling experiment setups, implementing predictive models for mechanical properties can enhance precision while reducing both temporal and monetary costs. This study conducted hot rolling experiments on CK45 steel across two distinct environments. The specimens underwent rolling at five different temperature levels and five varying work-roll rotation speeds, maintaining consistent reduction percentages. Following the rolling process, the samples were rapidly cooled in ambient air and cold-water conditions, with hardness measurements obtained using specialized testing equipment. The research employed the Adaptive Neuro-Fuzzy Inference approach to forecast hardness values based on operational parameters. The model utilized rolling temperature and rotational speed of the rollers as input variables, while the hardness measurements post-quenching in both air and water environments served as output data. The analysis yielded R² values exceeding 0.99 between measured and predicted results for both environments, demonstrating ANFIS's effectiveness in accurately predicting sample hardness across various rolling speeds and temperatures.

Keywords: ANFIS, CK45, Hot Rolling, Mechanical Properties, Rolling Parameters

Biographical notes: Aydin Salimi received his PhD in Mechanical Engineering from the University of Gazi. Ankara. Turkey. He is currently an Assistant Professor at the Department of Mechanical Engineering, Payame Noor University, Tabriz, Iran. **Esmaeil Seidi** received his PhD in Mechanization Engineering from University of Tabriz. He is currently an assistant Professor at Payame Noor University, Tabriz, Iran. **Mojtaba Moravej** received his PhD in Mechanical Engineering from Shahid Chamran University of Ahvaz. He is currently an assistant Professor at Payame Noor University, Behbahan, Iran.

Research paper

COPYRIGHTS

© 2025 by the authors. Licensee Islamic Azad University Isfahan Branch. This article is an open access article distributed under the terms and conditions of the Creative Commons Attribution 4.0 International (CC BY 4.0) (https://creativecommons.org/licenses/by/4.0/)



1 INTRODUCTION

Rolling is one of the most common manufacturing processes for producing metallic products, such as steel, in different shapes and dimensions [1].

Flat rolling represents a cornerstone process in modern manufacturing, accounting for a substantial 40-60% of rolled product output in industrialized nations. This prevalent technique is executed through two primary methodologies: hot rolling and cold rolling, each selected based on factors such as product specifications, dimensional requirements, desired mechanical properties, and manufacturer objectives. The hot rolling process, characterized by deformation occurring above the material's recrystallization temperature, offers several notable advantages such as high deformation rates, Low required power for deformation, and no strain hardening in the work [2-3]. On the other hand, rolling process can be considered as a strengthening method of steel products in which the strengthening can be done by changing the grain sizes and plastic deformation. By using the rolling method as a manufacturing process, controlling the effective parameters of strengthening can be carried out at low costs and high rates [4-5]. Various studies have been conducted worldwide on the effect of rolling parameters on mechanical properties.

Nikan and colleagues [6] investigated the effect of hot rolling parameters on two-phase steels in their research. Based on their research results, the rolling temperature and reduction rate showed an effective change in mechanical properties. Mandana et al [7] evaluated the effect of hot rolling on the mechanical properties of low and high-carbon steels. They found out that the hot rolling process is an excellent method for eliminating the age hardening and increasing the yield strength in these kinds of steel.

Pitter et al [8] investigated the effect of hot rolling parameters such as reduction rate and rolling temperature on St60Mn in research. In this research, tensile strength, yield strength, hardening, modulus of elasticity, toughness and bending strength were measured based on the changes in rolling parameters.

As was mentioned earlier, the rolling process is a costly and time-consuming method, so creating an experimental setup for the evaluation of the effect of rolling parameters on mechanical properties is not feasible and cost-effective for all parameters. Therefore, creating a prediction model for predicting the mechanical properties of rolled products based on rolling parameters is necessary and can play a significant role in reducing costs.

During recent years, various artificial intelligence techniques, including fuzzy logic, neural networks, and adaptive neuro-fuzzy inference systems, have been employed to predict materials' mechanical properties.

In their study, Abdul Syukor Mohamad Jaya and colleagues [9] introduced a novel methodology for forecasting the hardness of Titanium aluminum nitride (TiAlN) coatings by implementing the Adaptive Neuro-Fuzzy Inference System (ANFIS). G. Khalaj et al [10] studied a new approach based on the adaptive network-based fuzzy inference systems (ANFIS) to predict the Vickers micro hardness of the phase constituents occurring in five steel samples after continuous cooling. Ly et al [11] used ANFIS model for better prediction of the compressive strength of MSC (manufactured sand concrete).

M. Zare et al [12] explored the potential of ANN and ANFIS models to forecast yield strength (YS) and ultimate tensile strength (UTS) of a warm compacted molybdenum prealloy using existing data. Analysis of ANFIS modeling versus ANN model results indicates superior performance during the training stage. Le et al [13] used an adaptive neuro-fuzzy inference system for the prediction of the critical buckling load of steel columns. Yadollahi et al [14] developed an adaptive network-based fuzzy inference system (ANFIS) model and two linear and nonlinear regression models to predict the compressive strength of geopolymer composites.

Xie, Q et al [15], in their research, utilized the machine learning method for predicting the mechanical properties of several steel alloys after the welding operations. The results indicated that the error percentage in predicting these properties ranges between 36.2% to 2.16%. Soleymani, M et al [16] used neural networks for predicting the mechanical properties of steel plates made of St37 during the welding operations. The preliminary results were previously announced. Xu, H et al [17] identified a specific chemical composition of a steel alloy after the welding operations.

In this research, the hot rolling operation was carried out in two different environments on CK45 steel. The samples were rolled at five levels of temperature and five levels of rotational speeds of work-rolls under the same reduction percentage. They were then quickly cooled down in room atmosphere and cold water, and the hardnesses were measured by a hardness testing machine.

The Adaptive Neuro-Fuzzy Inference method was used for predicting the hardness based on the input parameters. Rolling temperature and the rotational speed were considered as the inputs, and the measured hardness after quenching in two air and water environments were considered as the output of the model. The obtained R² for the measured and estimated results for each environment was above 0.99, which shows that the ANFIS method can effectively predict the hardness of the samples based on different rolling speeds and temperatures.

2 EXPERIMENTS

CK45 steel was used as the main material for hot deformation. The chemical composition of CK45 is given in "Table1".

Table 1 Chemical composition of CK45 steel

С	Mn	Si	P	S	Fe	Element
0.45	0.65	0.25	0.01	0.035	balance	%wt

A resistance furnace produced by Azar Furnace with the F11L model and with a nominal temperature of 1250 °C was used to heat the material. The sample dimensions are given in "Fig. 1".

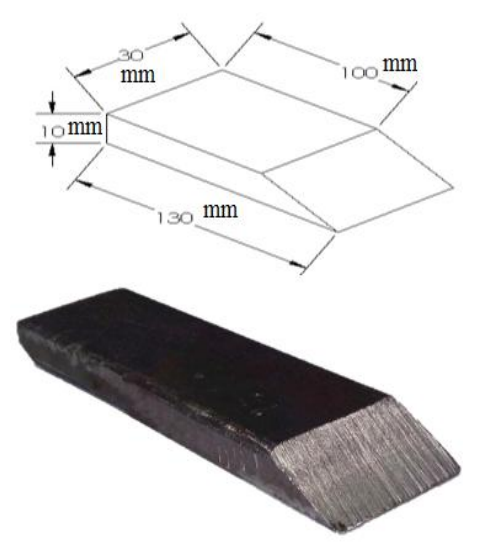


Fig. 1 The prepared sample for operation.



Fig. 2 The Vickers Hardness testing machine used for hardness measurement.

The rolling machine existing in the manufacturing workshop of Tabriz University of Sahand (IMK-1000h) was used for rolling operation. The power of this machine is 1000hp, and the roller diameter and roller length are 35cm and 40cm, respectively. An ESE WAY DVS B-P series of hardness testing machines ("Fig. 2") was used for measuring the material hardness.

The rotational speed of the rollers and the rolling temperature in five levels were used for the rolling operation. "Table 2" shows the rolling parameters used for the experimental procedure.

Table 2 Rolling parameters used for experiment

Rotational speed (rpm)	Temperature (°C)
10	850
12	900
15	950
17	1000
20	1050

3 EXPERIMENTAL PROCEDURES

After preparing the samples and increasing the furnace temperature to 950 °C, they were austinitized in furnace for two hours. They were then rolled immediately after being taken out of the furnace with 62 per cent of plastic deformation, at five rolling temperatures and five roller speeds. Figure 3 shows the rolling process. The samples were rapidly quenched in either ambient air (room temperature) or cold water (-100 °C), and they were then evaluated using a hardness testing machine using the Vickers method (30Kgf load and a pyramid diamond tool). The testing operations were repeated 5 times for each sample, and the averages were obtained and considered as the final hardness values for all of the samples. The value of the resultant force is obtained by the following equation:



Fig. 3 The samples under rolling.

4 ADAPTIVE NEURO FUZZY INFERENCE SYSTEM (ANFIS)

The Adaptive Neuro-Fuzzy Inference System (ANFIS), introduced by Jang in 1993, represents a significant advancement in modeling nonlinear systems [9], [18-19]. This Takagi-Sugeno type model integrates fuzzy-based human knowledge with data-driven learning, creating a robust input-output mapping framework. ANFIS operates within the structure of adaptive networks, employing a hybrid learning procedure. This innovative approach combines the strengths of artificial neural networks (ANN) and fuzzy inference systems (FIS), resulting in a model capable of both reasoning and self-learning. The fuzzy rules in ANFIS can be expressed as follows:

Rule 1: If x is A_1 and y is B_1 , then $f_1 = p_1x + q_1y + r_1$. Rule 2: If x is A_2 and y is B2, then $f_2 = p_2x + q_2y + r_2$.

In which p_1 , p_2 , q_1 , q_2 , r_1 , and r_2 represent linear coefficients in the consequent section, while A_1 , A_2 , B_1 , and B_2 denote nonlinear coefficients. Figure 4 shows the matching ANFIS structure for dual-input first-order Sugeno fuzzy systems with two rules.

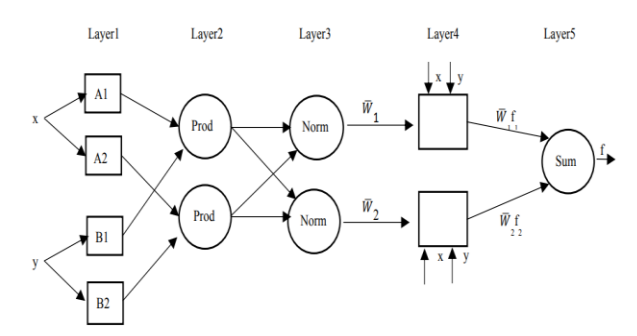


Fig. 4 Architecture of ANFIS model [13], [18].

The adaptive neuro-fuzzy inference system comprises a five-layer architecture: the fuzzy layer, product layer, normalized layer, de-fuzzy layer, and total output layer [13], [18], [20]. Each layer contains nodes with specific functions, as detailed below:

Layer 1: This initial layer, designated as the fuzzy layer, features adjustable nodes represented by square symbols and labeled A_1 , A_2 , B_1 , and B_2 . These nodes correspond to the system's inputs, x and y. The labels A_1 , A_2 , B_1 , and B_2 serve as linguistic descriptors utilized in fuzzy theory to delineate the membership functions (MFs). Within this layer, the node functions establish the membership relationship between the input and output functions, which can be expressed mathematically as:

$$O_j = \mu A_j(x); \quad j = 1, 2, ...$$
 (1)

$$O_i = \mu B_i(y); \quad i = 1, 2, ...$$
 (2)

In this system, $O_{1,i}$ and $O_{1,j}$ represent the output functions, while μ_{Ai} and μ_{Bj} denote the corresponding membership functions (MFs). These MFs may take various forms, including triangular, trapezoidal, or Gaussian functions, among others.

Layer 2: This layer, known as the product layer, consists of fixed nodes depicted as circles and labeled "Prod." This layer generates outputs w_1 and w_2 , which serve as weight functions for the following layer. The output of each node in this layer, denoted as $O_{2,i}$, is calculated by multiplying all incoming signals, as follows:

$$O_{2,i} = w_i = \mu A_i(x) \cdot \mu B_i(y); \quad i = 1, 2, \dots$$
 (3)

The output signal from each node, w_i , indicates the activation level of a rule.

Layer 3: This is the normalization layer where each node is a fixed node, denoted by a circle node and marked as Norm. The nodes compute normalized activation levels by calculating the ratio of this node's activation strength to the total sum of all activation strengths.

$$O_{3,i} = \overline{w}_i = \frac{w_i}{w_1 + w_2}; \quad i = 1, 2,$$
 (4)

Layer 4: This is the defuzzification layer containing adaptive nodes and indicated by square nodes. Each node i in this layer is an adaptive node with a node function:

$$O_{4i} = \overline{w}_i f_i = \overline{w}_i (p_i x + q_i y + z_i) \tag{5}$$

Where w_i represents the normalized firing strength output from layer 3 and pi, qi, and ri constitute the parameter set for this node. These parameters follow a linear pattern and are known as consequent parameters of this node.

Layer 5: This layer contains one fixed node, indicated by a circle and labeled sum, which calculates the final output by adding all incoming signals together as:

$$O_{5,i} = \sum_{i} \overline{w}_{i} f_{i} = \frac{\sum_{i} w_{i} f_{i}}{\sum_{i} w_{i}}$$
 (6)

The quantity of fuzzy sets corresponds to the number of nodes present in the initial layer. Meanwhile, the dimensionality of layer 4 reflects the total number of fuzzy rules integrated into the framework, demonstrating the sophistication and adaptability of the ANFIS structure. When compared to neural networks, fuzzy rules can be viewed as analogous to neurons.

An ANFIS system can undergo supervised training to progress from a given input toward a specific desired output. During the forward phase of the ANFIS hybrid algorithm, node outputs advance until layer four, and the consequent linear parameters (p_i, q_i, r_i) are calculated using the least-squares approach with training datasets. During the backward phase, error signals travel in reverse, and the premise nonlinear parameters (A_i, B_i, C_i) are modified through gradient descent. Research has demonstrated that this hybrid methodology is remarkably effective in ANFIS training [9], [13], [18-19].

5 RESULTS AND DISCUSSION

An ANFIS model was created for predicting the hardness of the rolled material based on the rotational speed of the rollers and the rolling temperature. The MATLAB program was used to develop the ANFIS model. To map the mentioned effective parameters to the material hardness and fuzzifying the inputs, Gaussian membership function was found to be the best fuzzifying function among the other membership functions.

When compared with other methods, Gaussian family methods had the most accurate results. The Gaussian-based membership function is defined by a central value m and a standard deviation k>0 as illustrated below ("Fig. 5"):

$$\mu(x) = e^{\frac{-(x-m)^2}{2k^2}}$$

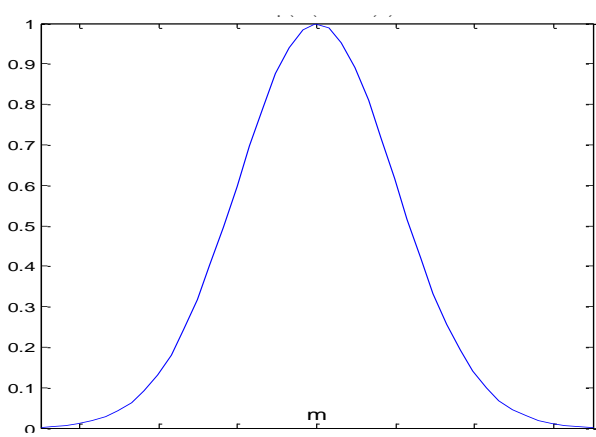


Fig. 5 Gaussian membership function.

After selecting the membership functions, the ANFIS model structure was created based on the experiments and defined fuzzy sets. In the designed structure, the rotational speed (V) and the rolling temperature (T) are defined as input, and the Vickers hardness (VH) as output of the model. The input and outputs of the model are given in "Fig. 6".

In the developed model, five fuzzy sets were implemented to fuzzify the rolling parameters, corresponding to their five distinct levels. Given that

the experimental design comprised 25 tests, a total of 25 fuzzy sets were established for both rotational speed and temperature as the primary variables. The rule count was matched to the number of experiments, resulting in 25 fuzzy rules being formulated for the hardness prediction model. Following the model construction, the ANFIS model training was executed using MATLAB software, and the outcomes were generated according to the model specifications. The ANFIS model architecture for predicting the material hardness after rolling is illustrated in "Fig. 7".

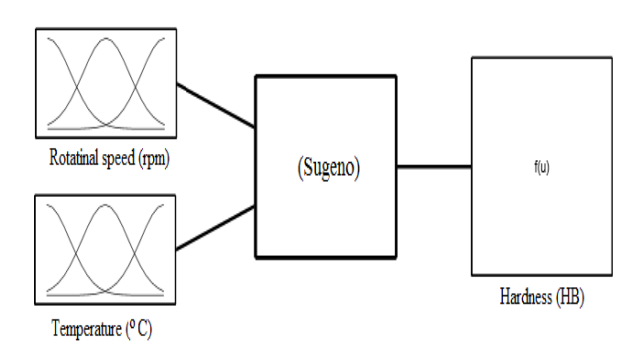


Fig. 6 Inputs and outputs of the ANFIS system.

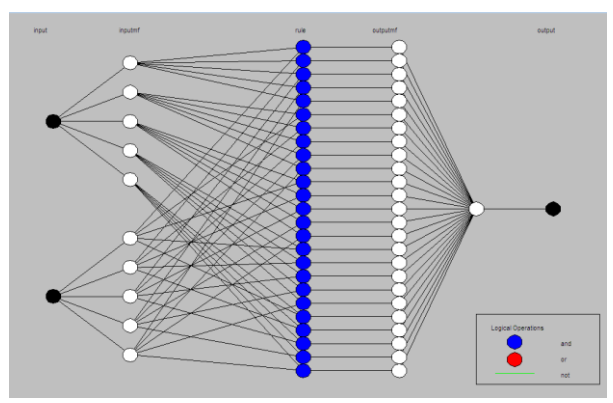


Fig. 7 The structure of ANFIS model.

As was mentioned earlier, after the rolling process, the samples were cooled separately in two environments, including air and water and the hardness values were measured using a Vickers test hardness machine. Two different ANFIS models were designed for each of the environments, and the predicted results of the models for these environments were estimated.

Graphical result of the ANFIS model was also created to evaluate the effects of the criterion variables. The effect of the rotational speed of the rollers and the rolling temperature on the hardness of the rolled samples is given in three-dimensional graphic in "Fig. 8". As is seen in the figure, both variables have a nonlinear effect on the material hardness. Figure 6 shows the result of the model for air quenching. As is seen in the figure, by increasing the rotational speed,

the hardness increases too. While by increasing the rolling temperature a dramatic decrease is happened in rolled material hardness values.

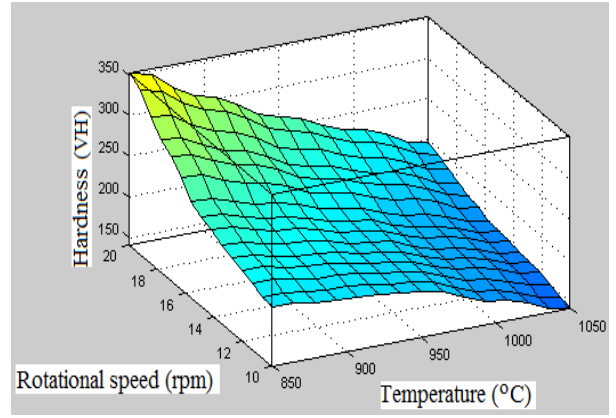


Fig. 8 The effect of rotational speed of rollers and rolling temperature on the hardness using of ANFIS model (air quenching).

Figure 9 shows the results of the model for water quenching. As is seen in the figure, by increasing both the rotational speed and the rolling temperature, the diagram shows an increase in rolled material hardness values. Moreover, by comparing the figures in air and water environments, it is found that the average hardness is higher in water quenching in relation to air quenching.

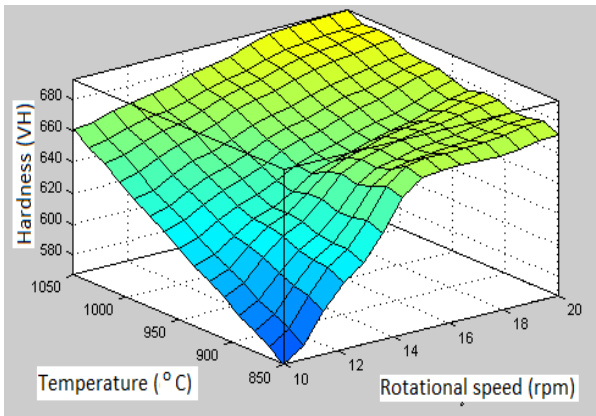


Fig. 9 The effect of rotational speed of rollers and rolling temperature on the hardness using the ANFIS model (water quenching).

The comparison diagram of the measured and estimated hardness is also conducted to obtain the R² values. Based on the comparison result, the R² value of the model is 0.9983 for air quenching and is 0.9947 for water quenching. It again confirms the ANFIS model accuracy and its contribution to the reliable estimation of rolled material hardness. Figures 10 & 11 show the comparison diagram of the measured and estimated hardness for air and water quenching, respectively.

In this research, the ANFIS method was used to predict the hardness, which, according to the authors of the paper, has not been previously reported in any research using this method. Given that the volume of experiments is usually low due to the high cost of rolling operations, compared to previous research done for similar cases using other methods, the aforementioned method has predicted the results with high accuracy by utilising the advantages of both fuzzy and neural models.

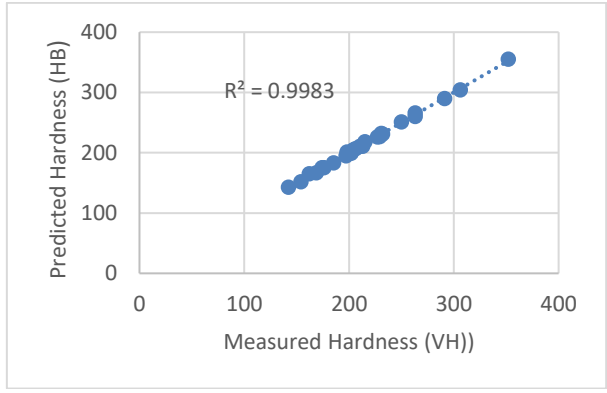


Fig. 10 Comparison of the measured and estimated results (air quenching).

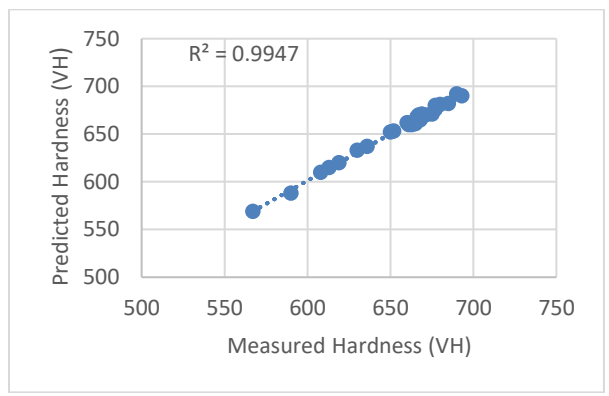


Fig. 11 Comparison of the measured and estimated results (water quenching).

6 CONCLUSIONS

This study investigated the impact of hot rolling process variables on the hardness properties of CK45 steel after air and water quenching treatments. The investigation focused on two key rolling parameters—temperature during rolling and the rollers' rotational velocity—as variables affecting material hardness. Multiple specimens underwent rolling processes at five distinct temperatures and five different roller speeds while maintaining consistent reduction ratios. Subsequently, the samples were rapidly cooled using ambient air and cold water, with hardness

measurements obtained through specialized testing equipment.

A predictive ANFIS framework was developed to forecast hardness values using operational parameters. The model incorporated temperature and rotational speed as input variables, while the measured hardness results from both air and water cooling served as output data. Analysis revealed that modifications to rolling parameters consistently produced noticeable alterations in the material's grain structure, consequently affecting mechanical characteristics, including specimen hardness.

The ANFIS model's predicted outcomes were validated against actual hardness measurements from testing equipment. The comparative analysis demonstrated that the ANFIS system accurately forecasts hardness values, establishing it as a reliable methodology for predicting results across various rolling parameter ranges not directly tested in the experimental phase.

REFERENCES

- [1] Ray, S., Introduction to Rolling Process, In Principles and Applications of Metal Rolling. Cambridge: Cambridge University Press, 2016, pp. 1-29.
- [2] Wang, S. F., Peng, Y. A., and Zhi-Jie, L., Work-Hardening and Deformation Mechanism of Cold Rolled Low Carbon Steel, Research Journal of Applied Sciences, Engineering and Technology, Vol. 5, No. 3, 2013, pp. 823-828.
- [3] Zhang, X., Wang, H., Scattergood, R. O., Narayan, J., and Koch, C. C., Modulated Oscillatory Hardening and Dynamic Recrystallization in Cryomilled Nanocrystalline Zn, Acta Materialia, Vol. 50, No. 16, 2002, pp. 3995-4004.
- [4] Ueji, R., Tsuji, N., Minamino, Y., and Koizumi, Y., Effect of Rolling Reduction on Ultrafine Grained Structure and Mechanical Properties of Low-Carbon Steel Thermomechanically Processed From Martensite Starting Structure, Science and Technology of Advanced Materials, Vol. 5, No. 1-2, 2004, pp. 153-162.
- [5] Sun, J. J., Lian, F. L., Liu, H. J., Jiang, T., Guo, S. W., Du, L. X., and Liu, Y. N., Microstructure of Warm Rolling and Pearlitic Transformation of Ultrafine-Grained GCr15 Steel, Materials Characterization, pp. Medium: X; Size: page(s), 2014, pp. 291-298.
- [6] Niakan, H., Najafizadeh, A., Effect of Niobium and Rolling Parameters on The Mechanical Properties and Microstructure of Dual Phase Steels, Materials Science and Engineering: A, Vol. 527, No. 21, 2010, pp. 5410-5414
- [7] Zebarjadi Sar, M., Barella, S., Gruttadauria, A., Mombelli, D., and Mapelli, C., Impact of Warm Rolling Process Parameters on Crystallographic Textures, Microstructure and Mechanical Properties of

- Low-Carbon Boron-Bearing Steels, Metals, Vol. 8, No. 11, 2018, pp. 927.
- [8] Nwachukwu, P. U., Oluwole, O. O., Effects of Rolling Process Parameters on The Mechanical Properties of Hot-Rolled St60Mn Steel, Case Studies in Construction Materials, Vol. 6, 2017, pp. 134-146.
- [9] Abdul Syukor Mohamad Jaya, A. S. H. B., Siti Zaiton Mohd Hashim, Habibollah Haron Muhd, R. M., and Md. Nizam Abd, R., Application of ANFIS in Predicting of TiAlN Coatings Hardness, Australian Journal of Basic and Applied Sciences, Vol. 5, No. 9, 2011, pp. 1647-1657.
- [10] Khalaj, G., Nazari, A., and Livary, A. K., Application of ANFIS for Modeling Of Microhardness of High Strength Low Alloy (HSLA) Steels in Continuous Cooling, Materials Research, Vol. 16, No. 4, 2013, pp. 721-730.
- [11] Ly, Pham, Dao, and Le, Improvement of ANFIS Model for Prediction of Compressive Strength of Manufactured Sand Concrete, Applied Sciences, Vol. 9, No. 18, 2019, pp. 3841.
- [12] Zare, M., Vahdati Khaki, J., Prediction of Mechanical Properties of A Warm Compacted Molybdenum Prealloy Using Artificial Neural Network and Adaptive Neuro-Fuzzy Models, Materials & Design, Vol. 38, 2012, pp. 26-31.
- [13] Le, L. M., Ly, H. B., Pham, B. T., Le, V. M., Pham, T. A., Nguyen, D. H., Tran, X. T., and Le, T. T., Hybrid Artificial Intelligence Approaches for Predicting Buckling Damage of Steel Columns Under Axial Compression, Materials, Vol. 12, No. 10, 2019, pp. 1670.
- [14] Yadollahi, M. M., Benli, A., and Demirboga, R., Application of Adaptive Neuro-Fuzzy Technique and Regression Models to Predict the Compressive Strength of Geopolymer Composites, Neural Computing and Applications, Vol. 28, No. 6, 2016, pp. 1453-1461.
- [15] Xie, Q., Suvarna, M., Li, J., Zhu, X., Cai, J., and Wang, X., Online Prediction of Mechanical Properties of Hot Rolled Steel Plate Using Machine Learning, Materials & Design, Vol. 197, 2021, pp. 109201.
- [16] Soleymani, M., Khoshnevisan, M., and Davoodi, B., Prediction of Micro-Hardness in Thread Rolling of St37 by Convolutional Neural Networks and Transfer Learning, The International Journal of Advanced Manufacturing Technology, Vol. 123, No. 9, 2022, pp. 3261-3274.
- [17] Xu, H., Xu, Z., and Zhang, K., Mechanical Properties Prediction for Hot Roll Steel Using Convolutional Neural Network, In Bio-inspired Computing: Theories and Applications, Singapore, L. Pan, J. Liang, and B. Qu, Eds., Springer Singapore, 2020, pp. 565-575.
- [18] Ginarsa, I. M., Nrartha, I. M. A., Muljono Agung, B., and Ardana, I. P., Application of Adaptive Neuro-Fuzzy Inference System Control in Power Systems, In Adaptive Neuro-Fuzzy Inference System as a Universal Estimator, V. Constantin Ed. Rijeka: IntechOpen, 2024, pp. Ch. 4.

- [19] Mohammadi, K., Shamshirband, S., Petković, D., Yee, P. L., and Mansor, Z., Using ANFIS for Selection of More Relevant Parameters to Predict Dew Point Temperature, Applied Thermal Engineering, Vol. 96, 2016, pp. 311-319.
- [20] Khalaj, G., Nazari, A., and Livary, A. K., Application of ANFIS for Modeling of Microhardness of High Strength Low Alloy (HSLA) Steels in Continuous Cooling, Materials Research-Ibero-American Journal of Materials, Vol. 16, 2013, pp. 721-730.